New methods for deblending spectral energy distributions in confused imaging

by

Todd Mackenzie

B.Sc., The University of Prince Edward Island, 2009
M.Sc., The University of British Columbia, 2011

A THESIS SUBMITTED IN PARTIAL FULFILLMENT OF
THE REQUIREMENTS FOR THE DEGREE OF

DOCTOR OF PHILOSOPHY

in

Faculty of Graduate and Postdoctoral Studies

(Astronomy)

THE UNIVERSITY OF BRITISH COLUMBIA

(Vancouver)

December 2015

Abstract

The submillimetre band is ideal for studying high-redshift star-forming galaxies, but such studies are hampered by the poor resolution of single-dish telescopes. Interferometric follow-up has shown that many sources are in fact comprised of multiple sources. For many such targets, confusion-limited *Herschel* observations that target the peak of their far-infrared emission are also available. Many methods for analysing these data have been developed, but most follow the traditional approach of extracting fluxes before model spectral energy distributions are fit, which erases degeneracies among fitting parameters and glosses over the intricacies of confusion noise. We have developed a forward-modelling method in order to tackle this problem in a more statistically rigorous way, which combines source deblending and spectral energy distribution fitting into the same procedure. We adapt our method to three independent projects, all of which benefit from our improved methodology.

We investigate a "giant submillimetre arc" behind a massive foreground cluster and uncover seven multiply imaged galaxies, of which six are found to be at a redshift of $z \sim 2.9$, and possibly constitute an interacting galaxy group. Using our new method, we disentangle the arc into its contributing components and constrain their far-IR properties.

Using confusion limited *Herschel*-SPIRE imaging, the far-IR properties LABOCA detected submillimetre sources can be constrained. Despite such sources often breaking up in high-resolution ALMA imaging, existing studies have implemented traditional fitting methods. We apply our new forward modelling method to re-derive constraints on the far-infrared properties of these sources, exploring selection effects on this sample, while highlighting the benefits of our fitting approach.

Finally, we present SCUBA-2 follow-up of 51 candidate proto-cluster fields undergoing enhanced star-formation. With the accompanying *Herschel*-SPIRE observations and a realistic dust temperature prior, we provide photometric redshift and far-IR luminosity estimates for 172 SCUBA-2 selected sources within the *Planck* overdensity fields. We find a redshift distribution similar to sources found in cosmological surveys, although our fields are enhanced in both density of sources and star formation rate density over a wide range of redshifts.

Preface

This work contains re-formatted pre-published work. The pronoun "we" is used throughout, as is convention in the literature, however all text has been written by myself. A breakdown of the work done by myself and others is given below.

- Chapter 2 was published as a paper in Monthly Notices of the Royal Astronomical Society (MacKenzie et al., 2014) and has been co-authored with Douglas Scott, Andy Gibb and others, with myself as the primary author. All work and writing was done myself with the exception of the lens model being provided by Jean-Paul Kneib and Johan Richard. *HST* and *Herschel* observations were publicly available, but the SCUBA-2 observations were performed by myself. Important feedback was provided by all co-authors.

- Chapter 3 strives to improve upon the work of Swinbank et al. (2014), thus all the images and catalogues were publicly available. All work and writting beyond these were done by myself, but important feedback was provided by both Douglas Scott and Mark Swinbank.

- Chapter 4 is a collaborative effort to follow up high-z candidates. The *Planck* source list and *Herschel* observations were provided by collaborators, but the SCUBA-2 observations, analysis and the writing were performed by myself. Collaborators who have provided feedback include Douglas Scott, Herve Dole, David Guery, Nicole Nesvadba, and Dave Clements.

Table of Contents

List of Tables

List of Figures

Acknowledgements

First, I would like to thank my supervisor, Dr. Douglas Scott. He has both guided me through my research and all the hurdles one must go through to complete both a Masters and Phd. Along with his guidance, he has also given me much independence and allowed me a much appreciated flexible schedule.

Second, I would like to thank my colleagues, Andy Gibb, Gaelan Marsden and Edward Chapin, who helped me through many technical problems, helped perform the research we have undertaken, and with whom I have collaborated with writing my published papers (MacKenzie et al., 2011, 2014). Without them, much of this work would not have been completed.

I must thank the sources of the funding I have received: my supervisor and NSERC for my salary and conference support, the department of physics and astronomy for tuition support and top-up bursaries, NSERC through an Alexander Graham Bell Canada Graduate Scholarship during my first year, UBC for a graduate fellowship during my second year, and the Joint Astronomy Centre in Hawaii for my journey to finally meet “my telescope”.

Finally, I must thank my parents for the support and freedom they have given me through all my studies.

Below are acknowledgements to the telescope facilities and organisations which this research has relied upon.

The James Clerk Maxwell Telescope is operated by The Joint Astronomy Centre on behalf of the Science and Technology Facilities Council of the United Kingdom, the Netherlands Organisation for Scientific Research, and the National Research Council of Canada. Data for this thesis were taken as part of the S2SRO programme, with Project ID M09BI142.

This research used the facilities of the Canadian Astronomy Data Centre operated by the National Research Council of Canada with the support of the Canadian Space Agency.

This research was supported by the Canadian Natural Sciences and Engineering Research Council and enabled through funding from the Canada Foundation for Innovation and through the CANFAR Programme, funded by CANARIE, Canada’s advanced Internet organisation.

This work is based in part on observations made with the *Spitzer Space Telescope*, which is operated by the Jet Propulsion Laboratory, California Institute of Technology, under a contract with NASA.

This research has made use of the NASA/IPAC Extragalactic Database (NED) which is operated by the Jet Propulsion Laboratory, California Institute of Technology, under contract with NASA.

The Digitized Sky Surveys were produced at the Space Telescope Science Institute under U.S. Government grant NAG W-2166. The images of these surveys are based on photographic data obtained using the Oschin Schmidt Telescope on Palomar Mountain and the UK Schmidt Telescope.

The VLA is part of the US National Radio Astronomy Observatory, a facility of the National Science Foundation operated under cooperative agreement by Associated Universities, Inc.

SPIRE has been developed by a consortium of institutes led by Cardiff University (UK) and including Univ. Lethbridge (Canada); NAOC (China); CEA, LAM (France); IFSI, Univ.

Padua (Italy); IAC (Spain); Stockholm Observatory (Sweden); Imperial College London, RAL, UCL-MSSL, UKATC, Univ. Sussex (UK); and Caltech, JPL, NHSC, Univ. Colorado (USA). This development has been supported by national funding agencies: CSA (Canada); NAOC (China); CEA, CNES, CNRS (France); ASI (Italy); MCINN (Spain); SNSB (Sweden); STFC, UKSA (UK); and NASA (USA).

PACS has been developed by a consortium of institutes led by MPE (Germany) and including UVIE (Austria); KU Leuven, CSL, IMEC (Belgium); CEA, LAM (France); MPIA (Germany); INAF-IFSI/OAA/OAP/OAT,
LENS, SISSA (Italy); IAC (Spain). This development has been supported by the funding agencies BMVIT (Austria), ESA-PRODEX (Belgium), CEA/ CNES (France), DLR (Germany), ASI/INAF (Italy), and CICYT/MCYT (Spain).

This research has made use of data from the HerMES project (`http://hermes.sussex.ac.uk/`), a Herschel Key Programme utilising Guaranteed Time from the SPIRE instrument team, ESAC scientists and a mission scientist.

The HerMES data were accessed through the HeDaM database (`http://hedam.oamp.fr`) operated by CeSAM and hosted by the Laboratoire
d'Astrophysique de Marseille.

Based on observations made with the NASA/ESA Hubble Space Telescope, obtained from the data archive at the Space Telescope Institute. STScI is operated by the association of Universities for Research in Astronomy, Inc. under the NASA contract NAS 5-26555.

This work is based [in part] on observations made with the Spitzer Space Telescope, which is operated by the Jet Propulsion Laboratory, California Institute of Technology under a contract with NASA. Support for this work was provided by NASA.

The Dark Cosmology Centre is funded by the Danish National Research Council.

Chapter 1

Introduction

Understanding the star-formation history of the Universe is an appealing subject that has gathered a lot of attention (see Fig. 1.1, e.g. Madau et al., 1996; Sanders et al., 2003; Takeuchi et al., 2003; Wyder et al., 2005; Schiminovich et al., 2005; Dahlen et al., 2007; Reddy and Steidel, 2009; Robotham and Driver, 2011; Magnelli et al., 2011; Bouwens et al., 2012; Cucciati et al., 2012; Magnelli et al., 2013; Gruppioni et al., 2013; Schenker et al., 2013; Madau and Dickinson, 2014). At the time of the Big Bang, we started with precisely zero stars, but as the Universe expanded and cooled, over-dense regions began to collapse due to gravity, and at some point the Universe formed its very first star. From that point in time, the co-moving (where a given volume encloses the same region of space, but expands with redshift due to the expansion of the universe) Star Formation Rate (SFR) density of the Universe increased until it peaked when the Universe was roughly 2 to 5 billion years old. The co-moving SFR density has since been on the decline. The evolution of SFR density is important in astronomy and cosmology, because it is directly related to structure and galaxy formation/growth. Specifically, it should be reproducible by cosmological models and/or simulations, although it does require accurate modelling of complex physical processes important for baryons within dark matter halos, such as the effects of stellar feedback, active galactic nuclei (AGN), supernovae and galaxy mergers.

The first accurate measurements of the co-moving SFR density of the Universe were performed by measuring the amount of ultra-violet (UV) radiation emitted by galaxies (Lilly et al., 1996). These wavelengths of radiation are primarily emitted from galaxies by hot young massive stars. The lifetime of such stars is relatively short lived, thus if large amounts UV radiation are seen being emitted from a galaxy, one can infer that the galaxy is forming many stars. Massive stars make up a minority of stars being formed, and thus one must extrapolate to lower masses to find a total SFR, using what is known of the initial mass function of stars (e.g. Salpeter, 1955). Once a galaxy stops rapidly forming stars, the hot massive stars present will quickly go supernova, and the galaxy will stop emitting large amounts of UV radiation in a few tens of millions of years.

The challenge of observing UV radiation is that it is absorbed by intervening dust (e.g. Whitford, 1958). This process is named “reddening” or “extinction” and can be modelled using multi-wavelength data (e.g. Fitzpatrick, 1999). However, in the early Universe, it is possible that the star-formation within a galaxy is almost completely enshrouded in dust, and will be missed entirely in optical studies. This makes it particularly difficult to accurately measure the co-moving SFR density at redshifts greater than about 1 (Sanders and Mirabel, 1996; Hughes et al., 1998; Steidel et al., 1999).

Another method to measure SFR is to observe in the far-infrared (far-IR). Ignoring the possibility of AGN, the energy emitted by a galaxy can be crudely divided into two categories: electro-magnetic (EM) radiation emitted by stars between wavelengths around 0.1 and 8 μm; and EM radiation emitted by dust between around 8 and 1000 μm. Dust is ubiquitous in the interstellar medium (ISM) and readily absorbs the shorter EM radiation of stars, re-emitting it at longer wavelengths. Young, hot, massive stars of a galaxy undergoing rapid star-formation will heat the dust within the galaxy and be re-emitted at far-infrared (far-IR) wavelengths, and

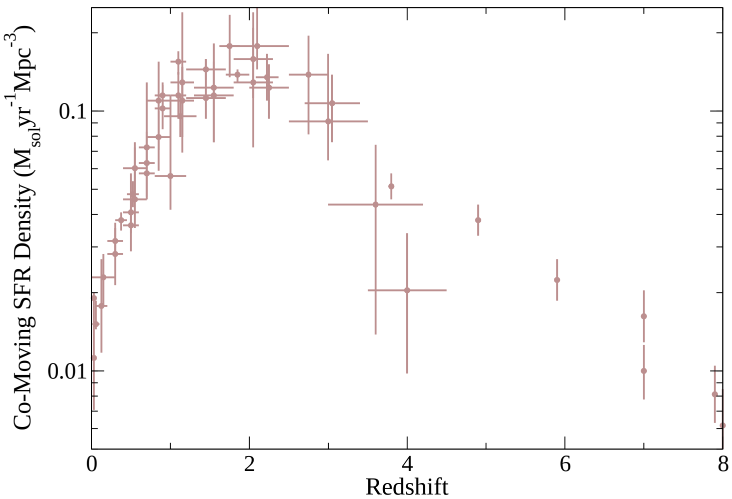

Figure 1.1: Co-moving SFR density history of the Universe as compiled by Madau and Dickinson (2014). A peak in SFR density is seen at $z \sim 2$, although measurements at higher redshifts are highly uncertain and subject to poorly understood systematic effects.

thus the luminosity between wavelengths of 8 and 1000 μm will be roughly proportional to the SFR of a galaxy (see review by Kennicutt, 1998). Because dust in the ISM is optically thin at these wavelengths, measurements of the SFR of a galaxy with this method is not affected by extinction.

In the earliest studies with targeted follow-up of known sources in the near-IR, it was found that the far-IR luminosity of some galaxies could match or exceed the energy output in the optical (Low and Kleinmann, 1968; Kleinmann and Low, 1970a,b). The first blind all-sky survey in the far-IR was performed by the Infrared Astronomical Satellite (*IRAS*, Soifer et al., 1984, 1987) and uncovered hundreds of previously unknown galaxies in the nearby Universe. This satellite was able to observe at wavelengths as long as 100 μm, which were previously not possible, since from the ground, Earth's atmospheres absorbs the majority of photons at these wavelengths. It was found that for many of these galaxies, labeled as "starburts" or "ultra-luminous infrared galaxies" (ULIRGs), the energy emitted in the far-IR far exceeded that of the shorter wavelengths and were missed in optical surveys.

Because the far-IR emission from a galaxy is dominated by the thermal emission of dust in the ISM, one can approximately model the far-IR spectral energy distribution (SED) of a galaxy by a modified blackbody of the form

$$S(\nu, T_\mathrm{d}, D) \propto \frac{\nu^{(3+\beta)}}{D^2} \left[\exp\left(\frac{h\nu}{k_\mathrm{B} T_\mathrm{d}} \right) - 1 \right]^{-1}, \tag{1.1}$$

where S is the flux density, ν is the observed frequency, β is the dust emissivity index, T_d is the dust temperature, and D is the distance to the source. Fig. 1.2 shows examples of modified blackbody spectra, although also including the effects of redshift, as described below. This SED shape adds just one extra term to the simple Planck distribution that describes thermal emission of a blackbody, namely dust emissivity, β. This dust emissivity is in fact a dust emissivity index (where emissivity $\propto [\nu/\nu_0]^\beta$), although it is referred to colloquially in literature as the dust emissivity. This parameter, β, is phenomenological, rather than physically-motivated, and is used to parameterise the effects resulting from the size distribution of dust grains, the optical depth of the dust at different frequencies, and actual temperature variations within the emitting regions (Draine and Lee, 1984). Typical values for dust emissivity range from 1.5 to 2. Like the dust emissivity, the dust temperature should not really be regarded as a physical parameter. Actual dust temperatures vary across galaxies depending on proximity to the galaxy centre and star-forming regions, and the temperature of individual grains can vary dramatically with time, thus the dust temperature here should be thought of as a phenomenological parameter with the units of Kelvin. Dust temperatures of around 35 K are typical for the star-forming galaxies that we will consider in this work (e.g. Chapin et al., 2009; Symeonidis et al., 2013; Swinbank et al., 2014; MacKenzie et al., 2014).

For distant galaxies, one must also consider the redshift of a source. This is the effect caused by space expanding and stretching the wavelength of photons, $\lambda_{\rm obs} = (1+z)\lambda_{\rm em}$, thus, reducing their energy. The consequence of redshift is such that at a redshift of z, each dimension of space becomes $1/(1+z)$ times as big as it is today (we are at a redshift of 0). When considering redshift, the modified blackbody becomes

$$S(\nu, T_{\rm d}, D_{\rm L}, z) \propto \frac{[\nu(1+z)]^{(3+\beta)}}{D_{\rm L}^2}\left[\exp\left(\frac{h\nu(1+z)}{k_{\rm B}T_{\rm d}}\right) - 1\right]^{-1}, \tag{1.2}$$

where z is the redshift, and $D_{\rm L}$ is now the "luminosity distance" (Peebles and Harrison, 1994), defined as

$$D_{\rm L} = (1+z)\frac{c}{H_0}\int_0^z \frac{dz'}{\sqrt{\Omega_{\rm m}(1+z')^3 + \Omega_{\rm K}(1+z')^2 + \Omega_\Lambda}}. \tag{1.3}$$

Here c is the speed of light, H_0 is the Hubble constant, and $\Omega_{\rm m}$, $\Omega_{\rm K}$, and Ω_Λ are cosmological parameters denoting the relative densities in matter, curvature, and the cosmological constant, respectively.

For a dust temperature of 35 K and a dust emissivity of 1.5, our modified blackbody SED peaks in flux density at 92 μm. Beyond this wavelength, the SED falls off and enters what is known as the "Rayleigh-Jeans" side of the SED. In this region, modified blackbodies become nearly pure power laws. Observing at wavelengths on the Rayleigh-Jeans side is difficult because of atmospheric absorption in the submillimtre regime. However, the next atmospheric window in this regime to make a significant impact in astronomy is at 850 μm, particularly with the Submillimeter Common User Bolometer Array (SCUBA, Holland et al., 1999) on the James Clerk Maxwell Telescope in Hawaii. At this wavelength, the flux density of a source is nearly invariant from a redshift of around 1 to 8. This is because as we go to higher redshifts, we are observing an intrinsically brighter part of the object's SED, thus countering the effect of the object becoming dimmer due to distance and redshift, and is shown in Fig. 1.2. The first deep blind survey with this instrument was of the Hubble Deep Field (HDF) by Barger et al. (1999). They found a total of five sources, with four of them at redshifts above 2. Their findings showed for the first time that the SFR density at $z > 2$ are perhaps a factor of 5 higher than previously thought from optical-based measurements. Many similar blind surveys have since followed, with greater depths and wider fields of view (e.g. Barger et al., 1999; Eales et al., 1999; Scott et al., 2002; Cowie et al., 2002; Borys et al., 2003; Coppin et al., 2006). There are now several telescopes/instruments operating (or operated) at or near this wavelength, including the Large Apex BOlometer CAmera (LABOCA, Siringo et al., 2009)

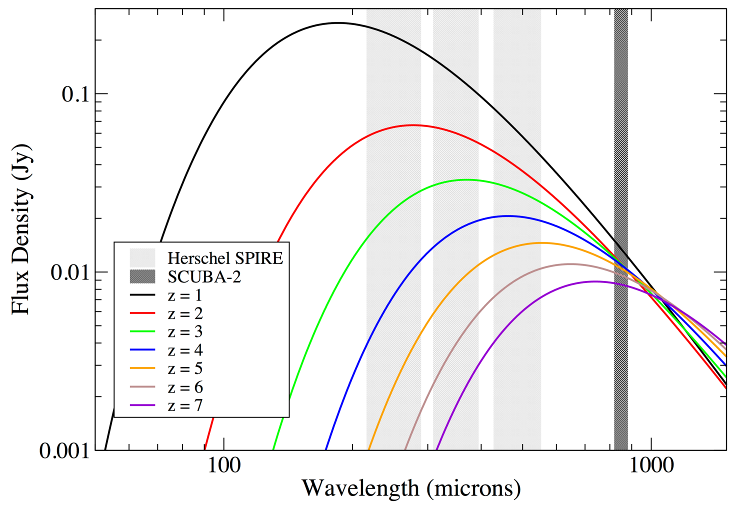

Figure 1.2: The SED of a modified blackbody with a dust temperature of 35 K, dust emissivity of 1.5, and a far-IR luminosity of 10^{13} $L_\odot$, plotted for different redshifts. The transmission bands of both *Herschel* SPIRE and SCUBA-2 at 850 μm are represented by the shaded areas. Observing at 850 μm has the advantage that a source's flux density is nearly invariant with redshift.

on the Atacama Pathfinder Experiment (APEX), AzTEC which was on the JCMT then the Atacama Submillimeter Telescope Experiment (ASTE, Ezawa et al., 2004), the Max-Planck Bolometer array (Kreysa et al., 1998) on the Institut de Radioastronomie Millimtrique (IRAM) telescope, and Bolocam (Glenn et al., 1998) on the Caltech Submillimeter Observatory (CSO). At shorter wavelengths, SCUBA also the exploited 450 μm atmospheric window, while the second-generation Submillimeter High Angular Resolution Camera (SHARC-2, Dowell et al., 2003) observed the sky at 350 μm (Kovács et al., 2006). The Balloon-borne Large Aperture Submillimeter Telescope (BLAST, Pascale et al., 2008) additionally observed at 250, 350 and 500 μm (e.g. Patanchon et al., 2009).

The latest single-dish instruments/observatories, and some of the primary instruments used in this work, include SCUBA-2 (Holland et al., 2013) on the JCMT, observing at 450 and 850 μm, and the *Herschel Space Observatory* (Pilbratt et al., 2010a). *Herschel* housed two photometric instruments. One was was Spectral and Photometric Imaging Receiver (SPIRE Griffin et al., 2010), observing at 250, 350 and 500 μm, and was essentially identical to the camera used in BLAST. The other was the Photodetector Array Camera and Spectrometer (PACS, Poglitsch et al., 2010), observing at 70, 100 and 160 μm.

One of the biggest challenges of observing in the submillimetre (submm) band is the resolution of these single-dish instruments, which typically have a full width at half maximum (FWHM) of 15 arcseconds or more. Within such large beams there are typically dozens of distant galaxies, making source identification difficult. If a field is observed for long enough, every pixel in the image will contain more signal than noise, but be comprised of many sources all blended together. In this scenario, only the brightest sources stand out and the uncertainty in measuring the flux density of any individual source is dominated by the high density

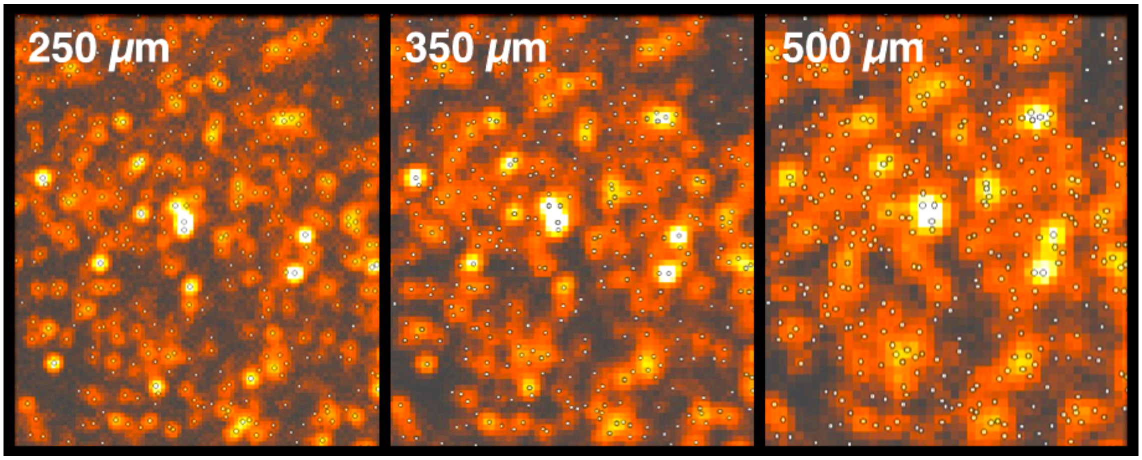

Figure 1.3: An example of confusion limited *Herschel* SPIRE confusion imaging at 250 μm, 350 μm and 500 μm. The location of known infrared and radio sources are denoted by white dots. In order to fit an SED to any of the known sources, one must devise a method that addresses the confused nature of the data.

of fainter sources blended together in the same region. This source of error is called "confusion noise"(e.g. Scheuer, 1957) and an example of such data are shown in Fig. 1.3. Even bright submm sources have often been found to be comprised of multiple fainter sources when followed-up with higher-resolution telescopes (e.g. Hodge et al., 2013), such as the Atacama Large Millimeter/submillimeter Array (ALMA). This problem of insufficient resolution is not unique to submm astronomy, and many methods have been developed to mitigate this problem. Using higher-resolution imaging at different wavelengths to identify contributing sources, flux densities for these sources can be "deblended" (e.g. Makovoz and Marleau, 2005; Roseboom et al., 2010; Elbaz et al., 2011a; Swinbank et al., 2014). However, this deblending of flux densities eliminates important degeneracies with neighbouring sources. Furthermore, each waveband is deblended independently, but confusion noise correlates both neighbouring pixels and neighbouring wavelengths, thus proper treatment of residuals while deblending is not trivial (see Patanchon et al., 2009; Vernstrom et al., 2014).

In practice, to try to determine the properties of a submm galaxy, one combines data at several different wavelengths. Once all this multi-wavelength photometry is compiled and a redshift estimate obtained (perhaps from spectroscopy), it is possible to move forward to fitting a model SED. The modified blackbody given above is a popular choice, due to its simplicity and accuracy in describing the generally coarse wavelength coverage of the data. In order to make a modified blackbody more luminous, one must either increase the dust temperature or add more mass to the dust. For many galaxies, in practice the answer appears to be a mixture of both possibilities and the result has been named the "L–$T_{\rm d}$" relation (e.g. Chapman et al., 2005; Magnelli et al., 2012; Casey, 2012; Symeonidis et al., 2013). The relationship has been found to evolve with redshift, but this claim has been disputed and could instead be attributed to selection effects (e.g. Chapin et al., 2009, 2011; Casey, 2012; Swinbank et al., 2014). In addition, the driving force behind the high SFR in such galaxies is debated. In some cases, it appears that galaxy-galaxy mergers trigger star-formation (Sanders and Mirabel, 1996), while other studies have suggested that the majority are simply the bright end of a galaxy "main-sequence" (Noeske et al., 2007; Daddi et al., 2007; Elbaz et al., 2011b). Again, when fitting a model SED, it is traditionally fitted to flux densities extracted from imaging. If these images are confusion limited, the process of deblending flux densities will eliminate important degeneracies with neighbouring sources, and potentially lead to biased results.

Here, we have developed new methods to fit SEDs using both high-resolution imaging and confusion limited imaging. Our method does not rely on the traditional two-step procedure of deblending/extracting flux densities then fitting your model, but instead combines these two tasks into one process. By doing so, we retain a statistical description of important degeneracies in fit parameters among neighbouring confused sources, and this allows us to perform a significantly improved analysis of available data. We originally developed this method to uncover and disentangle the submm emission from an interacting $z \simeq 2.9$ galaxy group that is multiply lensed by the massive MS 0451.6−0305 foreground cluster as described in Chapter 2. In Chapter 3, we adapt the same method to study the far-IR properties of submm galaxies followed-up with ALMA, often resolving sources into multiple contributing galaxies, and improving upon the work done by Swinbank et al. (2014). In Chapter 4 we use the same method as in Chapter 3 to analyse SCUBA-2 and *Herschel* SPIRE follow-up observations of *Planck* high-z candidates, comprised of strong gravitational lenses, potential proto-clusters and line-of-sight over-densities.

Chapter 2

Disentangling a lensed group of galaxies at z=2.9 observed with SCUBA-2

2.1 Introduction

Gravitational lensing has been a useful tool for enabling submm studies. The first results from the SCUBA submm camera on the James Clerk Maxwell Telescope (JCMT) (e.g. Smail et al., 1997) used "nature's telescope" to increase the detection rate of high-redshift submm sources and effectively beat the confusion limit for single dish studies. Now *Herschel* (Pilbratt et al., 2010b) has found that lensing is significant for some of the brightest submm sources, with surveys such as H-ATLAS and HerMES turning up a population of sources that are boosted enough that they can be studied in great detail in follow-up observations (e.g. Negrello et al., 2010a; Wardlow et al., 2013). However, the limited resolution of *Herschel*, and of non-interferometric ground-based observatories such as the JCMT, means that the effects of source blending are a cause of uncertainty in interpreting the results (e.g. Wang et al., 2011; Karim et al., 2013; Hodge et al., 2013), made more difficult in practice, since submm-bright sources are known to be typically merging or interacting systems, where disentangling the contribution to the combined spectral energy distribution (SED) is more complicated still. Even worse – while lensing is nominally achromatic, strong lensing of inhomogeneous extended sources within finite beams is *not* achromatic, since unresolved regions with different spectral properties can be lensed by different amounts. Thus the existence of strong lensing can be a double-edged sword, boosting the brightness of some sources, but making the detailed interpretation of their spectral energy distributions (SEDs) problematic (Serjeant, 2012). Multi-wavelength studies are key to understanding these complex systems.

MS 0451.6−0305, a massive galaxy cluster at a redshift of 0.55, is lensing several background sources and has been imaged at many different wavelengths: X-ray (Donahue et al., 2003b); optical (Gioia and Luppino, 1994; Takata et al., 2003; Kodama et al., 2005; Moran et al., 2007; Zitrin et al., 2011); near-IR (Borys et al., 2004; Wardlow et al., 2010); mid-IR (Geach et al., 2006); far-infrared (far-IR) (Oliver et al., 2012); mm/submm (Chapman et al., 2002a; Borys et al., 2004; Wardlow et al., 2010); and radio (Reese et al., 2000; Berciano Alba et al., 2010). In the optical, the previously discovered multiply-imaged sources include an extended optical arc composed of a Lyman-Break Galaxy (LBG) with a spectroscopic redshift of $z = 2.911$, as well as two extremely red objects (EROs) with a redshift of $z = 2.9 \pm 0.1$, determined from lensing models (Borys et al., 2004; Berciano Alba et al., 2010). The two EROs and the LBG are so close in separation ($\sim$10 kpc in projection) that they potentially constitute an interacting system. A fourth multiply imaged galaxy was discovered by Zitrin et al. (2011).

The steep number counts in the submm make lensing much more striking in this waveband than the optical – at 850 μm the SCUBA map of the cluster core showed a "giant submm arc,"

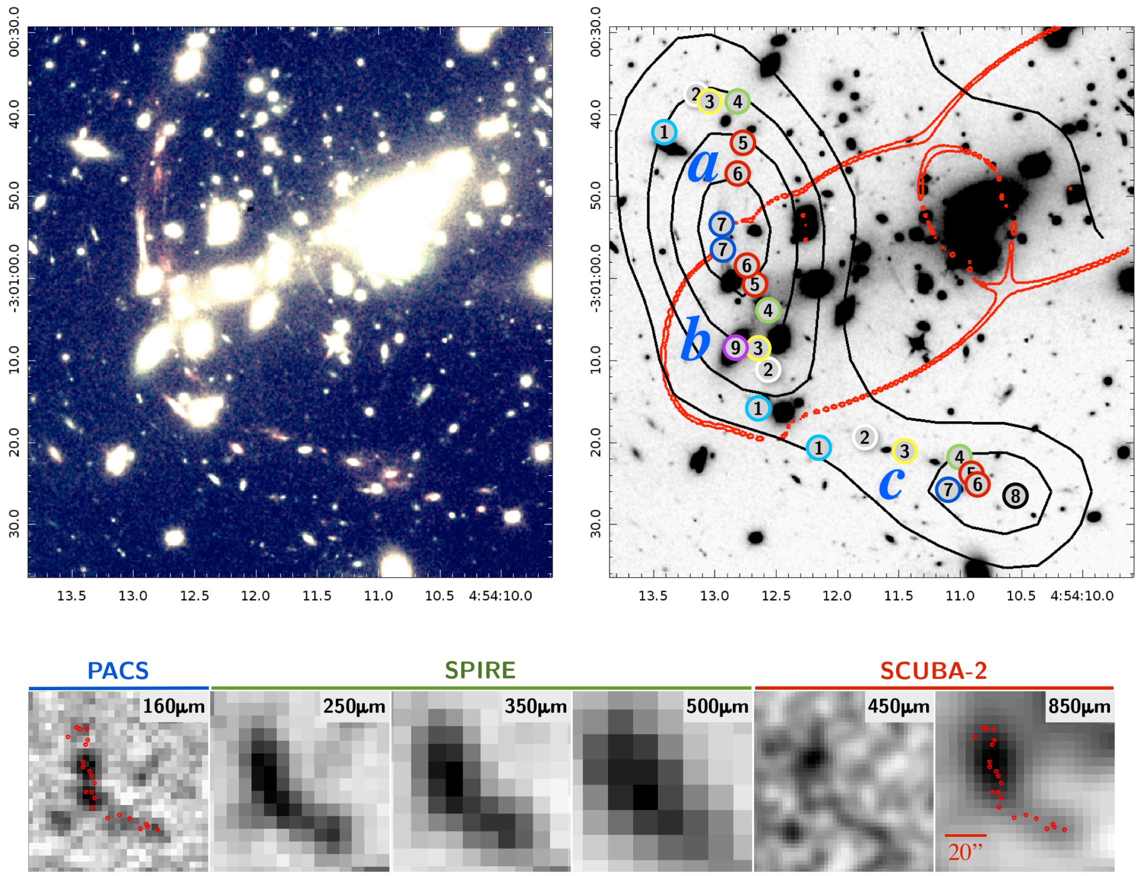

Figure 2.1: *Top left*: *HST* WFC3 colour-composite (red: 1.6 μm / H band, green: 1.6 + 1.1 μm / H + J bands, blue: 1.1 μm / J band), clearly showing the main optical arc (roughly vertical, at about RA = $4^{\rm h}54^{\rm m}12.9^{\rm s}$), offset slightly from the abundance of red images along the submm arc. The contrast has been stretched to highlight the faint arcs and multiply imaged galaxies. *Top right*: *HST* image (1.6 + 1.1 μm / H + J bands) with the positions of the multiply-imaged galaxies labelled numerically from 1 through 7, with sub-groups of images labelled as *a, b* and *c*. The galaxy discovered by Zitrin et al. (2011) is labelled as Galaxy 1 and the two EROs and the LBG discovered by Borys et al. (2004) are labelled Galaxy 5, 6, and 7, respectively. The red contour denotes the critical line of the lensing model for a redshift of z = 2.911, while the black contours represent the SCUBA-2 850 μm emission. Galaxy 8 is a singly imaged source with colours similar to those of the other multiply-imaged galaxies and has been found to be important when trying to reproduce the morphology of the submm arc. Galaxy 9 is a foreground galaxy at a redshift of z = 0.157. *Bottom*: The "giant submm arc" as seen by *Herschel* PACS and SPIRE and SCUBA-2 over more than a factor of five in wavelength range. The red circles plotted on the shortest and longest wavelength images mark the positions of the galaxies depicted in the top right panel. It is obvious that this string of multiply imaged $z \sim 2.9$ galaxy group sources are responsible for generating the majority of the submm arc. However, they are too spatially confused for traditional deblending techniques.

by far the brightest feature in this region of the sky, with an extent of around 1 arcminute, consistent with the blending of multiple galaxy images which lie near the critical line in the lensing model. If the optical galaxies are indeed interacting, the submm arc could be attributed to triggered star formation within one or more of these galaxies. This scenario is also supported by the radio data, as discussed in Berciano Alba et al. (2010).

New observations presented here using the Wide Field Camera 3 (WFC3) on *HST*, SCUBA-2 on the JCMT, and PACS and SPIRE on *Herschel*[1], shed new light on what is generating the submm arc. With the deeper *HST* images and a new Lenstool (Kneib et al., 1996; Jullo et al., 2007; Jullo and Kneib, 2009) lensing model, there are now *seven* known multiply-imaged galaxies (including the previously known four) in the region of the submm arc. Six of these multiply-imaged galaxies are consistent with a redshift of $z \sim 2.9$ and probably constitute an interacting galaxy group. To properly analyse the submm imaging of SCUBA-2 and *Herschel*, we have developed a new approach to disentangle the confused components generating the submm arc, which fully exploits the multiply-imaged and differentially-magnified nature of the system, and allows us to directly estimate both the dust temperature, T_{d}, and the far-infrared luminosity, L_{IR}, (and thus star formation rate, SFR) for each of the contributing galaxies. This allows us to investigate the T_{d} versus L_{IR} relation for intrinsically less luminous galaxies at high-z than traditional blank field surveys. Possible evolution of this relation with redshift allows us to probe the properties of star formation in the early Universe (e.g. Chapman et al., 2002b, 2005; Pope et al., 2006; Kovács et al., 2006; Chapin et al., 2011; Symeonidis et al., 2013; Swinbank et al., 2014; Sklias et al., 2014; Smail et al., 2014). Our method significantly improves upon the conventional method of extracting sources, or smoothing and binning multi-wavelength data to the worst resolution, before fitting SEDs (a process that destroys useful information).

This Chapter is organised as follows. In Section 2.2 we introduce the *HST* optical data and the lensing model. In Section 2.3.1 we present the SCUBA-2 data and in Chapter 2.3.2 the *Herschel* data. In Section 2.4.1 we present the SED model and image reconstruction methods and in Section 2.4.2 the model fitting procedure. Section 2.5.1 discusses the results and Section 5 finishes with the conclusions. Throughout we employ a ΛCDM cosmology with $\Omega_\Lambda = 0.7$, $\Omega_{\mathrm{m}} = 0.3$, and $H_0 = 70\,\mathrm{km\,s^{-1}\,Mpc^{-1}}$. ΛCDM cosmology is the current leading cosmological model used to describe the expansion history of the Universe, given the current rate of expansion and density of the components that fill the Universe (matter, photons and dark energy).

2.2 *HST* and the lensing model

Although the main motivation for our study comes from the new submm data, it makes the most scientific sense to first describe the optical data. We retrieved previously unpublished observations using WFC3 on *HST* from the Canadian Astronomical Data Centre (program 11591, PI: Jean-Paul Kneib). The observations were taken at 1.1 and 1.6 μm (J and H bands, respectively) with 2400 and 2600 second exposures, respectively. A small pointing shift in the data, with respect to *HST* data published by Borys et al. (2004) and Berciano Alba et al. (2010), was corrected by aligning to the older *HST* data in this field. These observations reveal a host of new red objects in the region of the submm arc (Fig. 2.1).

Lenstool (Kneib et al., 1996; Jullo et al., 2007; Jullo and Kneib, 2009) is a software package used to model gravitational lensing of sources behind massive galaxy clusters. The method involves modelling the gravitational effects of the most massive components of the intervening

[1] *Herschel* is an ESA space observatory with science instruments provided by European-led Principal Investigator consortia and with important participation from NASA.

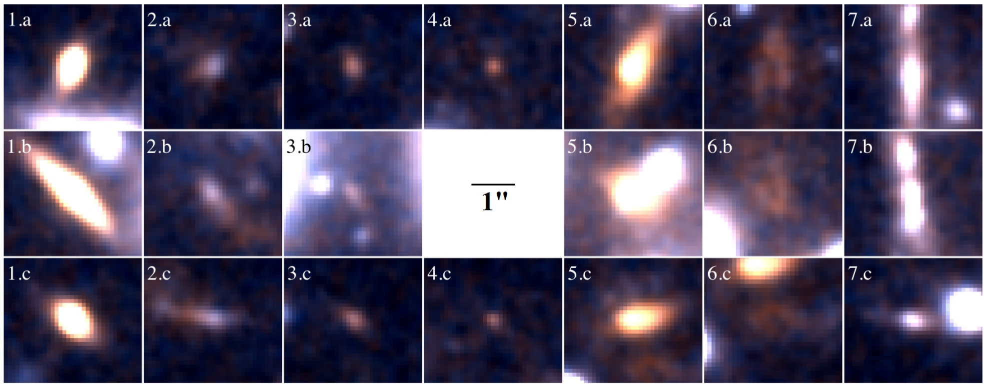

Figure 2.2: *HST* cut-outs at the locations of the seven multiply imaged galaxies listed in Table 2.1 with each column displaying the multiple images of a single galaxy. The letters refer to the three sub-groups of images labelled in Fig. 2.1. Image 4.b is not shown because it is obscured by foreground galaxies. We show a one arcsecond scale bar for all panels in the centre of the figure.

galaxy cluster (the encompassing cluster sized dark matter halo and the most massive galaxy sized halos) to predict the paths of photons of the background lensed sources into the image plane. The redshifts, positions, magnitudes and shapes of the multiply imaged lensed background sources are used to constrain the lensing model parameters. Using Lenstool and a new lensing model for the cluster, we were able to identify *three* new multiply-imaged galaxies within the *HST* images in the region of the submm arc. Table 2.1 lists the positions, amplifications factors, and redshift estimates derived from our model for of each of the seven multiply-imaged galaxies within the region of the submm arc. Fig. 2.1 shows the close positional arrangement of the multiple images with respect to the "giant submm arc" and the available submm data. Enlarged cut-outs of the multiply imaged galaxies are shown in Fig. 2.2. Borys et al. (2004) have already suggested that Galaxies 5, 6 and 7 are likely to be an interacting group at $z \sim 2.9$. Our new model supports their analysis and adds Galaxies 2, 3, and 4 to the same group, expanding it to a group of at least six galaxies at $z \sim 2.9$. Galaxy 1 is found to have a slightly higher redshift of $z = 3.11 \pm 0.03$ derived from the lensing model, and thus is not likely associated with the interacting group.

Galaxy 8 is not multiply imaged, but has similar colours to the rest of the multiply-imaged galaxies and has a disturbed morphology. If it is at the same redshift as the interacting group, our lensing model predicts no multiple images, consistent with the observations but yielding no additional constraints on its redshift from the lensing model. However, we have found that submm emission originating from near its position is important for reproducing the morphology of the submm arc (see Section 2.5.1), and thus we have included it in our model (see Section 2.4). Galaxy 9 is a foreground galaxy at $z = 0.157$ and has associated Multiband Imaging Photometer for Spitzer (MIPS) 24 μm (not described here) and PACS emission (see Section 2.3.2), thus it is also included in our model as a possible source of submm emission.

The lensing model consists of a cluster-sized dark matter halo, followed by 68 smaller mass halos to represent the most massive of the cluster galaxies. The parameters of the lensing model, such as the dark matter halo and galaxy masses, are constrained by the positions, relative magnitudes, ellipticities, and angles on the sky of the multiply imaged background sources. A total of 12 multiply imaged sources are known for this cluster, all of which are triply imaged, except for one source which is imaged five times with a confirmed spectroscopic redshift > 4. The model is fit using a Monte Carlo Markov chain (MCMC) method (Metropolis et al., 1953; Hastings, 1970), and is therefore able to provide uncertainties in the redshift and magnification estimates. The uncertainties provided do not include sources of error, such as an incomplete lensing model. More details concerning the LENSTOOL modelling will be presented in a forthcoming paper by Kneib & Richard (in prep.).

For our purposes, we are only interested in the redshift and magnification estimates provided by the lensing model. Along with the positions of the multiple images from the *HST* images, these will provide the backbone of the modelling described below. Because the uncertainties in redshift and magnification are small, we treat these values as fixed in order to reduce the complexity of the modelling described below. This does not significantly affect our results because our main source of uncertainty is the relatively low-resolution of the submm data and the confused nature of the *Herschel*-SPIRE imaging. However, we are vulnerable to the possible existence of fainter sources not detected in the *HST* imaging that may be contributing the the submm-arc, as was the case in Borys et al. (2004). Because we are able to reproduce the submm-arc as seen across all the available submm wavelengths with a high degree of fidelity (see Section 2.5.1), we do not believe we are missing any such missing component.

It is apparent that the nature of the submm arc is significantly more complicated than previously thought and is likely a combination of several of the galaxies described above.

2.3 New submm imaging

2.3.1 SCUBA-2

The cluster was observed with SCUBA-2 (Holland et al., 2013) on the JCMT during commissioning, as part of "Guaranteed Time" for the instrument team. A total of 12.7 hours in grade 2 weather between February of 2010 and February of 2012 achieved an rms error of 15 mJy per beam at 450 μm using 2 arcsecond pixels and 1.2 mJy per beam at 850 μm using 4 arcsecond pixels. Since the submm arc had already been observed at 850 μm using SCUBA (Borys et al., 2004), the motivations for the new observations were: (1) to confirm the bright lensed structure with SCUBA-2, without the complications introduced by SCUBA's requirement to chop (Borys et al., 2004); and (2) to detect the lensed structure at 450 μm, at a resolution better by about a factor of two, with the hope of resolving the submm arc into individual sources. The data were reduced using a configuration file optimized for blank fields using the SMURF data reduction software for SCUBA-2 (Chapin et al., 2013).

At 850 μm, the submm arc is detected at high signal-to-noise by SCUBA-2 (see Fig. 2.1). Its brightest part is elongated roughly north-south, and at the southern end curves to the west, just as in the original SCUBA image. The higher-resolution 450 μm data trace a largely similar structure, but at a lower relative sensitivity, with a signal-to-noise ratio of about 3 after smoothing with the beam, for the brightest portion of the lensed emission. The SCUBA-2 data are constrained by both resolution at 850 μm and sensitivity at 450 μm, and thus only limited conclusions can be obtained from these two channels alone. Fig. 2.1 shows the SCUBA-2 data alongside the *Herschel* SPIRE and PACS images for comparison, while Fig. 2.1 shows smoothed 850 μm contours plotted over the *HST* imaging.

2.3.2 *Herschel*

Confusion-limited images of MS 0451.6−0305 using *Herschel* SPIRE (Griffin et al., 2010; Swinyard et al., 2010) were taken as part of the guaranteed time program HerMES (the *Herschel*

Multi-tiered Extragalactic Survey, Oliver et al., 2012). The cluster was imaged at the three SPIRE wavelengths of 250, 350 and 500 μm with FWHM beam sizes of 18.1, 24.9 and 36.2 arcseconds, respectively (Griffin et al., 2010). A total of 18.3 hours of observation reached an rms of 1.5, 1.5 and 1.7 mJy per beam at 250, 350 and 500 μm, respectively, with pixel sizes of 6, 8.3, 12 arcseconds. A detailed description of the map-making procedure is given in Levenson et al. (2010), and the most recent updated method described in Viero et al. (2013). To ensure accurate astrometry, we have stacked on the positions of over 900 *Spitzer* MIPS 24 μm sources that overlap with the field and have corrected a 1.3 arcsecond shift in RA and 0.4 arcsecond shift in Dec. The uncertainty in this correction is 0.2 arcseconds, calculated by bootstrapping the 24 μm source list.

Two PACS (Poglitsch et al., 2010) observations taken as part of the PACS Evolutionary Probe key program (Lutz et al., 2011) are also available and were processed using the "multiple obsid scanMapDeepSurvey" pipeline within HIPE 10 (Ott, 2010). The default units were converted from Jy pixel^{-1} to Jy beam^{-1} by multiplying by the beam area and dividing by the pixel area. The beam area for the 160 μm point spread function (PSF) was found to be 180 arcsecond^2 and was computed by integrating over the beam profile provided by the NASA *Herschel* Science Center. A total of 5.2 hours of observation reached an rms of 2 mJy per beam using 3 arcsecond pixels. The FWHM at 160 μm is 11.6 arcseconds. For galaxies at $z \sim 3$, 70 μm PACS data are expected to be dominated by warm dust, which is not well reproduced by the simple SED model adopted in Section 2.4, and are therefore not used in this study.

The submm arc is detected across all the available submm bands (see Fig. 2.1), but with the large number of multiply-imaged galaxies (seen in Fig. 2.1) that are strung along the submm arc, it is unclear which galaxies are contributing. The morphology of the submm arc seen in each image is a function of both the telescope PSFs and the SEDs of the contributing galaxies. In addition to determining which galaxies are contributing, we would also like to constrain their physical properties. With the lensing model well constrained by the *HST* observations (see Section 2.2) and this wealth of multi-wavelength data, it is clear that a comprehensive modelling approach is required.

2.4 A framework for fitting SEDs to confused counterparts

Both Borys et al. (2004) and Berciano Alba et al. (2010) performed limited modelling of the optical and radio counterparts, respectively, in an attempt to reproduce the observed submm arc. Their approach of smoothing different plausible components with the SCUBA 850 μm beam showed that the LBG and two EROs are likely contributors, but neither could fully reproduce the observed submm arc. With new SCUBA-2 and *Herschel* observations, we are able to expand on this approach and have developed a framework for fitting SEDs to the confused optical counterparts, fully exploiting the strong gravitational lensing of this system.

While source plane reconstruction of multiply-imaged galaxies is an effective approach for high-resolution imaging (e.g. Kochanek and Narayan, 1992; Colley et al., 1996), it fails in the confused regime. Because the galaxies blend together in the submm, it is impractical to trace photons back through the lensing potential and into the source plane, since much of the photon positional information has been lost due to the large telescope beams. Instead, we use the high-resolution *HST* imaging to identify candidate counterparts to the submm galaxies in the optical, and use their positions as priors for the origin of any submm emission. We then forward-model the galaxy SEDs through the telescope filters, and use the amplification factors derived from the lensing model for each galaxy image, to reproduce the submm arc in each wavelength channel separately. Essentially, we are fitting SEDs of galaxies directly to the data, without the need for first deblending and extracting sources or smoothing and re-binning our data to the worst resolution (a process that destroys useful information).

Our method is complementary to that employed by Fu et al. (2012), where they forward-model a single submm source through the gravitational lens, allowing the position to vary, to reproduce the observed morphology of their Submillimetre Array (SMA) and Very Large Array (VLA) observations. With their model, they were able to show that the source of the gas and dust emission was offset from the optical counterpart. However, the gravitational lensing in this case is galaxy-galaxy lensing and the observations have much higher resolution than either the SCUBA-2 or *Herschel* observations presented here. The gravitational lensing presented here is for a group of galaxies being lensed by a foreground cluster and thus the set of multiple images subtends a much larger area on the sky than galaxy-galaxy lensing. The optical imaging provides positions which are more than adequate for our purposes, since, with the resolutions of SCUBA-2 and *Herschel*, any small offset of the submm emission from their optical counterparts will not have a strong effect on the morphology of the submm arc; the strongest effect of an offset would be seen in the relative amplifications of the multiple images. Our method is novel in that we reproduce the morphology of the submm emission across multiple wavelengths, while simultaneously fitting source SEDs, thus tying together the multi-wavelength data. These two complementary techniques (detailed source plane reconstruction and forward modelling SEDs at fixed source positions) could be combined in the future, given the proper observations.

2.4.1 Model SED and image reconstruction

The first ingredient we need is an SED model for our galaxies in the submm. For the longer wavelength channels of SCUBA-2 and *Herschel* SPIRE, the SED of a galaxy is well represented by a modified blackbody with a single temperature:

$$S(\nu, T_{\mathrm{d},i}, z_i, C_i) = C_i \left(\frac{\nu(1+z_i)}{\nu_0}\right)^{\beta} \Big(\nu(1+z_i)\Big)^3 \left[\exp\left(\frac{h\nu(1+z_i)}{k_{\mathrm{B}}T_{\mathrm{d},i}}\right) - 1\right]^{-1}, \tag{2.1}$$

where S is the flux density, ν is the observed frequency, $\nu_0 = 1.2\,\mathrm{THz} = c/(250\,\mu\mathrm{m})$, β is the dust emissivity, $T_{\mathrm{d},i}$ is the dust temperature, z_i is the redshift, C_i is a normalization factor, and the subscript i denotes the galaxy. We have virtually no constraining power on the dust emissivity, primarily due to the confused nature of the data, and we therefore fix it to a nominal value of 1.5. Due to the high redshifts of our galaxies, the shorter wavelength channels of *Herschel* are dominated by hot dust and are better represented by a power law on the Wien side, i.e.,

$$S(\nu, T_{\mathrm{d},i}, z_i, C_i) \propto \nu^{-\alpha}, \tag{2.2}$$

where the power law amplitude and the frequency at which to switch between the power law and modified blackbody are chosen so that the transition is smooth (i.e. the two functions and their first derivative are continuous); such a model has been used by Pascale et al. (2009), for example. For the same reason that we fix the value of the dust emissivity, we fix α to a nominal value of 2.0 as found by Casey (2012). We then propagate the individual galaxy SEDs through each telescope bandpass filter:

$$\bar{S}_b(T_{\mathrm{d},i}, z_i, C_i) = \frac{\int S(\nu, T_{\mathrm{d},i}, z_i, C_i) T_b(\nu) \mathrm{d}\nu}{\int T_b(\nu) f_b(\nu) \mathrm{d}\nu}, \tag{2.3}$$

where $\bar{S}_b$ is the galaxy flux density, as would be measured by the instrument for channel b, $T_b(\nu)$ is the transmission for channel b, and $f_b(\nu)$ is a calibration parameter. This calibration factor arises from the fact that bolometers respond to energy input and not flux density, and details can be found in Griffin et al. (2013). For *Herschel*, $f_b(\nu) = \nu_0/\nu$, due to assuming a power law SED shape for observed sources, where ν_0 is equal to $c/(160\,\mu\mathrm{m})$, $c/(250\,\mu\mathrm{m})$, $c/(350\,\mu\mathrm{m})$, and $c/(500\,\mu\mathrm{m})$ for 160, 250, 350 and 500 μm, respectively. We assume a constant calibration factor, $f_b(\nu) = 1$, for SCUBA-2, since the bandpass filters are relatively narrow and we are firmly on the Rayleigh-Jeans side of the spectrum.

Using the lensing model, the SCUBA-2 and *Herschel* images are reconstructed as follows:

$$M_b(\boldsymbol{x}) = \sum_i \sum_j A_{ij} \bar{S}_b(T_{\mathrm{d},i}, z_i, C_i) P_\nu(\boldsymbol{x} - \boldsymbol{r}_{ij}) + B_b. \tag{2.4}$$

Here $M_b(\boldsymbol{x})$ is the flux at position $\boldsymbol{x}$ for frequency channel b, A_{ij} is the amplification factor for image j of Galaxy i derived from the lensing model, $P_\nu(\boldsymbol{x} - \boldsymbol{r}_{ij})$ is the response function (i.e. the telescope beam), with $\boldsymbol{r}_{ij}$ denoting the position of image j of Galaxy i, and B_b is the image background. We assume all sources can be accurately represented by point sources at the positions of their optical counterparts. This assumption may be incorrect and tidal interactions may have created tails and bridges between the group members where the star formation is occurring, although the fidelity of our more simplistic model in Fig. 2.5 suggests that a more complex model is not needed here.

The response functions for the *Herschel* SPIRE channels are approximated as Gaussians with FWHM of 18.1, 24.9 and 36.2 arcseconds at 250, 350 and 500 μm, respectively, and 11.6 arcseconds at 160 μm for *Herschel* PACS. Due to the high-pass filtering of the SCUBA-2 data, we need to ensure that we have an accurate model of the effective response function, thus we simulate point-sources, for the 450 and 850 μm data, respectively, within the SMURF data-reduction software, and approximate the effective response function by fitting double Gaussians to their resulting shapes. The result for the 450 μm response function is a Gaussian with FWHM of 6.86 arcseconds and an amplitude of 0.893, plus a second Gaussian with FWHM of 34.6 arcseconds and amplitude of -0.015. The result for the 850 μm response function is a Gaussian with FWHM of 13.9 arcseconds and a amplitude of 0.869, plus a second Gaussian with FWHM of 25.9 arcseconds and amplitude of -0.077.

2.4.2 Model fitting

The SED model adopted is non-linear and due to the confused nature of this system, we expect there to be some degeneracies between fit parameters. To obtain uncertainties for each fit parameter, determine the degeneracies between them, and efficiently explore the large parameter space required, the model is fit to the data using an MCMC Metropolis-Hastings algorithm (Metropolis et al., 1953; Hastings, 1970) with Gibbs sampling (Geman and Geman, 1993, where only one model parameter is varied per MCMC chain point instead of all parameters,). This method has become widely used in Astronomy, especially for fitting cosmological parameters (Lewis and Bridle, 2002). The method requires a likelihood function to be defined to which the model is fit. Since the SCUBA-2 450 and 850 μm and PACS 160 μm data are limited by instrumental noise, the log likelihood functions for these data are calculated as follows:

$$-\log L_b = X_b + \sum_k \frac{(D_b(\boldsymbol{x}_k) - M_b(\boldsymbol{x}_k)/c_b)^2}{2\sigma_{b,k}^2}, \tag{2.5}$$

where subscript b denotes the band, $D_b(\boldsymbol{x}_k)$ are the data, $\boldsymbol{x}_k$ denotes the position of pixel k in the image, $\sigma^2_{b,k}$ is the instrumental noise for pixel k, c_b is the instrument calibration factor (with a mean value of unity), and X_b is a constant.

The log likelihood function for the *Herschel* SPIRE data is more complicated, since we are limited by extragalactic confusion noise as opposed to instrumental noise. The confusion limit in each channel is 5.8, 6.3 and 6.8 mJy at 250, 350 and 500 μm, respectively (Nguyen et al., 2010). In short, we cannot determine the flux density of a given source to greater accuracy than these confusion limits without using additional information from another sources (such as a prior position catalogue of all the sources within the field or flux density estimates from another telescope at a comparable wavelength). This means that the residuals after subtracting the model will be: (i) much larger than instrumental noise; (ii) correlated spatially with the beam; and (iii) correlated across wavelengths. This is because confusion noise is real signal generated from many faint sources that are all blending together to produce an unknown and correlated variable background. Taking confusion into account, the log likelihood function for the *Herschel* SPIRE data is therefore

$$-\log L_{\mathrm{SPIRE}} = X_{\mathrm{SPIRE}} + \frac{1}{2}\boldsymbol{R}^{\mathrm{T}}\boldsymbol{C}^{-1}\boldsymbol{R}, \tag{2.6}$$

where $\boldsymbol{R}$ is a one-dimensional list of the residuals, and contains all three channels of SPIRE data ($\boldsymbol{R} = \{D_{250}(\boldsymbol{x}_k) - M_{250}(\boldsymbol{x}_k)/c_{250}, D_{350}(\boldsymbol{x}_k) - M_{350}(\boldsymbol{x}_k)/c_{350}, D_{500}(\boldsymbol{x}_k) - M_{500}(\boldsymbol{x}_k)/c_{500}\}$), and $\boldsymbol{C}^{-1}$ is the inverse covariance matrix for the residuals. The covariance matrix, $\boldsymbol{C}$, is estimated using the GOODS-North HerMES field, also observed with *Herschel* SPIRE. This is the largest blank *Herschel* field with instrumental noise similar to that of the MS 0451.6−0305 data, and has an area of 0.1 deg^2. To estimate the covariance matrix, we extract cut-outs from the GOODS-North field, with the same dimensions as the MS 0451.6−0305 data, and calculate the covariance between all the pixels. We then average the covariance matrices of each set of cut-outs to obtain an estimate of the true covariance matrix, ignoring regions with standard deviations greater than twice the confusion limit in any channel to avoid regions with significantly bright sources. One could smooth the covariance matrix using the assumption that the sky is homogeneous and isotropic, but this may lead to singular matrices. Any standard method to invert the matrix may be used here. The total log likelihood is then

$$\log L_{\mathrm{total}} = \log L_{850} + \log L_{450} + \log L_{\mathrm{SPIRE}} + \log L_{160}. \tag{2.7}$$

This however assumes that the confusion noise on the sky is Gaussian and does not account for the possibility that the sky may hold non-Gaussian bright objects in our field of view, conspiring against our efforts to disentangle this galaxy group.

Flux calibration uncertainties, c_b, are taken into account during the fitting procedure by setting priors on c_b for each band. The flux calibrations of the 160, 450 and 850 μm data are 5%, 2.5% and 5%, respectively (Muller et al., 2011; Dempsey et al., 2013). SPIRE waveband calibrations are correlated, with a covariance matrix

$$C = \begin{vmatrix} 0.001825 & 0.0016 & 0.0016 \\ 0.0016 & 0.001825 & 0.0016 \\ 0.0016 & 0.0016 & 0.001825 \end{vmatrix}, \tag{2.8}$$

where the calibration is normalised to unity (Bendo et al., 2013, 4% correlated uncertainty between bands plus 1.5% uncorrelated between bands). The calibration uncertainties are a small effect when compared to the instrumental and confusion noise within the observations.

We set no prior (or a flat prior) on the amplitude of the modified blackbodies or each unknown image background. A hard prior, $T > 10\,\mathrm{K}$, is motivated by the fact that neither Dale et al. (2012) nor Amblard et al. (2010) found any colder *Herschel* galaxies in either the nearby or distant Universe, respectively. While we have corrected the relative pointing of *Herschel* and *HST*, we are unable to find any significant pointing shift in the JCMT due to the lower signal-to-noise in the map than what is available in the *Herschel* SPIRE observations. The nominal pointing accuracy is 1.5 arcseconds, and thus we include this as a prior and marginalise over any possible pointing offset along with the image backgrounds.

Table 2.1 lists the possible contributing galaxies in our model. This consists of the seven multiply-imaged galaxies, one singly-imaged red galaxy (Galaxy 8) with disturbed morphology, and one foreground galaxy (Galaxy 9) with associated MIPS 24 μm and PACS 160 μm emission. This brings the total to nine possible contributing galaxies. Their positions are derived from the *HST* data and their amplification factors are derived from the lensing model. The redshift of Galaxy 8 is set to a nominal value of $z = 2.9$ and we report the lensed far-IR luminosity and SFR for this galaxy. Galaxy image positions, amplification factors and redshifts are held fixed during the fitting procedure since their uncertainties are small.

By assuming the UV radiation of hot young stars is completely absorbed and re-radiated at longer wavelengths by intervening dust, as well as assuming an initial mass function and a starburst model, it is possible to estimate a rough conversion factor between bolometric luminosity and SFR (e.g. Lehnert and Heckman, 1996; Meurer et al., 1997; Kennicutt, 1998). Here, we convert far-IR luminosities, calculated by integrating the rest-frame SEDs from 8 to 1000 μm, to SFRs using the relation estimated by Murphy et al. (2011):

$$\mathrm{SFR} = 1.49 \times 10^{-10} \mathrm{M}_{\odot}\mathrm{yr}^{-1} L_{\mathrm{FIR}}/\mathrm{L}_{\odot}. \tag{2.9}$$

When reporting the uncertainties in our SFR values for each galaxy in our model, we consider only the uncertainty in far-IR luminosity and do not include any uncertainty in this relation.

2.5 Results and discussion

2.5.1 A compact group of galaxies at high redshift

All galaxies listed in Table 2.1 are included in our model and when fitted, we can clearly identify Galaxies 2, 6, 7, 8, and 9 as the sources of submm emission generating the submm arc. Fig. 2.3 shows the positional arrangement of the $z \sim 2.9$ galaxy group in the source plane with squares highlighting the galaxies responsible for generating the majority of the submm arc. Fig. 2.5 shows the data, the best-fit model, and the residuals after subtracting the model from the data. Also included in the figure is a decomposition of the submm arc into the unique contributions of each galaxy to the total best-fit model. Fig. 2.6 shows the MCMC likelihood contours for temperature and far-IR luminosity for these five galaxies, and Table 2.2 lists the results along with SFRs and upper limits for Galaxies 1, 3, 4, and 5. It is apparent in the MCMC likelihood contours that there is a strong degeneracy between the far-IR luminosities of Galaxies 6 and 7.

Fig. 2.6 shows a degeneracy between the luminosity of Galaxy 6 versus Galaxy 5 in our model, due to their close proximity. While our model prefers emission from Galaxy 6, Berciano Alba

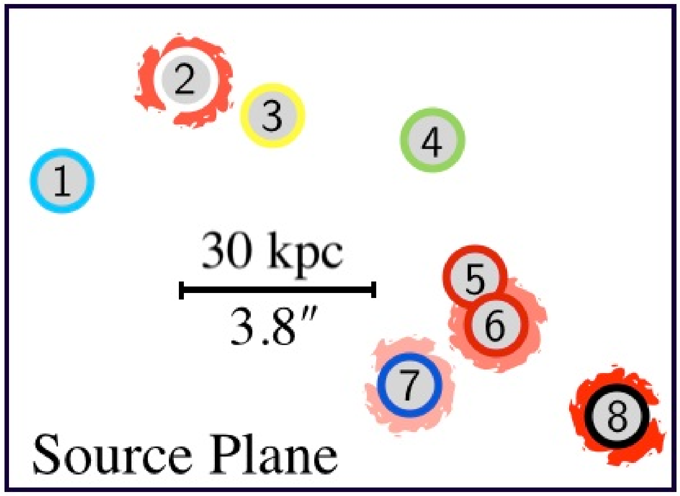

Figure 2.3: Source plane arrangement of the $z \sim 2.9$ group galaxies. Galaxies 2 through 7 are consistent with being at this redshift. Galaxy 1 lies at a slightly higher redshift, while Galaxy 8 is assumed to be part of the $z \sim 2.9$ group. The galaxies found to be generating the majority of the submm arc are highlighted with red backgrounds and scale with their measured far-IR luminosity. The galaxies are spread over no more than $\sim 100\,\mathrm{kpc}$ in projection, with many components separated by $\sim 10-20\,\mathrm{kpc}$.

et al. (2010) found that Galaxy 5 has associated radio emission, and hence we might consider that the submm emission attributed to Galaxy 6 in our model actually originates from Galaxy 5. We can test this hypothesis using the far-IR-to-radio correlation to predict a luminosity for Galaxy 5 and by also removing Galaxy 6 from our model and perform the fitting procedure again (thus forcing our model to attribute a portion of its luminosity to Galaxy 5), and then comparing the results. When doing so, we find that Galaxy 5 is attributed a luminosity of $(4.5 \pm 0.9) \times 10^{11}\,\mathrm{L}_{\odot}$ by our model (i.e essentially all the luminosity of Galaxies 5 and 6 together). Using the peak flux density measurements of Berciano Alba et al. (2010) at 1.4 GHz and the amplification factors in Table. 2.1, the unlensed 1.4 GHz flux density for Galaxy 5 is $(11 \pm 1)\,\mu$Jy. With these two measurements, we can calculate the logarithmic ratio of the far-IR flux to radio flux density, $q_{\mathrm{IR}} = \log_{10}[(S_{\mathrm{IR}}/3.75 \times 10^{12}\,\mathrm{Wm^{-2}})/(S_{1.4}/\mathrm{Wm^{-2}Hz^{-1}})]$. We assume a power law for the radio SED, $S_{\mathrm{radio}} \propto \nu^{\alpha}$, with $\alpha = -0.8$, and we correct for the effects of redshift. We find $q_{\mathrm{IR}} = 1.67 \pm 0.09$, which is 2-$\sigma$ below the relation found by Ivison et al. (2010b) for high-z galaxies, $q_{\mathrm{IR}} = 2.3 \pm 0.3$. This indicates that Galaxy 5 may have excess radio emission, suggesting contribution from an AGN, rather than radio emission associated with star formation. For this reason, we tend to follow the results which come from our model fitting, i.e. that Galaxy 6 dominates the far-IR emission. Nevertheless, it remain the case that interpretation of this pair is difficult with existing data.

Using ALMA to obtain high-resolution imaging, Hodge et al. (2013) recently showed that many of the submm galaxies (SMGs) previously detected in the LABOCA ECDFS Submillimeter Survey (LESS) are in fact composed of multiple fainter sources. The group of galaxies behind MS 0451.6−0305, consisting of Galaxies 2 through 8, is another good example of SMGs being composed of several sources. Unlensed, this $z \sim 2.9$ group would appear as a point source to any of the current single-dish submm telescopes, with flux densities of 3.8 ± 0.5 mJy, 8.5 ± 0.9 mJy, 10.4 ± 1.1 mJy, 8.0 ± 0.9 mJy, 8.9 ± 1.0 mJy, and 2.5 ± 0.3 mJy at 160, 250, 350, 500, 450 and 850 μm, respectively. This would put the group below the LESS survey detection threshold of 4.5 mJy at 870 μm, hence we are seeing evidence of submm source multiplicity due to physically associated groupings, as opposed to chance alignment, extending to fainter flux densities. On account of the frequency of submm source multiplicity, Hodge et al. (2013) suggest that many are likely to be physically associated. Our findings support this claim and suggest that these systems could be part of larger groups, many of which are too faint to be detected in the submm at current depths. The coincidence of being highly magnified by a massive foreground cluster allows us to study this group in much greater detail than would otherwise be possible, but we cannot infer how rare such SMG groups might be.

Although not as striking, a few analogues of our lensed star-forming galaxy group are found in the literature. First of all SMM J09431+4700, a SCUBA selected hyperluminous infrared galaxy behind A851 at $z = 3.35$ (Cowie et al., 2002; Ledlow et al., 2002). It is accompanied by an optically selected galaxy, DG 433, (Trager et al., 1997), separated by $400\,\mathrm{km\,s^{-1}}$ in redshift and 1 Mpc in projection. Secondly there is SMM J16359+6612, a faint SCUBA selected galaxy behind A2218 at $z = 2.5165$ (Kneib et al., 2004; Sheth et al., 2004). It is accompanied by two optically selected galaxies, separated by only $100\,\mathrm{km\,s^{-1}}$ in redshift and 130 kpc in projection. With more unlensed analogues of groups and recent mergers in the literature (e.g. Ivison et al., 1998; Frayer et al., 1998; Borne et al., 2000; Tacconi et al., 2008; Ivison et al., 2010a, 2013) and the ALMA multiplicity results from Hodge et al. (2013), it is clear that mergers and interactions play an important role for many SMGs. These distant galaxy groups are akin to nearby compact groups (Hickson, 1982), with the $z \sim 2.9$ galaxy group presented here reminiscent perhaps to Stephan's Quintet (Stephan, 1877), due to the remarkable number of galaxies associated with this submm source. There are surely more such systems to be discovered.

However, we believe that situations like we found here are fairly rare, and it is possible that what we have described in this chapter is the largest compact group that is lensed by a rich galaxy cluster on the entire sky. Although a detailed estimate of the probability is clouded by the usual problems with a posteriori statistics (i.e., if we only consider systems exactly like we found, then the probability would be arbitrarily small), we can carry out a crude estimate as follows. The MS0451 cluster has a mass of around $10^{15}\,\mathrm{M_\odot}$ (Donahue et al., 2003a) and an Einstein radius of around 30 arcseconds (where strong lensing is possible). Conservatively taking $3\times10^{14}\,\mathrm{M_\odot}$ as the limit for rich clusters, surveys (like the Planck catalogue of Sunyaev-Zeldovich sources, Planck Collaboration XXIX, 2013) suggest there are around 2000 such clusters on the sky, and hence the sum of the areas covered by their Einstein radii is about 10^{-5} of the sky. Assuming that a compact group has a mass of at least $3 \times 10^{13}\,\mathrm{M_\odot}$, then the Press-Schechter formalism (Press and Schechter, 1974) suggests a comoving density of about $10^{-6}\,\mathrm{Mpc^{-3}}$ at $z = 3$ for such groups. The Press-Schechter formalism is a model used to predict the abundance of massive halos in a given volume of the Universe, given a mass range. Taking a volume that covers $\Delta z = 1$ centred on $z = 3$, we estimate 500,000 such groups on the sky. Finally, multiplying this by the fraction of the sky that might be strongly lensed by rich clusters, we find that there will only be a handful of such objects lensed by a rich cluster. Given a group radius of 45 Kpc, the group crossing time is of the order 30 Myr. The merging timescale for a galaxy group is on the order of ten crossing times (Barnes, 1984; Navarro et al., 1987; Kodaira et al., 1990; Cavaliere et al., 1991; Hickson, 1997), thus the merging time of the galaxy group is on the order of 0.3 Gyr. This timescale is about a tenth the age of the Universe at a redshift of 2.9, and given that only a small percentage of $3 \times 10^{13}\,\mathrm{M_\odot}$ objects are compact groups (and even smaller for merging groups Hickson, 1997), it may seem surprising that this group has been found. However, the numerical argument presented here should be considered to be very approximate, and hence no strong conclusions can be drawn.

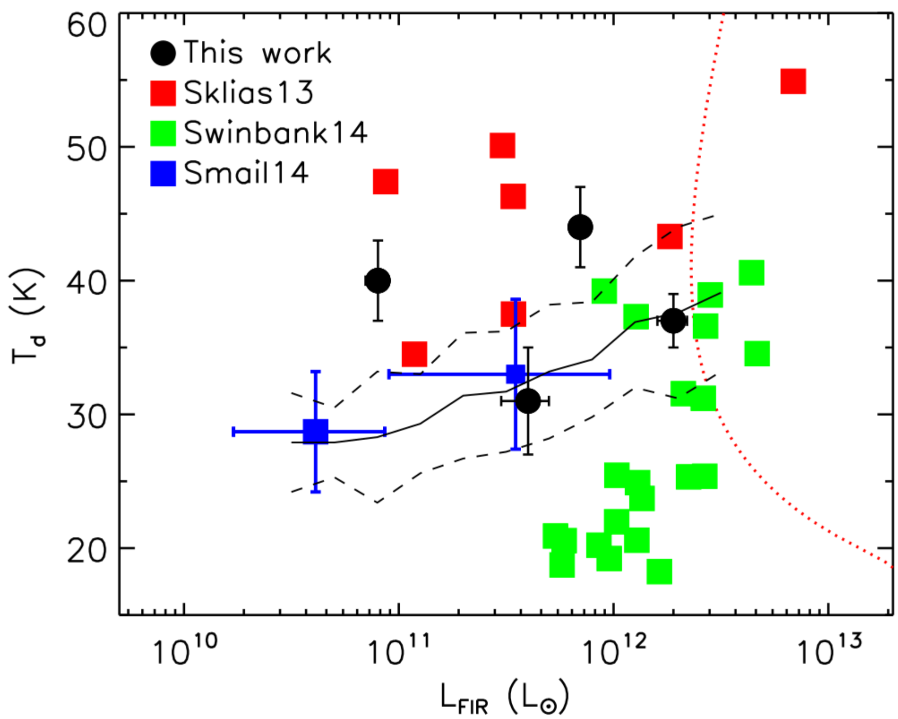

Figure 2.4: Dust temperature versus far-IR luminosity for several samples of galaxies. The solid line shows the trend found by Symeonidis et al. (2013) using *Herschel* for $z \sim$0–1.5 galaxies, with the dashed lines showing the dispersion of the sample. The green squares are the LESS SMGs followed up by Swinbank et al. (2014) with ALMA and *Herschel*, with $z \sim$1-6. The blue squares are the results of stacking on narrow-band [OII] emitters (left) and MIPS+radio sources not detected in SPIRE/SCUBA-2 (right) for a $z = 1.6$ cluster (Smail et al., 2014). The red squares are a sample of lensed SMGs discovered with *Herschel* (Sklias et al., 2014) with $z \sim$1.5–3. The black circles are the four $z \sim 2.9$ group galaxies that compose the submm arc of MS 0451.6−0305. Both Swinbank et al. (2014) and Symeonidis et al. (2013) found that high-z galaxies are on average cooler than the $z = 0$ relation, while Sklias et al. (2014) and our results report warmer than average results for high-z galaxies. The dotted red line represents the SPIRE 250 μm detection limit as a function of dust temperature for $z = 2.9$ galaxies, illustrating the usefulness of gravitational lensing, to push to fainter objects, when studying high-z SMGs.

2.5.2 Physical properties

The SED fits within our model allow us to investigate the physical conditions of each component of the submm arc. Fig. 2.4 plots $T_{\rm d}$ verus $L_{\rm IR}$ for the four $z \sim 2.9$ galaxies constrained by our model with trends and data found by Symeonidis et al. (2013), Swinbank et al. (2014), Sklias et al. (2014), and Smail et al. (2014). As described in Symeonidis et al. (2013), studying the relation between these two quantities gives insight into the nature of star-formation within galaxies: a flat relation with $T_{\rm d}$ = constant implies that star formation regions become more extended when increasing far-IR luminosity, while something close to the Stefan-Boltzmann law, $L_{\rm IR} \propto T^4$, would imply constant star formation region size (for optically thick star-forming clouds). Symeonidis et al. (2013) used *Herschel* SPIRE and PACS to probe this relation and found the trend plotted as a solid black line in Fig. 2.4, with dashed lines showing the dispersion. When comparing low and high redshift galaxies, they found that the later were up to 10 K cooler than their low redshift counterparts, suggesting evolution with redshift towards more extended

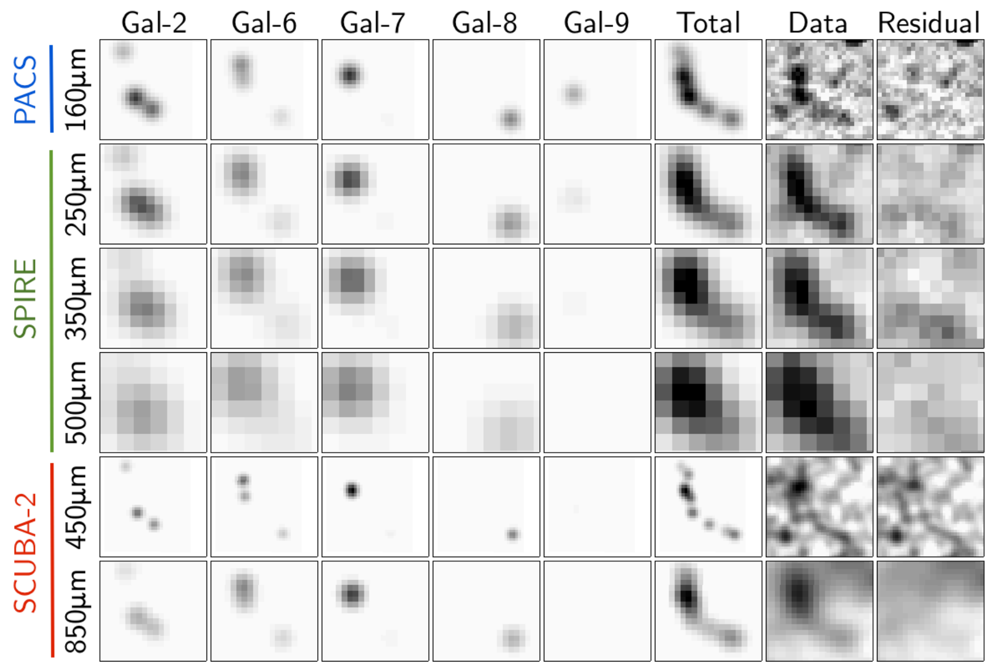

Figure 2.5: Decomposition of the submm arc into each contributing galaxy for the best-fit model, the total emission for the best-fit model, the data, and the residual after subtracting the model from the data. The columns display the contributions for individual galaxies across the six wavelength channels. Due to the differential amplification and unique positions of the multiple images, the emission from each galaxy is morphologically unique and this is what enables us to disentangle their contributions. The data and residual components for the SCUBA-2 channels have been smoothed with the FWHM for each respective wavelength. The pixel sizes are 3, 6, 8.3, 12, 2, and 4 arcseconds at 160, 250, 350, 500, 450, and 850 μm, respectively.

star-forming regions in the early universe. Swinbank et al. (2014) found a similar trend with high redshift galaxies being on average 2–3 K colder than low redshift galaxies. Smail et al. (2014) found that stacking on narrow-band [OII] emitters and MIPS+radio sources within a $z = 1.6$ cluster (intrinsically faint sources) found no evidence of evolution, although their direct detections with SPIRE and SCUBA-2 (thus intrinsically luminous sources) were also found to be cooler in temperature. A recent study by Sklias et al. (2014), used gravitational lensing to examine intrinsically fainter galaxies at high redshifts. Although limited by small number statistics, they found the opposite trend for high redshift galaxies. When adding the four $z \sim 2.9$ galaxies constrained by our model, our results appear to support those found by Sklias et al. (2014). This suggests that selection effects and/or biases are present in the different studies.

As has been pointed out before (e.g. Chapman et al., 2005; Chapin et al., 2011) selection effects can be extremely important when studying the correlation between $T_{\rm d}$ and $L_{\rm IR}$. The Swinbank et al. (2014) sample of SMGs were selected at 870 μm and thus may be biased towards lower dust temperatures, and those of Sklias et al. (2014) were formally selected at 160 μm, and thus could be biased towards warmer dust temperatures. It should be noted that the submm arc in MS 0451.6−0305 was first discovered at 850 μm (Chapman et al., 2002a) and therefore unlikely to be biased towards the warmer dust temperatures that we find.

In addition to the selection biases inherent in focusing on a single distinctive source, there are also a number of systematic uncertainties that could be present in our modelling approach.

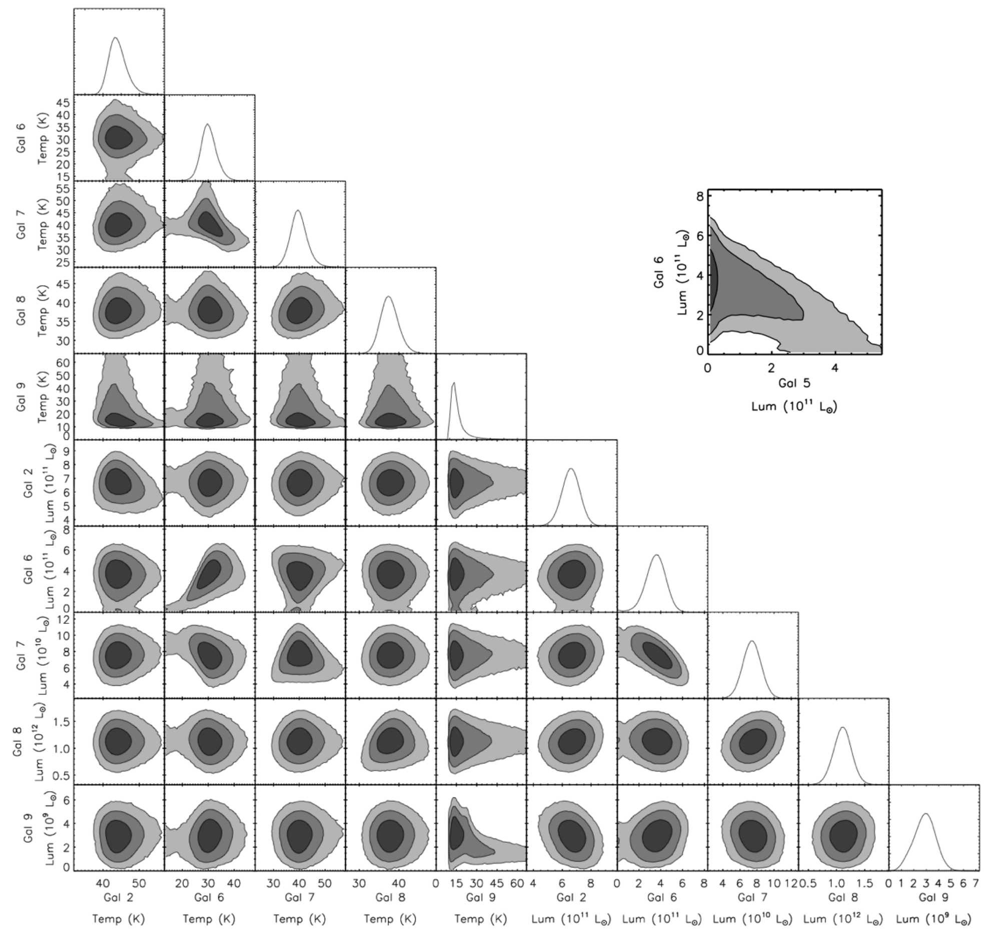

Figure 2.6: MCMC likelihood contours for temperature and far-IR luminosity for the galaxies that were found to contribute to the submm arc. The contour levels are 68%, 95% and 99.7% confidence intervals. Because of the morphological uniqueness of the lensing for each individual galaxy, there are few degeneracies here, despite the images of the system being spatially confused. The most obvious degeneracy is between the far-IR luminosity of Galaxy 6 and Galaxy 7. *Top right*: The likelihood contours for the model show a degeneracy between Galaxy 5 and Galaxy 6 in far-IR luminosity. Galaxy 5 has associated radio emission, but it exceeds that expected from SFR alone, thus suggesting an AGN component.

Most importantly, we have fixed the amplification factors for the galaxy images. Any errors in amplification can affect our results in several ways. For example, since the contributions to the submm arc from Galaxies 7 and 8 (See Fig. 2.5) are mostly point-like, then any uncertainty in amplification predominantly affects their measured far-IR luminosities and SFRs. This is especially true for Galaxy 7, because two of its images lie very close to the critical line (the region in the image plane with the greatest amplification), and thus its amplification is highly sensitive to any offset between optical and submm components of the galaxy. The uncertainty in relative amplification between galaxy images likely affects which galaxies are preferred by the data. For example, the images of Galaxies 5 and 6 are spatially very close, thus the different relative amplifications between their respective images probably contributes to Galaxy 6 being preferred by the model fits.

It is possible that the simple SED model we have adopted may not accurately approximate the true SEDs of the galaxies in the lensed system. The dust emissivity, β, is known to be partially degenerate with dust temperature and we have fixed it to a nominal value of 1.5, thus the uncertainties reported for dust temperatures are likely too small. Furthermore, although this newer *HST* data is both deeper and at a longer wavelength, it is possible that we are missing fainter group members, as was the case in previous studies (Borys et al., 2004; Berciano Alba et al., 2010). If any of the galaxies are not at $z \sim 2.9$, their reported far-IR luminosities and thus SFRs will be affected, since the distances to the galaxies are used in these calculations. This is especially true for Galaxy 8, as we have no constraints on its actual redshift and our analysis has assumed it to be part of the $z \sim 2.9$ group.

Despite these reservations, the model we have adopted appears to provide a reasonably good fit to the data across a wide range of wavelengths. Higher resolution submm data would be needed to further investigate the nature of the $z \sim 2.9$ galaxy group.

2.6 Conclusions

With our new modelling approach, we have overcome the confused nature of this complex system by fully exploiting the differential amplification across the galaxy group and the multiple imaging caused by the strong gravitational lensing. This has allowed us to tackle the challenge of disentangling and fitting SEDs to multiple components of the submm arc. We have shown that the submm arc is predominantly generated by four of the seven galaxies that probably comprise a group at a redshift of $z \sim 2.9$, with star-formation likely triggered by the galaxies undergoing a merger. It is therefore not necessary to have a hidden region of dust-enshrouded star formation (as postulated by Berciano Alba et al., 2010) to explain the morphology of the submm arc. This method also demonstrates the power of a broad multi-wavelength approach to fully understanding the nature of the submm arc: *HST* imaging gives us the priors on galaxy positions, as well as providing the constraints for the lensing model; *Herschel* samples the peak of the far-IR SED, as well as providing the high-resolution far-IR imaging at 160 μm; and SCUBA-2 850 μm data samples the long wavelength portion of the FIR SED at a resolution that closely matches that of the 160 μm imaging.

This is a unique system that gives us a glimpse into the formation of structure and stars in the early Universe, and no other submm lens discovered to date can match the number of separate galaxies lensed from the same redshift. Spectroscopy and high-resolution follow-up with new interferometer observatories will be the key to confirming and unravelling the nature of this high-z merging galaxy group.

Table 2.1: List of images for the eight high-z galaxies, as well as one low redshift interloper at $z = 0.157$. The galaxy IDs denote each galaxy, as shown in Fig. 2.1, and the letters indicate the multiple images of each galaxy (with a being the most Northern images in each case, and c being the most southern images). The position of image 4.b, as inferred from the lensing model, is obscured by foreground cluster galaxies. The amplification factors are derived from the LENSTOOL modelling in Section 2.2. The redshift of Galaxy 8 is unknown, but has similar colours to the other high-redshift multiply imaged galaxies, a disturbed morphology, and was found to be important for reproducing the SW extension of the submm arc, thus we assume a nominal redshift of 2.9. The superscript letters on the redshifts denote the method by which they were derived: a for redshifts derived from the lensing model, b for a spectroscopic redshift, and c for a nominally chosen value. The reported magnitudes for the F160W and F110W *HST* filters are AB magnitudes.

Gal ID	R.A. J2000	Dec. J2000	F160W (Mag)	F110W (Mag)	Amplification	Redshift	Notes
1.a	04:54:13.42	−3:00:43.0	21.94 ± 0.01	23.26 ± 0.01	3.80 ± 0.06	3.11 ± 0.03^a	(Takata et al., 2003; Zitrin et al., 2011)
1.b	04:54:12.65	−3:01:16.5	20.91 ± 0.01	22.27 ± 0.01	20 ± 1		(Takata et al., 2003; Zitrin et al., 2011)
1.c	04:54:12.17	−3:01:21.4	21.86 ± 0.01	23.18 ± 0.01	7.3 ± 0.1		(Takata et al., 2003; Zitrin et al., 2011)
2.a	04:54:13.15	−3:00:38.4	24.15 ± 0.03	24.74 ± 0.05	2.86 ± 0.04	2.91 ± 0.04^a	
2.b	04:54:12.58	−3:01:11.9	23.62 ± 0.03	24.25 ± 0.05	8.1 ± 0.4		
2.c	04:54:11.79	−3:01:20.2	22.88 ± 0.02	23.85 ± 0.04	6.1 ± 0.1		
3.a	04:54:13.04	−3:00:39.2	24.98 ± 0.04	26.28 ± 0.07	3.19 ± 0.05	2.94 ± 0.04^a	
3.b	04:54:12.68	−3:01:09.1	23.27 ± 0.02	24.09 ± 0.05	2.98 ± 0.05		
3.c	04:54:11.46	−3:01:21.7	24.27 ± 0.04	25.49 ± 0.06	4.31 ± 0.08		
4.a	04:54:12.82	−3:00:39.3	24.82 ± 0.05	26.39 ± 0.08	3.57 ± 0.06	2.94 ± 0.04^a	
4.b	*04:54:12.53*	*−3:01:04.5*	26.64 ± 0.07	27.50 ± 0.09	6.2 ± 0.2		Lensing model position
4.c	04:54:11.03	−3:01:22.4	24.70 ± 0.05	25.90 ± 0.07	3.36 ± 0.06		
5.a	04:54:12.81	−3:00:44.4	21.73 ± 0.01	23.51 ± 0.01	5.3 ± 0.1	2.89 ± 0.03^a	ERO-B(Borys et al., 2004)
5.b	04:54:12.69	−3:01:01.5	21.81 ± 0.01	23.47 ± 0.01	6.4 ± 0.1		ERO-B(Borys et al., 2004)
5.c	04:54:10.93	−3:01:24.6	21.97 ± 0.01	23.78 ± 0.02	2.89 ± 0.04		ERO-B(Borys et al., 2004)
6.a	04:54:12.81	−3:00:47.5	22.62 ± 0.02	24.55 ± 0.06	8.2 ± 0.2	2.86 ± 0.03^a	ERO-C(Borys et al., 2004)
6.b	04:54:12.72	−3:00:59.6	24.41 ± 0.04	26.60 ± 0.15	4.98 ± 0.08		ERO-C(Borys et al., 2004)
6.c	04:54:10.88	−3:01:25.8	22.85 ± 0.02	24.67 ± 0.09	2.76 ± 0.04		ERO-C(Borys et al., 2004)
7.a	04:54:12.95	−3:00:54.8	21.80 ± 0.01	22.26 ± 0.01	33 ± 2	2.911 ± 0.003^b	LBG(Borys et al., 2004)
7.b	04:54:12.93	−3:00:57.5	22.29 ± 0.01	22.76 ± 0.01	45 ± 3		LBG(Borys et al., 2004)
7.c	04:54:11.11	−3:01:26.6	23.66 ± 0.02	24.23 ± 0.03	2.87 ± 0.04		LBG(Borys et al., 2004)
8	04:54:10.55	−3:01:27.3	22.77 ± 0.02	23.50 ± 0.03	1.73 ± 0.04	2.9^c	Singly imaged
9	04:54:12.85	−3:01:09.1	18.91 ± 0.01	19.19 ± 0.02	–	0.15719^b	foreground galaxy

Table 2.2: Lensing-amplification-corrected results from the model. The total L_{FIR} for the $z \sim 2.9$ galaxy group is $(3.1 \pm 0.3) \times 10^{12}\mathrm{L}_{\odot}$, which gives a SFR of (450 ± 50) $\mathrm{M}_{\odot}\mathrm{yr}^{-1}$. The 95^{th} percentile upper limits are given for galaxies not found to be contributing to the submm arc. Note that Galaxy 9 is a foreground galaxy at $z = 0.157$ and is therefore not lensed.

Gal ID	T_{d} (K)	L_{FIR} ($\mathrm{L}_{\odot}$)	SFR ($\mathrm{M}_{\odot}\mathrm{yr}^{-1}$)	S_{160} (mJy)	S_{250} (mJy)	S_{350} (mJy)	S_{500} (mJy)	S_{450} (mJy)	S_{850} (mJy)
1	–	$< 8.2 \times 10^{9}$	< 1.3	–	–	–	–	–	–
2	44 ± 3	$(6.7 \pm 0.6) \times 10^{11}$	99 ± 9	0.94 ± 0.10	1.9 ± 0.2	1.9 ± 0.2	1.2 ± 0.2	1.4 ± 0.2	0.31 ± 0.06
3	–	$< 1.5 \times 10^{11}$	< 23	–	–	–	–	–	–
4	–	$< 3.3 \times 10^{11}$	< 50	–	–	–	–	–	–
5	–	$< 2.0 \times 10^{11}$	< 35	–	–	–	–	–	–
6	31 ± 4	$(3.6 \pm 0.9) \times 10^{11}$	53 ± 14	0.31 ± 0.12	0.7 ± 0.3	1.3 ± 0.4	1.5 ± 0.4	1.5 ± 0.4	0.7 ± 0.2
7	40 ± 3	$(7.5 \pm 1.0) \times 10^{10}$	11 ± 2	0.10 ± 0.02	0.22 ± 0.04	0.23 ± 0.06	0.16 ± 0.05	0.18 ± 0.04	0.04 ± 0.02
8	37 ± 2	$(1.9 \pm 0.3) \times 10^{12}$	290 ± 40	2.5 ± 0.4	5.6 ± 0.8	6.9 ± 1.0	5.1 ± 0.9	5.8 ± 1.0	1.5 ± 0.3
9	17 ± 9	$(1.7 \pm 0.5) \times 10^{9}$	0.25 ± 0.07	3.6 ± 1.0	2.5 ± 0.8	1.3 ± 0.5	0.5 ± 0.2	0.6 ± 0.2	0.08 ± 0.04

Chapter 3

Fitting spectral energy distributions to sources in blended imaging

3.1 Introduction

With the advent of single-dish submm observatories such as those using SCUBA-2 (Holland et al., 2013) on the JCMT, BLAST (Pascale et al., 2008), and *Herschel* (Pilbratt et al., 2010a), we now have a window into the distant star-forming Universe (e.g. Smail et al., 1997; Barger et al., 1999; Eales et al., 1999; Scott et al., 2002; Cowie et al., 2002; Borys et al., 2003; Coppin et al., 2006; Patanchon et al., 2009; Eales et al., 2010; Elbaz et al., 2011b; Oliver et al., 2012; Geach et al., 2013). However, due to the resolution of these observatories, instrumental noise is not the limiting factor when determining the uncertainty in flux density of individual sources, when observed for sufficiently long period of time. Instead, we are limited by confusion noise caused by the high density of sources relative to the resolution of imaging. Higher resolution imaging can help with extracting the desired information from these confused images, but the current methods of combining such data are lacking in statistical rigour.

A common exercise in these wavebands is to determine the spectral energy distribution (SED) of a source. When the source is much brighter than the confusion limit, this task is rather straight forward. However, if the source is near or below the confusion limit for any particular waveband, then determining the SED of a source becomes problematic. This has been done with varying degrees of success using "de-blending" techniques (e.g. Makovoz and Marleau, 2005; Roseboom et al., 2010; Elbaz et al., 2011a; Swinbank et al., 2014), often using positional priors from other higher-resolution observations, to first extract fluxes, then subsequently fit SED models. This two-step process usually ignores the intricacies of confusion noise (both spatial and between wavebands) and erases useful information regarding degeneracies among SED model fits with nearby sources, and thus the attribution of uncertainties to fit parameters becomes problematic. We present here a method of combining high-resolution imaging with confused imaging, which simultaneously fits SEDs and separates sources, thus deblending SEDs instead of flux densities. We adapt the forward-modelling method of MacKenzie et al. (2014) (henceforth referred to as M14; see also Chapter 2) and generalise it to the case of point source deblending of model SEDs. This new method forward-models each source SED to recreate the image plane and uses an MCMC Metropolis-Hastings algorithm (Metropolis et al., 1953; Hastings, 1970) with Gibbs sampling (Geman and Geman, 1993) to determine the uncertainties of the model parameters. We apply our method to the Atacama Large Millimeter/submillimeter Array (ALMA) Survey of Submillimeter Galaxies (ALESS, Hodge et al., 2013) in the Extended Chandra Deep Field South (ECDFS) to measure the far-IR properties of the LABOCA ECDFS Submm Survey selected sources (LESS, Weiß et al., 2009). This task has already been undertaken by Swinbank et al. (2014), allowing us to compare our results with those of a more traditional method. Along with 870 μm ALMA data, this region of the sky has also been imaged with the *Herschel* Spectral and Photometric Imaging Receiver (SPIRE, Griffin et al., 2010) and Photoconductor Array Camera and Spectrometer (PACS, Poglitsch et al., 2010), thus making it the ideal arena to test the effectiveness of our method. Throughout we employ a ΛCDM cosmology with $\Omega_\Lambda = 0.728$, $\Omega_\mathrm{m} = 0.272$, and $H_0 = 70.4\,\mathrm{km\,s^{-1}\,Mpc^{-1}}$ (Komatsu et al., 2011).

3.2 A framework for fitting SEDs to blended sources

3.2.1 Model SED and image reconstruction

We adopt a modified blackbody SED with a power-law component for the shorter wavelengths, as in M14. Because we are not dealing with multiple images here (i.e. not strongly lensed), the image planes are reconstructed as follows:

$$M_b(\boldsymbol{x}) = \sum_i \bar{S}_b(T_{\mathrm{d},i}, z_i, C_i) P_\nu(\boldsymbol{x} - \boldsymbol{r}_i) + B_b. \tag{3.1}$$

Here $M_b(\boldsymbol{x})$ is the reconstructed image for frequency channel b, $\boldsymbol{x}$ denotes the position within the image, $\bar{S}_b$ is the source flux density of source i averaged over the channel b transmission filter, $T_{\mathrm{d},i}$ is the dust temperature, z_i is the redshift, C_i is a normalisation factor of source i, $P_\nu(\boldsymbol{x} - \boldsymbol{r}_i)$ is the response function (i.e. the telescope beam), with $\boldsymbol{r}_i$ denoting the position of source i, and B_b is the image background. The response functions for the *Herschel* channels are approximated as Gaussians with FWHM values of 11.6, 18.1, 24.9 and 36.2 arcseconds at 160, 250, 350 and 500 μm, respectively (Griffin et al., 2010).

3.2.2 *Herschel*-SPIRE sky residuals

In M14, additional deep cosmological field imaging was used to estimate the covariance of the sky in the likelihood calculation. In this study, we are deblending the ALESS sources with the catalogue of nearby MIPS 24 μm and JVLA sources provided in Swinbank et al. (2014), henceforth referred to as the NMJS catalogue. This catalogue accounts for the majority of the flux in the *Herschel*-SPIRE data and thus, using a cosmological field without subtracted sources to estimate the covariance for our likelihood calculations is not appropriate here. Instead, we use the ECDFS SPIRE residuals, after subtracting our model SED, fit to every nearby source and ALESS source simultaneously.

A maximum likelihood method is used to fit our model SEDs using a similar method to that described in Section 3.2.3, weighting each pixel equally within the SPIRE data and ignoring any covariance between pixels. No PACS or ALMA data are used in this step. We limit this process to the region where the 250 μm instrumental noise is less than 1.2 mJy, which includes 4024 sources from both the ALESS and NMJS catalogues. Total flux densities from all sources combined of 37.2, 28.6 and 16.2 Jy are subtracted from the data at 250 μm, 350 μm and 500 μm, respectively. To test if we are over-subtracting flux from the maps, we stack the original maps on the positions of the catalogues, which produces total flux densities of 28.7±0.7, 23.4±0.6 and 14.5±0.5 mJy at 250 μm, 350 μm and 500 μm, respectively, with the errors estimated by bootstrapping. One might conclude that we are over-subtracting, but stacking on the model sky (the images subtracted from the data to produce the residuals) produces total flux densities of 30.5, 24.0 and 14.0 mJy at 250 μm, 350 μm and 500 μm, respectively. Both of these stacking results significantly lower than the total flux densities of the subtracted sources, however we only expect stacked results to equal the total flux densities of the sources if they are Poisson

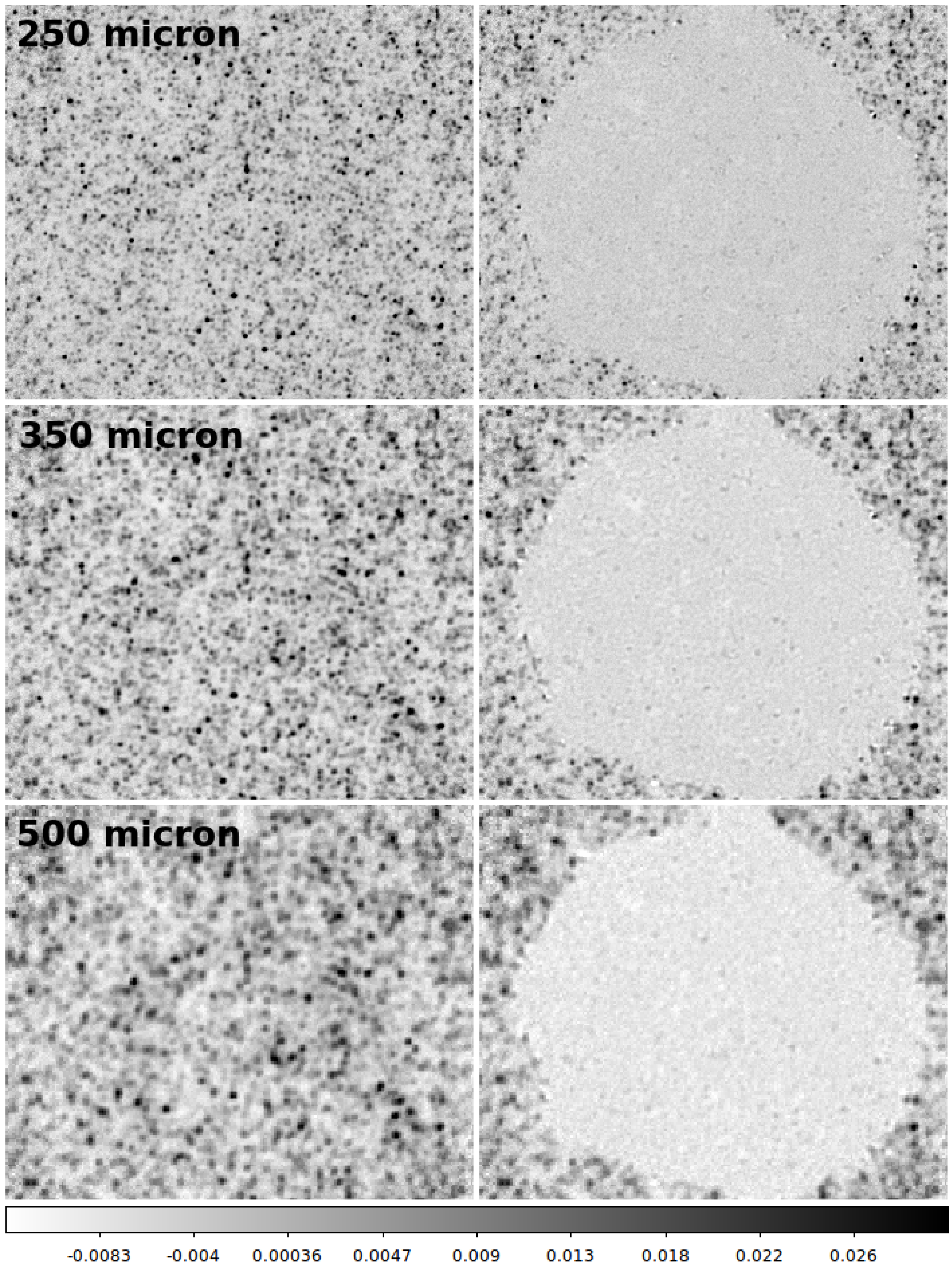

Figure 3.1: Left: SPIRE ECDFS field. Right: SPIRE ECDFS field, after source subtraction of 4024 sources in the region of the sky where the 250 μm instrumental noise is less than 1.2 mJy. The standard deviations of the residuals in the region of the subtraction are 1.5, 1.6 and 1.4 mJy at 250 μm, 350 μm and 500 μm, respectively. These residuals are larger than the instrumental noise and are presumably dominated by sources too faint to be included in the catalogue of sources subtracted. The scale at the bottom of the image is in Jy.

distributed on the sky (Marsden et al., 2009). Because the stacking on the real and model sky give consistent results, we conclude that we are not significantly over-subtracting flux from our maps.

The standard deviations of the residuals are 1.5, 1.6 and 1.4 mJy at 250 μm, 350 μm and 500 μm, respectively; significantly reduced from the confusion limits of 5.8, 6.3 and 6.8 mJy, respectively (Nguyen et al., 2010). These residuals are greater than the instrumental noise levels of 1.0, 1.1 and 1.2 mJy in these regions; we are thus seeing the residual confusion noise of the sources that are not bright enough to be included in the ALESS and NMJS catalogue of sources we subtracted. These residuals will be used in Section 3.2.3 to estimate the covariance of the sky. This method allows us to greatly reduce the effects of confusion noise; instead, we are left with degeneracies in SED fitting parameters among the many nearby sources in our catalogues.

3.2.3 Model fitting

As in M14, the model is fit to the data using an MCMC Metropolis-Hastings algorithm (Metropolis et al., 1953; Hastings, 1970) with Gibbs sampling (Geman and Geman, 1993). The log likelihood function for the *Herschel*-SPIRE data is

$$-\log L_{\mathrm{SPIRE}} = X_{\mathrm{SPIRE}} + \frac{1}{2}\boldsymbol{R}^{\mathrm{T}}\mathbf{C}^{-1}\boldsymbol{R}, \tag{3.2}$$

where $\boldsymbol{R}$ is a one-dimensional list of the residuals, and contains all three channels of SPIRE data ($\boldsymbol{R} = \{D_{250}(\boldsymbol{x}_k) - M_{250}(\boldsymbol{x}_k)/c_{250}, D_{350}(\boldsymbol{x}_k) - M_{350}(\boldsymbol{x}_k)/c_{350}, D_{500}(\boldsymbol{x}_k) - M_{500}(\boldsymbol{x}_k)/c_{500}\}$), $\mathbf{C}^{-1}$ is the inverse covariance matrix for the residuals, c_b are the calibration factors of each respective band, and X_{SPIRE} is a constant. For each step in the MCMC chain, we are only interested in the differences between log-likelihoods, thus any constants can be ignored.

In M14 the area of the sky used was only a few arcminutes across, but the method described here must function on much larger areas of sky and the above calculation time scales with the square of the area used. Fortunately, the covariance between pixels is only significant for nearby pixels, and so we do not need the whole matrix. We can estimate the covariance for an image of 10×10 pixels at each of the three SPIRE channels by selecting randomly chosen cutouts from the residuals described in Section 3.2.2. The covariance matrix is inverted and the result separated into six lists, corresponding to inverse covariances between pixels within the same waveband and between wavebands, which we then bin according to their angular separation on the sky. Where these bins are regular (due to the relative pixel sizes), we take the median value of values in each bin to obtain a better estimate of the inverse covariance. For inverse covariances between 250 μm and 350 μm, and 350 μm and 500 μm, a high-order polynomial is fit to the data (the pixel sizes of 6, 8.3 and 12 arcseconds do not form simple repeating angular separation bins between the wavelengths). Fig. 3.2 shows the inverse covariance as a function of angular separation for the six lists. If we limit the log-likelihood calculation to only pixels within a fixed radius of the sources of interest and between pixels within a fixed angular distance, the resulting likelihood calculation only scales with the area of sky used.

In practice, we could iterate on the process of making residual maps for use in estimating the residual sky covariance. Where we treated each pixel with equal weight in Section 3.2.2, we could instead use the estimated covariance from the previous iteration. In practice however, the computational time of the likelihood calculation would become prohibitively large compared to the simple approach we implemented. Fortunately, the residuals are likely dominated by sources

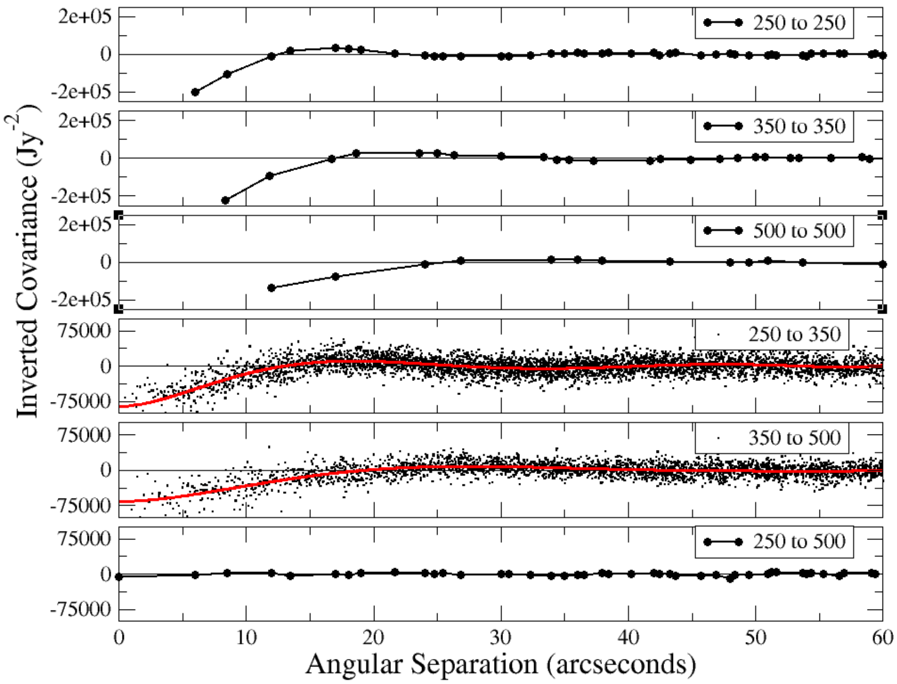

Figure 3.2: Results of separating the inverted covariance matrix of the *Herschel* SPIRE residuals by angular separation and by wavelength. The inverse auto-covariances for 250 μm to 250 μm, 350 μm to 350 μm, 500 μm to 500 μm at an angular separation of zero are 1.02×10^6, 1.07×10^6, and 7.9×10^6 Jy^{-2}, respectively, and are not shown on the graphs above for clarity.

too faint to be included in our NMJS catalogue, and not by a poorly weighted fit, and thus little would be gained by iterating on the residuals.

Flux calibration uncertainties, c_b, are taken into account during the fitting procedure by setting priors on c_b for each band. SPIRE waveband calibrations are correlated, with a covariance matrix

$$\mathbf{C}_{cal} = \begin{vmatrix} 0.001825 & 0.0016 & 0.0016 \\ 0.0016 & 0.001825 & 0.0016 \\ 0.0016 & 0.0016 & 0.001825 \end{vmatrix}, \tag{3.3}$$

where the calibration is normalised to unity (Bendo et al., 2013). This corresponds to a 4% correlated uncertainty between bands plus 1.5% uncorrelated uncertainty between bands.

The log-likelihood for the ALMA fluxes for a given band is given by

$$-\log L_{\rm b} = X_{\rm b} + \sum_i \frac{1}{2\sigma_{i,b}^2}(D_{i,b} - M_{i,b}/c_b)^2, \tag{3.4}$$

where $D_{i,b}$ is the measured flux density for source i, $\bar{M}_{i,b}$ is the model flux density for source i, $\sigma_{i,b}$ is the uncertainty in the measurement of $D_{i,b}$, c_b is the calibration factor, $X_{\rm b}$ is a constant, and b denotes the band of the measurement. Unlike the *Herschel* SPIRE bandpass filters, the ALMA bandpass filter is narrow and $\bar{M}_{i,b}$ is taken to be the flux density at the specified frequency. The data used in this study are 345 GHz ALMA Band 7, although we also consider the benefits of using additional 650 GHz Band 9 data for constraining the far-IR properties of the ALESS sample in Section 3.3.1. Calibration uncertainties are 10% and 20% in Bands 7 and 9, respectively (see Capabilities for ALMA Cycle 0).

Because the 160 μm PACS data are dominated by instrumental noise, the log-likelihood for these data is given by

$$-\log L_{\rm PACS} = X_{160} + \sum_i \frac{1}{2\sigma(\boldsymbol{x}_i)^2}(D_{160}(\boldsymbol{x}_i) - M_{160}(\boldsymbol{x}_i)/c_{160})^2, \tag{3.5}$$

where $D_{160}(\boldsymbol{x}_i)$ are the data, $M_{160}(\boldsymbol{x}_i)$ is the sky model, $\sigma(\boldsymbol{x}_i)$ is the instrumental error, X_{160} is a constant, c_{160} is the calibration factor, and $\boldsymbol{x}_i$ is the position of pixel i on the sky. The 160 μm PACS calibration uncertainty is 5% (Müller et al., 2011).

3.3 Testing with simulated sources

While we do not require simulation of artificial sources in order to calibrate our method, we can use it as a tool to verify the accuracy of the uncertainties reported. In particular, we can test how redshift, uncertainty in redshift, dust temperature and far-IR luminosity affect our ability to constrain these same properties. We can also explore the effects of including nearby sources and the generated degeneracies. In addition, we can quantitatively assess the benefits of adding further data, such as Band 9 ALMA measurements.

3.3.1 Verifying our method

We verify our method by injecting simulated sources into the residual *Herschel* SPIRE images, described in Section 3.2.2, along with simulated PACS data, and recording the resulting best-fit. The best-fit distribution of the injected sources should match the expected uncertainties for such sources. Simulated ALMA 870 μm flux densities are given 0.5 mJy Gaussian errors and the PACS 160 μm data are simulated by generating a blank image with Gaussian random noise equal to the instrumental noise. SPIRE calibration errors are randomly generated using the covariance matrix given in Section 3.2.3 and calibration errors for the ALMA and PACS data are also included. This is, in effect, a Monte Carlo verification of our method and allows us to verify the validity of our treatment of the *Herschel* SPIRE likelihood analysis. We adopt a "standard" source with a redshift of 2, a dust temperature of 30 K, and a far-IR luminosity of $10^{12}\,\mathrm{L}_\odot$, for the purpose of testing our method. This equates to flux densities of 4.5, 6.4, 7.6, 5.6, and 1.8 mJy at 160, 250, 350, 500, and 870 μm, respectively, with a peak flux density of 7.7 mJy at 323 μm. We inject a total of 441 fake sources for each case we test below. Injecting a single source at a time allows us to test our constraining power for a single isolated source (although this is a rare occurrence due to the density of sources on the sky). To see the effect of source confusion, we can injected multiple simulated sources in close proximity. Both of these cases are discussed below.

Because dust temperature and redshift are entirely degenerate, it would be possible to constrain $T_{\rm d}/(1+z)$, instead of fixing the redshift and constraining dust temperature separately, as is done in most of the examples below. However, because we have redshift estimates for all the ALESS sources, we think it is more beneficial to show constraints on dust temperatures separately. The effect of an uncertainty in redshift is also explored below, but separately (see Fig. 3.7).

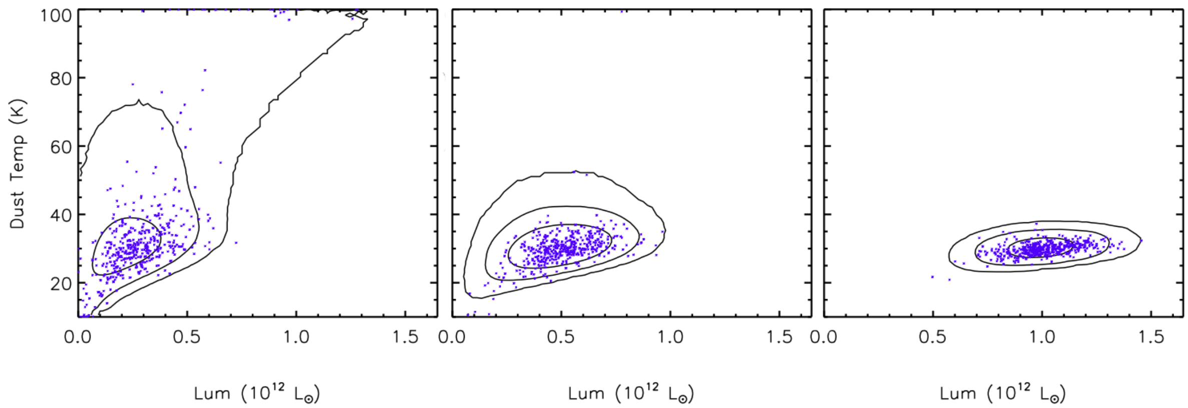

Figure 3.3: Results comparing the expected uncertainty in fitting a source given by our method (black contours), versus Monte Carlo simulated sources injected into the data. The blue points are the Monte Carlo simulated sources used to verify our method. In the right panel, we show our standard source with a redshift of 2, a dust temperature of 30 K and a far-IR luminosity of 10^{12} $L_\odot$. In the middle panel we show the same standard source with half the luminosity, and in the left panel, the standard source with a quarter of the original luminosity. The black contours represent 68%, 95% and 99.7% credible regions

Fig. 3.3 shows the verification of our method for our standard source, as well as the cases where we decrease its luminosity by a factor of two and by a factor of four. Good agreement is found between our expected uncertainties and the Monte Carlo injected sources. It is interesting to see the drastic change in temperature uncertainty as the luminosity of the standard source is reduced. We could clearly provide good constraints on sources to well below the confusion limit of the SPIRE data, if only we had isolated sources on the sky. Of course this is just a tautology, since the sky is unfortunately a crowded place and our ability to constrain the properties of sources is largely limited by nearby sources that generate degeneracies in the fit parameters.

Fig. 3.4 shows the verification of our method for the case of two standard sources separated by 5 arcseconds. This example demonstrates a typical case of submm multiplicity as seen for many of the ALESS sources (Hodge et al., 2013). Here, it is clear that the constraints on the properties of a source are limited by the degeneracies with its neighbour and not the residual unresolved far-IR background. A linear degeneracy between the two far-IR luminosities is expected, with the one-to-one degeneracy seen here the result of the two sources having the same far-IR luminosity and redshift. The degeneracies seen between the other SED model parameters, typically "banana-shaped," depend on the values of the parameters themselves. It is these degeneracies that two-step SED fitting misses. Again, our Monte Carlo simulated sources accurately reflect the expected uncertainties.

Fitting large numbers of Monte Carlo simulated sources is a computationally expensive exercise and thus we stop the verification of our method here. We have shown that the constraints produced by our method accurately reflect the results of Monte Carlo simulations, and thus our treatment of the SPIRE likelihood analysis is validated. For a standard source, Fig. 3.5 shows the difference between our approach and an identical method where we only consider the instrumental noise of the SPIRE data and ignore the correlations between neighbouring pixels in angular separation as well as between wavelengths. Without our treatment of the SPIRE likelihoods, it is clear that we would be over-constraining the properties of sources within our model.

Assigning a realistic dust temperature is an issue that has been neglected in much of the

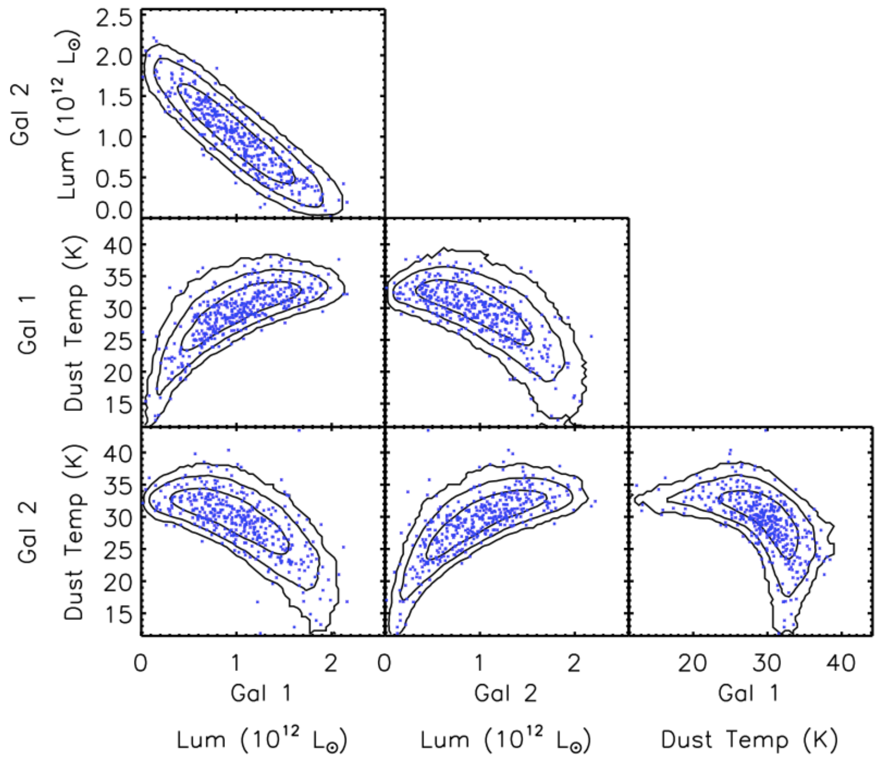

Figure 3.4: Comparing the expected uncertainties for two standard sources separated by five arcseconds with the Monte Carlo simulated results (blue points). The black contours represent 68%, 95% and 99.7% credible regions.

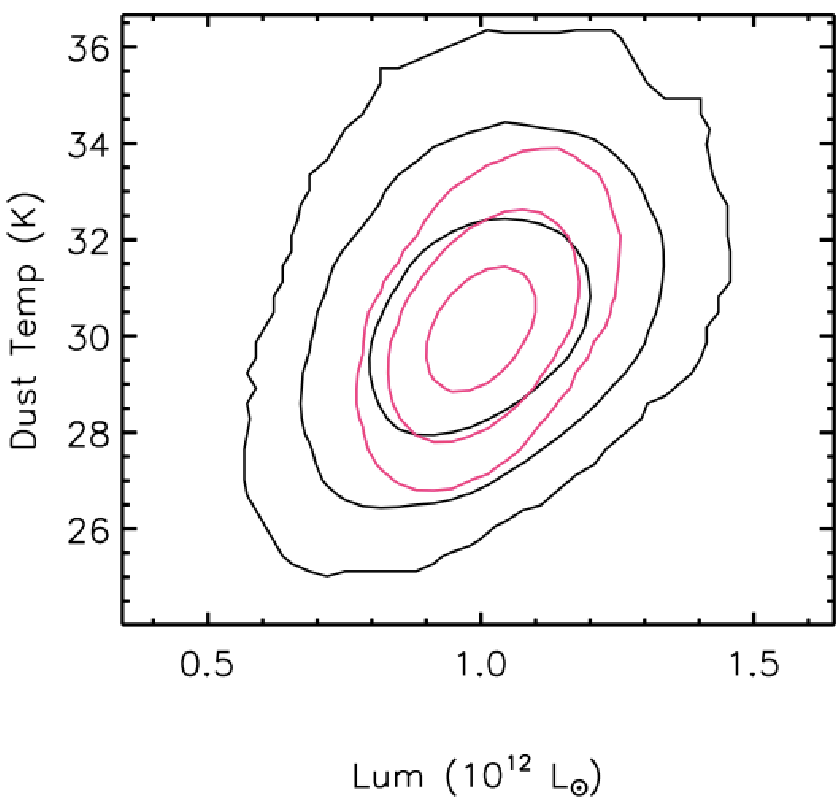

Figure 3.5: Comparing the expected uncertainties for a standard source using our method (black contours show 68%, 95% and 99.7% credible regions) and an identical method with a naive approach of the *Herschel* SPIRE likelihood that considers only the instrumental noise in each pixel and ignores the covariance with neighbouring pixels (red contours).

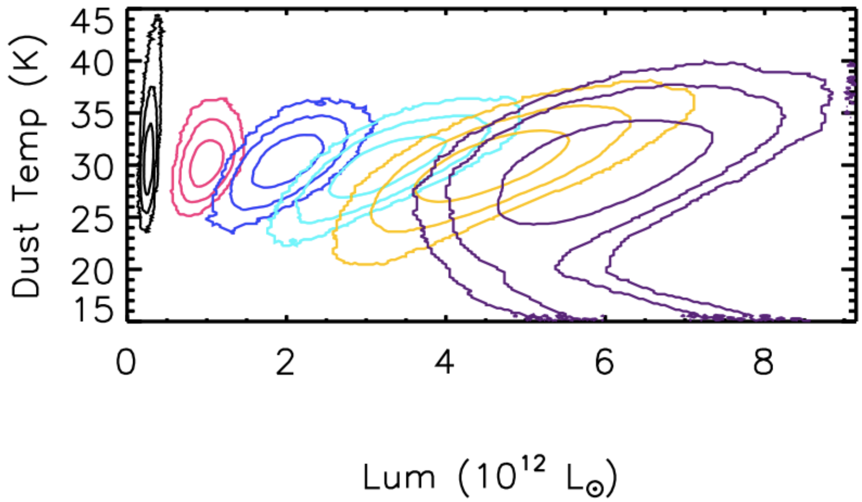

Figure 3.6: Constraining power of our model as a function of redshift for our standard source while keeping peak flux density constant. We show 68%, 95% and 99.7% credible regions for redshifts of 1, 2, 3, 4, 5 and 6 in black, red, blue, green yellow and purple, respectively.

literature. Constraints on dust temperature are affected by several factors, such as the redshift of the source, the width of the telescope bandpass filters, the wavelength coverage of the telescope filters, and the signal-to-noise of the source within the images. However, the dust temperature uncertainty naturally falls out of the method employed here, and thus we perform a few tests as examples.

Fig. 3.6 shows how our constraints change as we vary the redshift of our standard source while keeping the peak flux density constant and letting the far-IR luminosity change. An interesting effect is seen at high redshift, where a colder fit to the dust temperature starts to increase the far-IR luminosity. This is because the peak of the SED shifts beyond the ALMA 870 μm waveband. A similar effect is seen at low redshifts, when the peak of the SED shifts to wavelengths shorter than 160 μm and the upper dust temperature bound starts to rise. For a dust temperature of 30 K, these effects do not become significant unless the redshift is lower than about 1 or greater than about 6, thus the wavelength coverage of the available data is ideally suited for the sample of ALESS sources we are fitting in Section 3.4.

Up to this point, we have assumed that the redshift of our standard source was well constrained. Fig. 3.7 shows our model constraints for redshift uncertainties of 0, ± 0.5, and ± 1. How well we can constrain dust temperature and far-IR luminosity, along with degeneracies among nearby sources, strongly depends on the uncertainty in source redshift.

3.3.2 The addition of a second ALMA frequency

ALMA follow-up of 870 μm sources selected from ALESS (Weiß et al., 2009; Hodge et al., 2013) have shown that a significant fraction of single-dish detected sources are in fact comprised of multiple galaxies. Since degeneracies with nearby sources are a dominating factor in determining our ability to constrain their far-IR properties (see Fig. 3.4), such sources will have particularly poor constraints on their far-IR properties. In Fig. 3.8 we explore the benefits of adding ALMA Band 9 observations at 460 μm, with an rms of 1 mJy, for the case of two standard sources

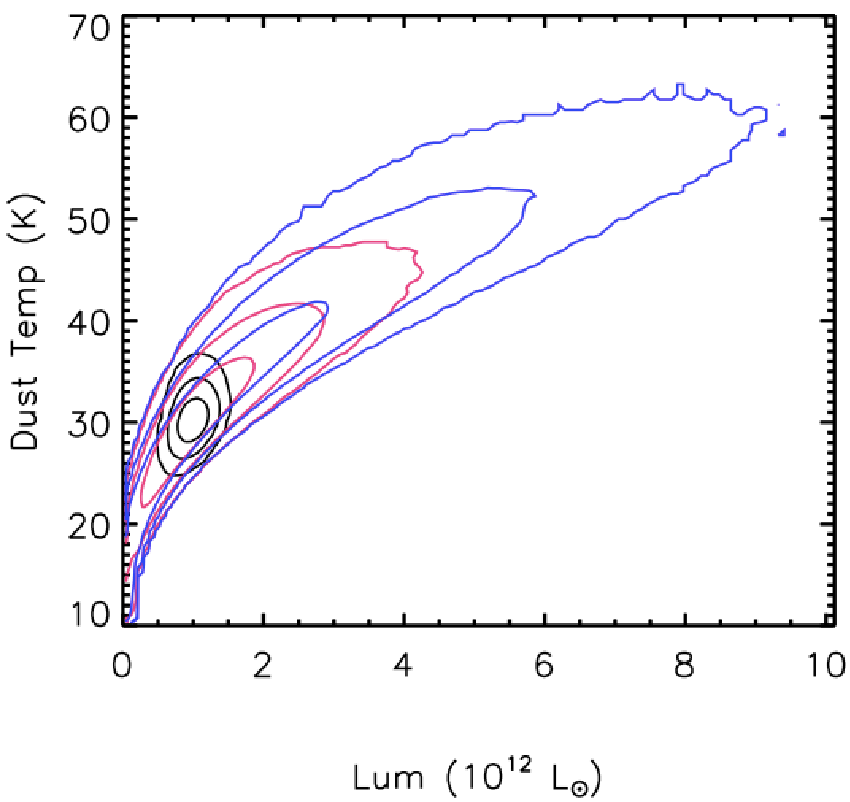

Figure 3.7: Constraining power of our model for the case of varying redshift uncertainty. Here, 68%, 95% and 99.7% credible regions are shown for redshift uncertainties of 0, ±0.5 and ±1, in black, red and blue contours, respectively. A large uncertainty in redshift is one of the main limitations for constraining dust temperature,as well as far-IR luminosity.

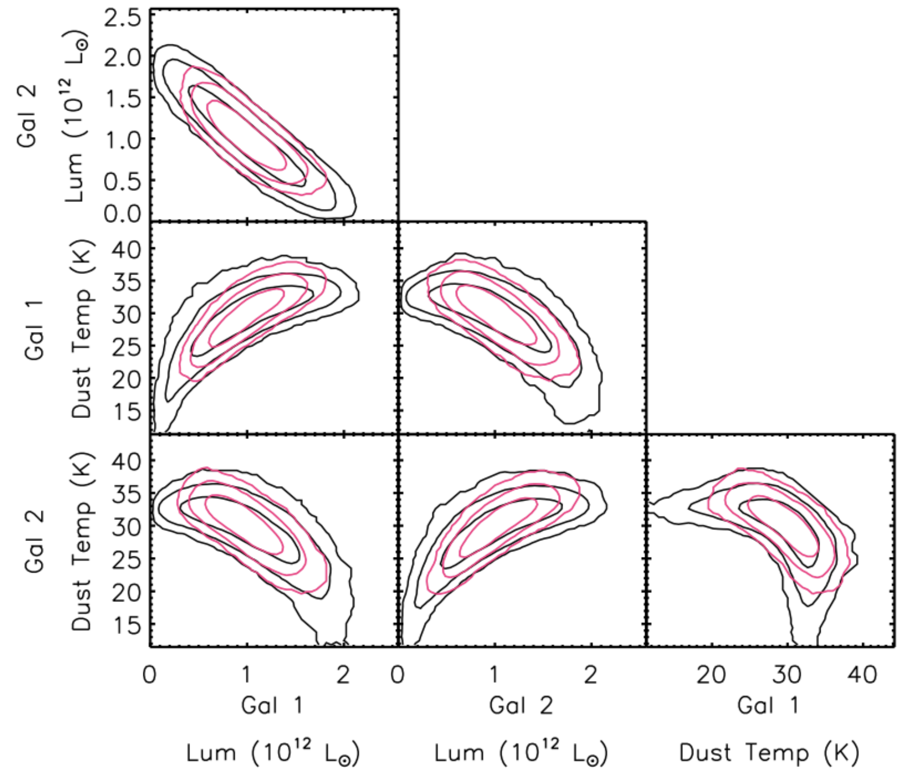

Figure 3.8: Constraining power of our model for the case of two standard sources separated by 5 arcseconds. The black contours denote 68%, 95% and 99.7% credible regions using 0.5 mJy rms 870 μm ALMA Band 7 observations, while the red contours are when 1 mJy rms 460 μm ALMA Band 9 observations are added along with 870 μm ALMA Band 7 observations.

separated by 5 arcseconds on the sky. Since the peak of the SED for our standard source is at 323 μm, which is shorter than both the ALMA wavelengths considered, only moderate improvement in constraining power is expected, and this is what is seen in the simulations. Specifically, the lower bound on the temperature is improved, which in turn improves the constraint on far-IR luminosity. Much bigger improvements in constraining power are realised when the peak of the SED is straddled by the two ALMA wavelengths, as would be the case if our standard source were at a higher redshift or had a lower dust temperature. Fig. 3.9 shows the improvement for the case of two standard sources separated by 5 arcseconds, where the standard sources are moved to a redshift of 4 and their peak flux densities remain unchanged. In this case, degeneracies between the two sources are nearly eliminated when adding a second ALMA band.

3.4 The properties of submm galaxies within the ALESS survey

When fitting our model to the data, we use the ALMA 870 μm fluxes and positions from Hodge et al. (2013) and the photometric redshift estimates of Simpson et al. (2014), which were used by Swinbank et al. (2014). The photometric redshift constraints are considered to be $\pm 1\,\sigma$

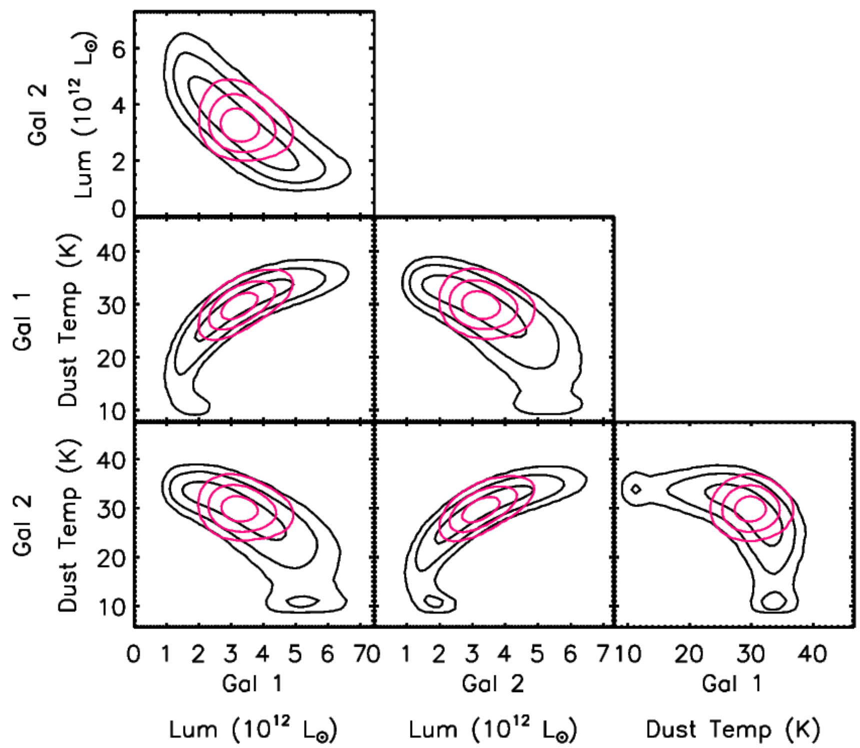

Figure 3.9: Constraining power of our model for the case of two standard sources, moved to a redshift of 4, while keeping the same peak flux density, and a separation of 5 arcseconds. The black contours denote 68%, 95% and 99.7% credible regions using 0.5 mJy rms 870 μm ALMA Band 7 observations, while the red contours are when 1 mJy rms 460 μm ALMA Band 9 observations are added along with 870 μm ALMA Band 7 observations.

Gaussian priors in our model. As in Swinbank et al. (2014), we treat any source in the NMJS catalogue as a duplicate if it is within 1.5 arcseconds of an ALESS or another NMJS source.

We found that our data have almost no constraining power on the dust emissivity, β, when it is allowed to range over $1.0-2.5$, and thus we simply fix it to a nominal value of 1.5 so that we may easily compare the ALESS sample with the sample of Symeonidis et al. (2013). We set a hard prior on the dust temperature such that it must be above 10 K, since no colder galaxies have been found in any similar surveys (e.g. Dale et al., 2012; Amblard et al., 2010; Symeonidis et al., 2013). This hard prior is useful for when the peak of the SED is shifted close to, or beyond, the ALMA 870 μm wavelength, which occurs at high-redshifts when the source is cold (see Fig.3.6); thus this prior keeps the model from entering an unphysical region of parameter space. We also use a hard prior to keep the dust temperature from going beyond 100 K, since no source in the ALESS sample was found to be this warm by Swinbank et al. (2014).

We report the median values of our MCMC chains and report 68% credible intervals throughout. Far-IR luminosities are calculated by integrating the model SED from 8 to 1000 μm. When either the dust temperature or far-IR luminosity lower credible interval are consistent with either zero far-IR luminosity or 10 K for dust temperature, we report the upper 84% credible interval as an upper limit. Note that because of our prior on dust temperature, upper limits for dust temperature are somewhat subjective in that the upper limit would move if we changed the dust temperature prior. While we may only have upper limits in one of these parameters, this does not necessarily translate into an upper limit on the other. In fact, for only one case do we have an upper limit on both far-IR luminosity and dust temperature. The resulting far-IR luminosity and dust temperature constraints are given in Table A.1. Note that we do not report any constraints for ALESS083.4, since the redshift of the source puts the peak of the SED shorter than the available data and thus no constraints on dust temperature or far-IR luminosity are possible.

3.4.1 Comparison with Swinbank et al. (2014)

The benefit of applying our method to this sample of ALESS sources is that we can compare our results with those of Swinbank et al. (2014), who employed a modern competing method of deblending and SED fitting. To facilitate the comparison, we have used much of the same data, although there are also key differences that make a detailed comparison less than straightforward. To facilitate the comparison, we have used the same ALESS catalogue of positions and flux densities (Hodge et al., 2013), the same NMJS catalogue, the same *Herschel*-SPIRE and PACS 160 μm data, and the same redshift estimates (Simpson et al., 2014). Aside from the method used to deblend the *Herschel* data, important differences include the use of an SED library and the inclusion of both shorter and longer wavelength data when fitting SEDs (see Swinbank et al., 2014).

Fig. 3.11 compares the results of our two methods to assess their level of agreement. The black dashed line in both plots shows the locus representing complete agreement, and the Swinbank et al. (2014) dust temperatures used in the comparison are those that were derived from fitting a modified blackbody to the *Herschel* photometry. We use a fixed dust emissivity index of 1.5, primarily so that we may also compare our results with those of Symeonidis et al. (2013). An apparent systematic shift towards hotter dust temperatures is seen for our results of around 4 K; however, comparing dust temperatures requires knowledge the SED used to fit the data and any priors on the dust emissivity. We found that using a dust emissivity of ~ 1.9 would eliminate this systematic, however Swinbank et al. (2014) allowed the dust emissivity to vary between 1.5 and 2.2 and found an average best fit value of 1.8, thus this dust temperature discrepancy is mostly due to a difference in dust emissivity. When we allow the dust emissivity to vary freely between 1 and 2.5, we found that the data had almost no constraining power on the dust emissivity.

When comparing the far-IR luminosities, a clear correlation can bee seen between the two methods with a slight tendency for our method to fit higher far-IR luminosities for more luminous objects and and lower far-IR luminosities for less luminous objects. Again, the choice of specific SED model will affect results here, primarily the lack of a shorter wavelength hot component to our SED model, as well as the use of shorter and longer wavelength data used by Swinbank et al. (2014). Such a comparison would require us to develop a more complicated SED model that would allow us to incorporate these other wavelengths.

Overall, we believe our method to be an improvement over what has been used in many previous studies of submm galaxies and its effectiveness has been shown in Section 3.3.1. It forgoes the need to deblend confused imaging prior to fitting SEDs; Our method fits SEDs and deblends the images simultaneously and harnesses prior knowledge of the expected source SED shape.

3.4.2 Dust temperatures and selection effects for ALESS sources

The top panel of Fig. 3.10 plots the dust temperature versus far-IR luminosity for the ALESS sample. Many previous studies showed a correlation between dust temperature and far-IR luminosity (the L–$T_{\rm d}$ relation, e.g. Chapman et al. (2005); Magnelli et al. (2012); Casey (2012); Symeonidis et al. (2013)), although some authors have noted that many of these studies are biased by selection effects (e.g. Chapin et al., 2009, 2011; Swinbank et al., 2014). Over-plotted on the top panel of Fig. 3.10, using a solid black line, is the L–$T_{\rm d}$ relation as found by Symeonidis et al. (2013). The sample of sources used to find this relation were specifically chosen with the aim of minimising selection effects and are likely the most accurate representation of the L–$T_{\rm d}$ relation in the literature. A major result of Symeonidis et al. (2013) is that sources at $z < 0.1$ are on average a few Kelvin warmer than those with redshifts ranging from 0.1 to 2. For our study, we have specifically chosen a value of the dust emissivity that allows us to compare our results directly to those of Symeonidis et al. (2013), to test if dust temperature evolves further at higher redshifts. Upon first inspection, it would appear that the ALESS sources are indeed cooler, however, we must consider the selection effects of our sample. In the top panel of Fig. 3.10, the red and purple, dot and dashed lines, denote representative ALMA $3.5\,\sigma$ detection limits for redshifts of 1, 3, 5, and 7. In the region where our two samples overlap, it is clear that these detection limits bias our sample to cooler temperatures.

To test whether or not our sample is indeed cooler, we devise a method of applying the ALESS sample selection effects to the Symeonidis et al. (2013) sample. We obtained the catalogue of sources used to create the estimate of the L–$T_{\rm d}$ relation of Symeonidis et al. (2013) (solid black line in Fig. 15), including source far-IR luminosities and dust temperatures. We randomly draw n objects from this source list, where n is the number of sources in the list, with replacement. We randomly assign to these sources, redshifts from the ALESS source catalogue, such that they will have the same redshift distribution. We retain those sources that have a predicted flux density greater than the $3.5\,\sigma$ ALMA flux limit at $870\,\mu$m and calculate the mean dust temperature of this sample of sources. We perform this procedure many times, thus bootstrapping the sample, and restrict our test to sources with luminosities between 10^{12} and $10^{13}\,{\rm L}_\odot$ (where the two samples overlap). We find a mean dust temperature of (35.6 ± 0.8) K. Using a similar procedure, we find a mean dust temperature of (33.9 ± 2.4) K for the ALESS sample. Since these values are completely consistent, we cannot conclude that we detect any

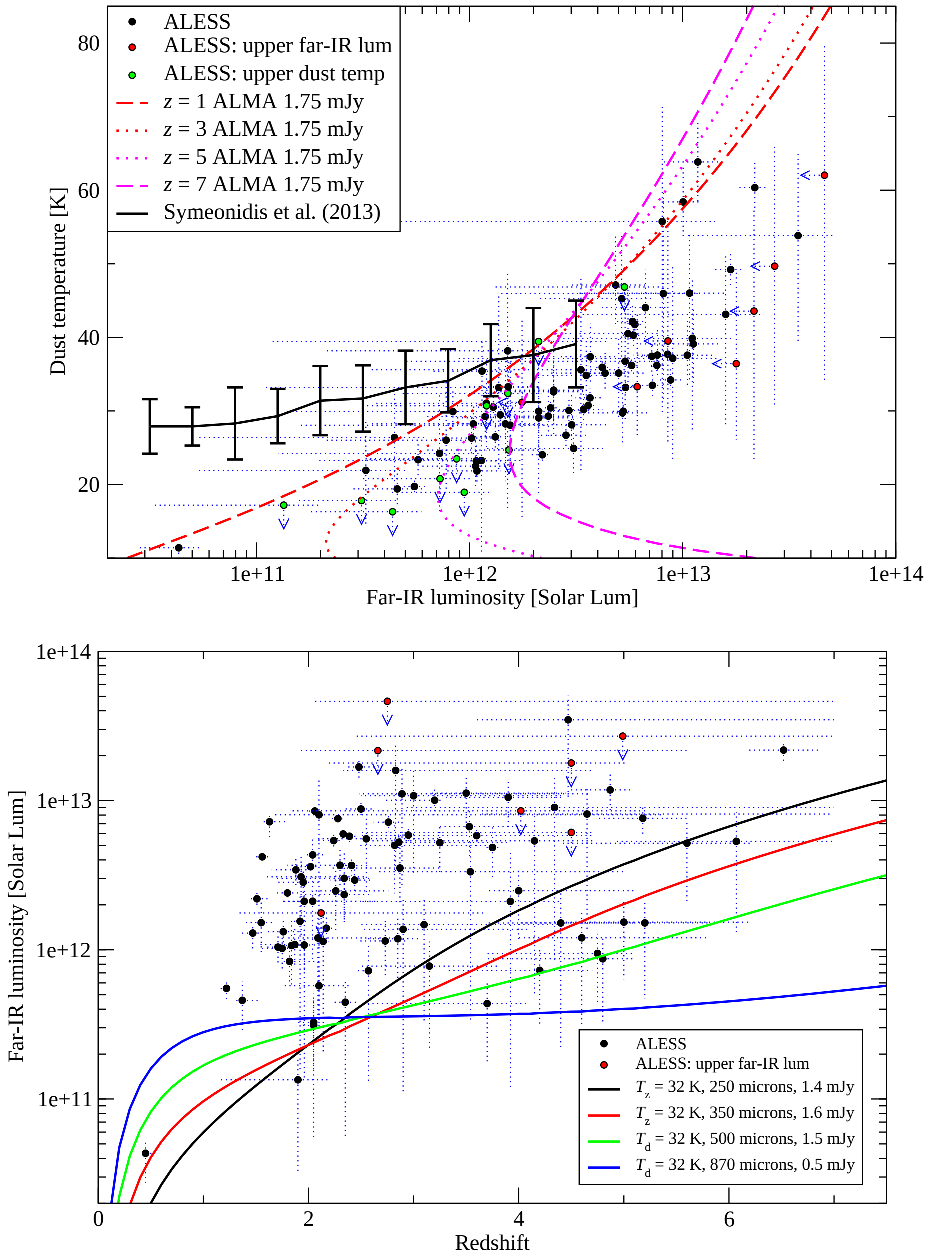

Figure 3.10: *Top*: Dust temperature vs far-IR luminosity for the ALESS sample. Black points are ALESS sources with constraints on both the far-IR luminosity and dust temperature. Red points are ALESS sources with $1\,\sigma$ upper limits on far-IR luminosity. Green points are ALESS sources with $1\,\sigma$ upper limits on dust temperature. Dot and dashed lines are representative $3.5\,\sigma$ detection limits of the ALMA data for redshifts between 1 and 7. The solid black line is the far-IR luminosity to dust temperature relation found by Symeonidis et al. (2013). It is clear from the detection limits that our sample is biased towards colder dust temperatures. *Bottom*: Far-IR luminosity vs redshift for the ALESS sample. The colour of the points denote the same objects as above. Representative $1\,\sigma$ detection limits are drawn for a $T_{\rm d} = 33\,$K source for 250, 350, 500 and 870 μm in black, red, green, and blue, respectively. ALESS sources with upper limits on dust temperature can be found in the region between the ALMA and *Herschel* SPIRE detection limits, implying a detection by ALMA, but little or no flux seen by *Herschel* SPIRE.

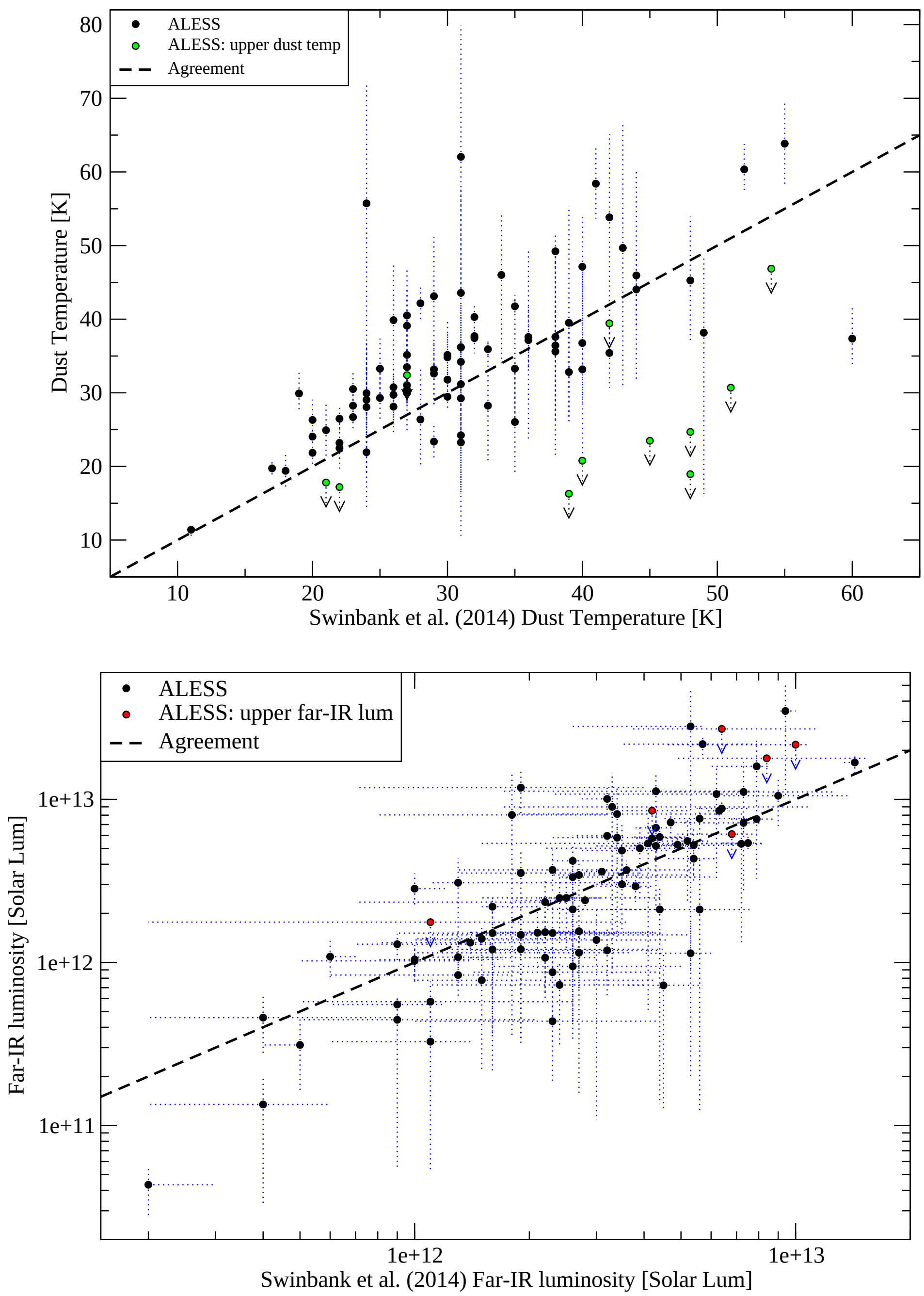

Figure 3.11: A comparison of our results with those found by Swinbank et al. (2014). *Top*: comparison of dust temperatures between the two methods. *Bottom*: Comparison of far-IR luminosities. Black points are ALESS sources with constraints on both the far-IR luminosity and dust temperature. Red points are ALESS sources with 84% upper limits on far-IR luminosity. Green points are ALESS sources with 84% upper limits on dust temperature. The dashed black line shows the expected relation if the two methods were in agreement. While our results show a clear correlation with those found by Swinbank et al. (2014), there is disagreement for many of the ALESS sources. One prominent feature appears to be roughly a 4 K offset in temperature between the two methods. This discrepancy is explained by a difference in dust emissivity used.

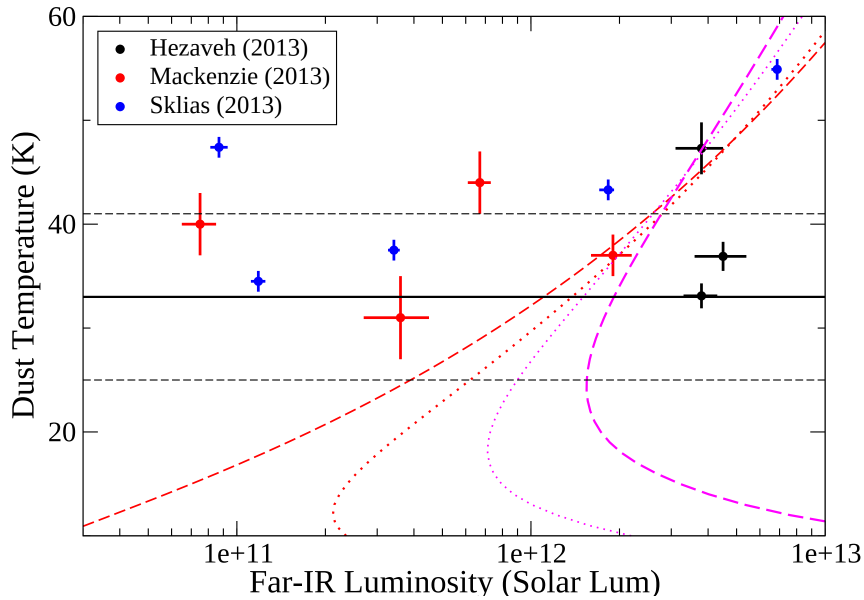

Figure 3.12: Dust temperature versus far-IR luminosity for a sample of lensed submm galaxies (MacKenzie et al., 2014; Sklias et al., 2014; Hezaveh et al., 2013). The black line denotes the average dust temperature of the ALESS sample with the ± 8 K standard deviation shown as the black dashed lines. Red and purple dot and dashed lines are representative $3.5\,\sigma$ detection limits of the ALMA data for redshifts of 1, 3, 5, and 7.

evolution in dust temperature with redshift in the ALESS sources when compared to those of Symeonidis et al. (2013). The selection effects of the ALESS sample unfortunately preclude any attempt at performing this same test for those sources with $z < 0.1$.

Instead of going deeper, a useful way to probe the L–$T_{\rm d}$ relation for fainter sources at high redshift is to use strong gravitational lensing. The particular striking case of a strongly lensed galaxy group at $z = 2.9$ was presented in Chapter 2 and is another example of source multiplicity. Along with the lensed sources of Sklias et al. (2014), we have examples of seven high redshift sources in the region of the L–$T_{\rm d}$ plane excluded by the ALMA selection effects, five of which have dust temperatures warmer than the average of the ALESS sample. Fig. 3.12 shows these sources along with sources from Hezaveh et al. (2013), which although fainter, would be bright enough to be included in the ALESS catalogue. The solid and dashed lines denote the 34.6 K average temperature and 8 K standard deviation of the ALESS sample. This supports our conclusion that selection effects drive the L–$T_{\rm d}$ to apparently lower temperatures.

3.4.3 Contribution to the co-moving star formation rate density of the Universe

Fig. 3.13 shows the co-moving SFR density for the ALESS sources with flux densities greater than 4.2 mJy, using a conversion factor of $1.08 \times 10^{-10} \mathrm{M}_{\odot}\mathrm{yr}^{-1}\mathrm{L}_{\odot}^{-1}$ for a Chabrier IMF, as in Swinbank et al. (2014). The vertical error bars on our results are 68% confidence intervals for the co-moving SFR density after bootstrapping the MCMC chains and the horizontal error bars are the 16th and 84th percentile of the redshift distribution used to generate each data point, with the data point being plotted at the 50th percentile of the redshift distribution used within that bin. For comparison, the points plotted from Swinbank et al. (2014) are divided

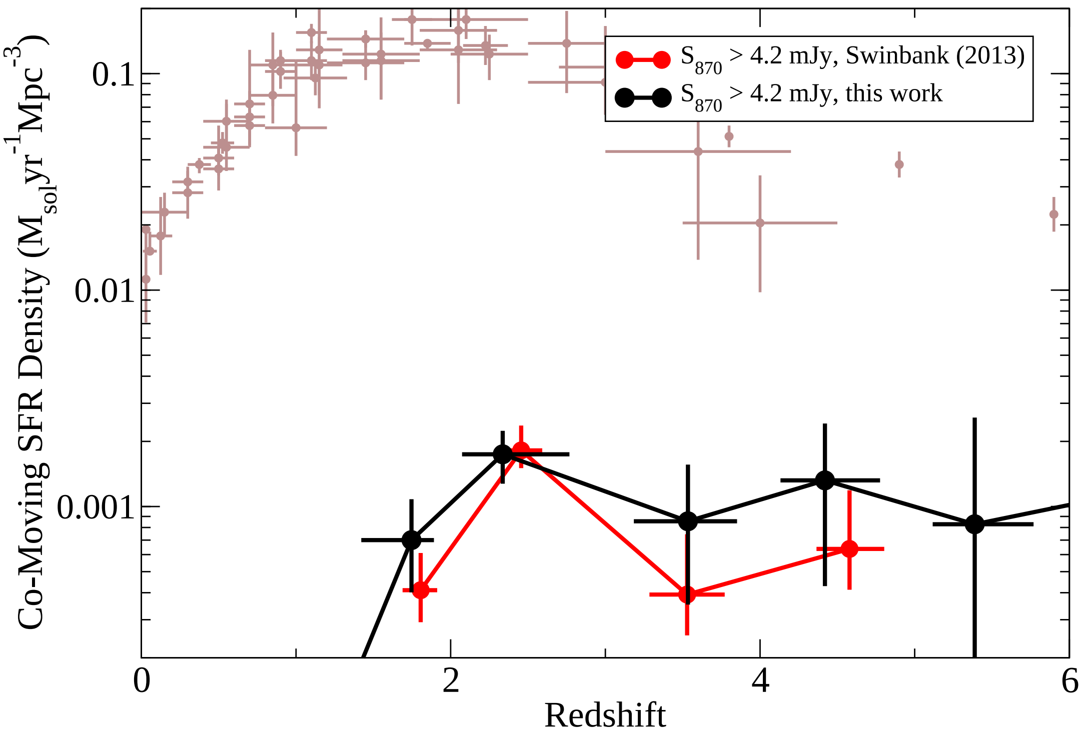

Figure 3.13: Contribution of the ALESS sources with flux densities greater than 4.2 mJy to the co-moving star formation history of the Universe. The vertical error bars on our results are 68% confidence intervals for the co-moving SFR density after bootstrapping the MCMC chains and the horizontal error bars are the 16th and 84th percentile of the redshift distribution used to generate each data point, with the data point being plotted at the 50th percentile of the redshift distribution used within that bin. For comparison, we include the data points from Swinbank et al. (2014), divided by a factor of 2, which they use to correct their estimate, as the region is though to be under dense (Casey et al., 2009).

by a factor of 2, which they use to correct their estimate, as the region is though to be under dense (Casey et al., 2009). Although our competing methods may produce significantly different far-IR constraints for individual sources, this particular measurement agrees rather well with those of (Swinbank et al., 2014). As such, we refer the reader to Swinbank et al. (2014) for interpretations and extrapolations for this particular metric of the data.

3.5 Conclusions

After generalising our method from Chapter 2 for the case of deblending SEDs of confused point sources, we were able to show that our method gives realistic estimates of far-IR properties and their uncertainties and accurately captures the degeneracies among SED parameters of nearby sources caused by confusion. When applied to the ALESS catalogue, we were able to give constraints on dust temperatures and far-IR luminosities and show that our results correlate with those of Swinbank et al. (2014), although our derived far-IR properties differ significantly when comparing individual sources. *Herschel* SPIRE currently provides the best view of the 250, 350 and 500 μm extragalactic sky in terms of depth and sky coverage. The majority of these data are confusion limited, yet many of the methods being used . Using the sample of Symeonidis et al. (2013) and applying the same selection function as the ALESS sample, we were able to show that any evolution of the L–$T_{\rm d}$ relation to cooler dust temperatures at high redshifts, are indistinguishable from selection effects.

With the large quantities of confusion limited imaging now available, such as that from *Herschel*, applications of our method are many. One possibility is obvious: the co-moving SFR density of the Universe as seen within the Hubble Ultra Deep Field (HUDF). Confusion limited *Herschel*-SPIRE imaging for this field are already available, and in Section 3.3.2 we showed how ALMA observations at more than one frequency can greatly aid in deblending SEDs. Combining these observations with the spectroscopic and photometric catalogues that currently exist would yield worthwhile results.

Chapter 4

SCUBA–2 follow-up of candidate Planck proto-clusters

4.1 Introduction

New submm observatories, such as the JCMT (Holland et al., 1999), BLAST(Pascale et al., 2008) and *Herschel* (Pilbratt et al., 2010a), have allowed us to view larger and larger portions of the submm sky to greater and greater depths, continually improving the statistics on this relatively new population of sources. Of particular interest is the role of these sources in their contribution to global star formation rates (SFR) and the driving force behind their intense star formation. While some may be triggered by mergers(e.g. Sanders and Mirabel, 1996), others may simply be at the bright end of what have been named the "main sequence" of galaxies (Noeske et al., 2007; Daddi et al., 2007; Elbaz et al., 2011b). While most wide-field cosmology surveys try to characterise this population as a whole, it is important to consider the effects of galaxy environment on star formation. Due to detection techniques, most known clusters are at redshifts below that of the peak of star formation, and their star formation has been quenched through various physical processes, although galaxies falling into their gravitational potential wells for the first time may still experience an increase in star formation (Verdugo et al., 2008; Braglia et al., 2009, 2011). Those clusters detected through the Sunyaev-Zeldovich effect, while redshift independent above $z \sim 0.25$, require the presence of hot intra-cluster plasma (Zeldovich and Sunyaev, 1969; Sunyaev and Zeldovich, 1970). This technique has been used to detect hundreds of clusters out to $z \sim 1.5$ (e.g. Planck Collaboration VIII, 2011; Hasselfield et al., 2013; Planck Collaboration XXIX, 2014; Planck Collaboration XX, 2014; Bleem et al., 2015).

A complementary high-z cluster detection technique is to look for regions of exceptional star formation. Due to the density of such objects on the sky, large areas must be probed in order to find a significant sample, thus all-sky surveys are needed. *Planck* (with its 5 arcminute beam that closely matches the expected size of a forming galaxy cluster at $z \sim 2$–4), along with its all-sky coverage, makes it a good observatory for finding such objects. Thus, the search was performed and the first results can be found in Planck Collaboration XXVII (2015) and Cañameras et al. (2015).

Two methods were used to generate a list of potential high-z targets to follow-up with *Herschel* (see Planck Collaboration XXVII 2015 and Planck Collaboration XXXIX 2015 for details). The first uses CMB and Galactic-cirrus cleaned *Planck* maps at 353, 545 and 857 GHz, using only 26% of the sky which is the least contaminated by Galactic sources. S/N > 5 sources are identified in a 545 GHz excess map, defined to be the 545 GHz map with a linear interpolation between the 353 and 857 GHz maps subtracted. On top of this, S/N > 3 detections are required at 353, 545 and 857 GHz. To remove cold Galactic cores and extragalactic radio sources, only sources with $S_{545}/S_{857} > 0.5$ and $S_{353}/S_{545} < 0.9$ are retained. The second method used The Planck Catalogue of Compact Sources (PCCS, Planck Collaboration XXVIII, 2014) and a selection method based on the work of Negrello et al. (2010b). Here, 52% of the sky is used based on the 857 GHz Galactic mask, and sources with S/N $>$ 4 at 545 GHz are selected from the catalogue. From this list, sources are only retained with $S_{857}/S_{545} < 1.5$ and $S_{217}/S_{353} < 1$, and which are not identified as a local galaxy, a bright radio source or Galactic cirrus in either the NASA/IPAC Extragalactic Database (NED), ALADIN, or IRAS maps. The result is a list of over 2000 high-z candidate sources, selected to have apparent redshifted flux densities peaking between 353 and 857 GHz. Included in this is a combination of strongly lensed sources, proto-clusters undergoing massive starbursts, chance overdensities of star forming galaxies, and perhaps a few Galactic interlopers. The fraction of objects in the various categories is currently unknown, which is why follow-up observations are critical.

A total of 228 of these candidates were observed by *Herschel* using the Spectral and Photometric Imaging Receiver Griffin et al. (SPIRE, 2010). This instrument, with a beamsize 16 times smaller than *Planck*'s, has the ability to resolve the *Planck* candidates into either single bright point-sources or overdensities within the *Planck* beam. The former were shown to be among the brightest strongly lensed sources on the sky by Cañameras et al. (2015); 11 out of 15 of these bright sources were followed-up (two were previously known (Fu et al., 2012; Combes et al., 2012) and two are in the far south) with a host of instruments, including SCUBA-2 at 850 μm, spectroscopic observations using the wide-band heterodyne receiver Eight MIxer Receiver (EMIR) at the Institut de Radioastronomie Millimétrique telescope (IRAM) and SMA 850 μm interferometry to confirm their lensed nature. Their redshifts range from 2.2 to 3.6, with peak flux densities ranging from 0.35 to 1.14 Jy, and they have apparent far-IR luminosities up to $3 \times 10^{14}\,\mathrm{L}_{\odot}$. Due to their extra-ordinary flux densities and far-IR luminosities, these sources have been aptly named "*Planck*'s dusty GEMS" (Gravitationally Enhanced subMillimetre Sources).

The first results covering the overdensity fields are presented in Planck Collaboration XXVII (2015). They find significant enhancements in the surface density of sources at 350 and 500 μm, with the majority of sources peaking at 350 μm. Assuming an average dust temperature of 35 K, they find a typical redshift of 2 for the overdensity fields with average far-IR luminosities of around $4 \times 10^{12}\,\mathrm{L}_{\odot}$ per SPIRE source. These overdensities may be high redshift proto-clusters undergoing rapid starformation, although they may also be chance line-of-sight alignments. Without spectroscopic redshift estimates of the objects within these overdensities, it is impossible to distinguish between these two possibilities.

The analysis here focuses on the SCUBA-2 observations, based on 61 of the 228 *Herschel* fields that have been followed up with 850 μm observations at the JCMT. 11 of these fields are observations of *Planck*'s dusty GEMS and are detailed in Cañameras et al. (2015). The 51 overdensity fields are discussed here. The more favourable "k-correction" (A method of correcting the measured flux density of an object for the effects of redshift, given that we are observing an intrinsically brighter region of the SED; Franceschini et al., 1991; Blain and Longair, 1993) at 850 μm means that we have a significantly less biased view on the redshift distribution of the overdensity fields than *Herschel* and a greater sensitivity for sources at redshifts $\gtrsim 3$. We use the method adapted from Chapter 2, as described in more detail in Chapter 3, to fit modified blackbody SEDs to the SCUBA-2-detected sources. To do this, we use the SCUBA-2 positions and fluxes, as well as the *Herschel*-SPIRE imaging. We use a prior on dust temperature to break its degeneracy with redshift, giving us useful constraints on both redshift and far-IR luminosities. Throughout we employ a ΛCDM cosmology with $\Omega_{\Lambda} = 0.728$, $\Omega_{\mathrm{m}} = 0.272$, and $H_0 = 70.4\,\mathrm{km\,s^{-1}\,Mpc^{-1}}$ (Komatsu et al., 2011).

4.2 The Planck candidates follow-up

4.2.1 SCUBA-2 follow-up

51 overdensity fields observed with *Herschel* have been followed-up with SCUBA-2 850 μm observations at the JCMT (project codes: M12AC19, M13AC22, M13BC05, M13BU09, and M14AC02) with approximately 10 arcminute diameter Lissajous scans. The observations were reduced using SMURF (Chapin et al., 2013) called from the ORAC-DR pipeline (Gibb and Jenness, 2010) using the standard blank-field map-making recipe optimised for finding point-sources. Readings from the JCMT water-vapour monitor (WVM, Dempsey and Friberg 2008) and the scaling relations found by Dempsey (Dempsey et al., 2010) were used to correct for atmospheric extinction.

To facilitate finding and extracting of point-sources, we use the standard "matched-filter" provided by ORAC-DR. This procedure subtracts a 30 arcsecond smoothed map from a map convolved with the PSF of the telescope and applying a scaling factor such that point sources return the correct flux density. The purpose of the filter is to remove any large scale structures from the map and facilitate the identification of point like sources. The minimum rms depths of each field range from 1.5 to 3 mJy, with a median of 1.9 mJy for point sources in the matched-filtered images. We extract peak flux densities and positions from these maps to generate a catalogue of 172 SCUBA-2-detected sources with a S/N>4 in 1.20 deg^2 of sky for the 51 *Planck* overdensity fields. We also require a flux density uncertainty of less than 4 mJy for every source since higher noise regions near the edges of the maps are more likely to be artifacts of the map-making procedure. Of the 1.2 deg^2, 0.69 deg^2 was within the *Planck* beam, which we define to be the area in the *Planck* 353 GHz map with flux density greater than half the peak flux density of the *Planck* source, as in Planck Collaboration XXVII (2015). Of the 172 SCUBA-2-detected sources, 138 are located within the *Planck* beam. Table A.2 list the source positions and flux densities, as well as constraints on their far-IR luminosities and redshifts.

In order to assess the number of spurious sources within our catalogue, we perform the same source extraction procedure for negative sources within our maps and find 28 negative peaks satisfying our selection criteria. This is higher than expected given the area observed, possibly caused by map-making/bolometer artifacts. For this process, we avoid negative sources associated with "negative bowls" surrounding bright positive sources caused by the matched-filter. More details pertaining to the possibility of spurious sources are given below. Since the number counts in these regions will differ from those in cosmological fields, and hence it is hard to estimate the effects of confusion(see e.g. Coppin et al., 2006; Scott et al., 2010), we refrain from deboosting the flux densities of our catalogue.

4.2.2 *Herschel* SPIRE data

All our observed fields have accompanying *Herschel*-SPIRE observations at 250, 350 and 500 μm. These observations have been reduced using HIPE 10 (Ott, 2010), with the details given in Planck Collaboration XXVII (2015). The images have instrumental noise levels of 7.7, 6.3 and 7.6 mJy per pixel using the standard pixel sizes of 6, 10 and 14 arcseconds at 250, 350 and 500 μm, respectively. Thus, the noise level in the images are near the confusion limit of *Herschel*-SPIRE (Nguyen et al., 2010).

4.3 SED model and fitting

We use the same modified blackbody SED and fitting method as described in Section 3.2.1, with a few key differences. First, since we do not have a catalogue of nearby sources to use for deblending, we instead use blank sky to estimate the sky covariance matrix. Specifically, we turn to the GOODS-North HerMES field used in MacKenzie et al. (2014), with Gaussian random noise added in quadrature to the instrumental noise, so that the images contain the same noise properties as the overdensity fields. We treat the SCUBA-2-detected sources in the same way as the ALMA resolved LESS sources in Section 3.2.1, using the source positions and flux density estimates at 850 μm (although source positions are not as well constrained, of course). To account for this, we allow source positions to vary, with a 3 arcsecond positional prior, applied to the radial offset, up to a maximum of 10 arcseconds. Such positional errors are typical for 5σ SCUBA-2 850 μm sources (Simpson et al., 2015). In addition to allowing for source position uncertainties, we allow the telescope pointing to vary with a 1.5 arcsecond prior. The former positional prior accounts for source position uncertainty due to instrumental noise and applies to sources individually, while the later accounts for telescope pointing uncertainty and affects all sources within a field the same way. As well as that, a 5% calibration uncertainty is used for the SCUBA-2 flux estimates (Dempsey et al., 2013).

While the ALESS sample had independent photometric redshift estimates (Simpson et al., 2014), our catalogue does not. Instead, we apply a prior on dust temperature in order to generate estimates for both redshifts and far-IR luminosities of our sample. Of course, the adoption of a dust temperature prior means that our redshift estimates would change if we imposed a different prior; however, we make sure to choose a prior distribution with a realistic width, and to the extent that the dust temperature does not change dramatically with redshift, our far-IR luminosity estimates should be good in a relative sense. Using sources above the 4.2 mJy flux limit of LESS for the ALESS follow-up in Chapter 3, we found a dust temperature distribution of 33^{+13}_{-9} K using 68% confidence intervals, and we use this as our dust temperature prior. Note that this represents the distribution and not the error on the mean of the distribution. This central dust temperature and range is consistent with previous estimates for sources selected at 850 μm (e.g. Chapman et al., 2005; Swinbank et al., 2014).

In addition to fitting SEDs to the SCUBA-2-selected sources in the *Planck* overdensity fields, we also apply the same method to SCUBA-2-selected sources from the Cosmology Legacy Survey (CLS, Simpson et al., 2015) within the Ultra Deep Survey (UDS) field (Lawrence et al., 2007). This field also has accompanying *Herschel*-SPIRE observations from HerMES (Oliver et al., 2012). By performing an identical treatment to the sources that are detected in this field, we are able to perform a direct comparison with the *Planck* overdensity fields. In addition to the availability of both SCUBA-2 and *Herschel*-SPIRE observations, this field was chosen since the data are deeper and the area of the sky surveyed is almost identical to that covered by the *Planck* overdensity fields. Before fitting SEDs to these sources, we add Gaussian random noise in quadrature to the instrumental noise of the HerMES SPIRE images to give it the same noise properties as the *Planck* overdensity fields, while accounting for the difference in pixel sizes. This catalogue contains 619 SCUBA-2-detected sources within 1.05 deg^2 of sky, with an average source flux density uncertainty of 1.2 mJy. Similarly, we find 26 negative sources within the UDS field.

4.4 SED fitting results

The results of the SED fitting are shown in Fig. 4.1 and listed in Table A.2 along with 68% percent confidence intervals. Due to the wavelength coverage of the data, we are not able to constrain redshifts for sources with redshifts greater than 6.5, and for those sources we report 84% confidence lower limits. For high redshift sources, these limits are affected by a hard prior that sources cannot have a redshift greater than 10. Using our temperature prior of 33^{+13}_{-9} K, we achieve a photometric redshift uncertainty of $\delta z/(1+z) \approx 0.28$, with 68% confidence intervals skewed to higher redshifts due to the asymmetric prior. In addition to fitting SEDs to the 172 SCUBA-2-detected sources, we fit SEDs to the 28 negative sources in the map above the 4σ cutoff (treating the negative flux densities at $850\,\mu$m as positive). Since there should be no *Herschel* counterparts, the majority of these sources are constrained to the high redshift region of Fig. 4.1, with 19 of the 28 negative sources falling into this category. Of the 172 positive sources in our catalogue, 32 sources have median redshifts greater than 6.5. Thus, the majority of sources with a redshift greater than 6.5 should be considered suspect. Only 9 negative sources coincidentally have *Herschel* counterparts and redshift estimates lower than 6.5, therefore those sources with lower redshifts should be considered reliable ($\sim 6\%$ contamination).

4.5 Discussion

In Fig. 4.1, the majority of well constrained sources have far-IR luminosity estimates of around $10^{13}\mathrm{L}_\odot$, corresponding to SFRs of roughly $1000\,\mathrm{M}_\odot\,\mathrm{yr}^{-1}$. On average, these sources are more luminous than those found by Planck Collaboration XXVII (2015), which have an average of $4\times10^{12}\mathrm{L}_\odot$ (assuming a dust temperature of 35 K), although this is easily explained when considering the selection effects. A representative 2 mJy 1σ detection limit for a 33 K source is plotted in Fig. 4.1 with a solid blue line along with *Herschel*-SPIRE confusion limits for a source of the same dust temperature and dust emissivity. From these detection limits, it is clear that SCUBA-2 is significantly less biased toward low redshift sources than *Herschel*-SPIRE and is more sensitive for sources at redshifts of $\gtrsim$3. While Planck Collaboration XXVII (2015) found that only 3.5% of *Herschel*-SPIRE $350\,\mu$m-detected sources peak in the $500\,\mu$m waveband, we find that 33% of the SCUBA-2-detected sources have SED models with predicted a $500\,\mu$m to $350\,\mu$m flux density ratio greater than 1.

Fig. 4.2 shows the estimated redshift distribution of the SCUBA-2 catalogues within the *Planck* beam for the *Planck* overdensities, with 68% confidence intervals. Also plotted is the expected CLS UDS redshift distribution, given the same survey area and selection function. This plot is generated by bootstrapping the MCMC chains and is corrected for contributions from spurious sources by subtracting the redshift distribution of the negative SCUBA-2 sources. The majority of these sources have redshifts greater than 6 due to the absence of associated *Herschel*-SPIRE detections and their subtraction should correct the estimated redshift distribution for contribution from spurious positive SCUBA-2 detections. In order to give the CLS sources a similar selection function and flux density boosting as the overdensity fields, we add Gaussian random noise to the CLS SCUBA-2 fluxes, such that the distribution of flux density uncertainties matches the distribution of randomly selected points within the *Planck* overdensity fields with a flux density uncertainty < 4 mJy and that are within the *Planck* beam. It is important to note that this estimated redshift distribution is actually a convolution between the true redshift distribution and the redshift error distribution, and because of this, the plotted points are not independent. For the majority of sources in the $z = 1$ - 7 range, this error

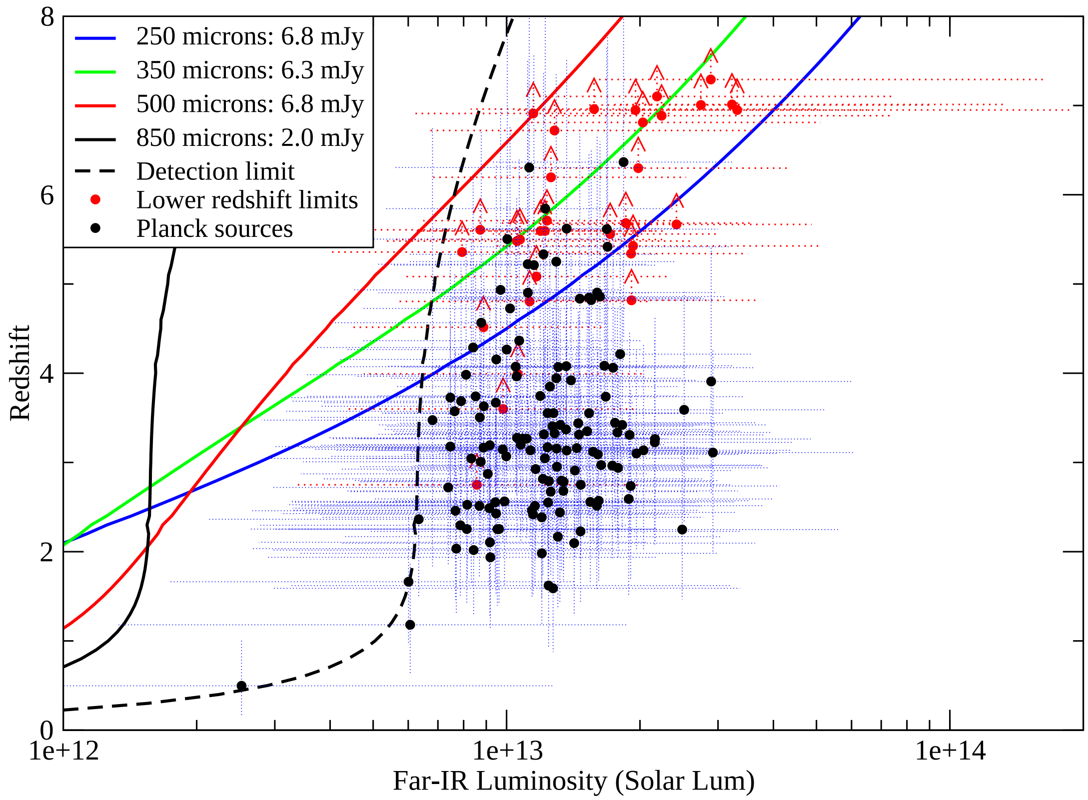

Figure 4.1: Constraints on far-IR luminosities and photometric redshifts for the sample of SCUBA-2-detected sources within the Planck overdensity fields. We report the median values from the MCMC chain points and plot 68% confidence intervals for both far-IR luminosities and photometric redshifts. Photometric redshifts for sources with redshifts less than 1 or greater than 7 are not possible due to the peak of the SED being located outside wavelength coverage; these sources are shown with red points and 84% upper/lower confidence intervals are plotted. Solid lines denote 2.0, 6.8, 6.3, and 5.8 mJy limits at 850, 500, 350, and 250 μm, respectively, for a 33 K dust temperature and 1.5 dust emissivity modified blackbody (the former is a representative 850 μm point source flux density uncertainty and the later are the *Herschel*-SPIRE confusion limits, Nguyen et al., 2010). The black dashed line denotes a representative 4 sigma detection limit for our 850 μm selected sample. Note that our source list is expected to have a rather high number of spurious sources ($\sim$ 28). When fitted, many of these sources get constrained to redshifts greater than 6.5 since the SPIRE images contain no sources in their proximity. For redshifts less than 6.5, we only expect $\sim$ 9 spurious source, based on searching for negative peaks.

distribution function is $\delta z/(1+z) \approx 0.28$. This distribution peaks at a higher redshift than found by Planck Collaboration XXVII (2015) and due to the favourable selection effects of observing at 850 μm, this redshift distribution may more accurately reflect the true redshift distribution of the *Planck* overdensities. If most of the *Planck* overdensities are in fact physically associated structures, those sources found by Planck Collaboration XXVII (2015) would be at higher redshifts and have warmer dust temperatures than assumed. Conversely, we may be detecting colder components of these structures. However, the redshift distribution of the SCUBA-2-selected *Planck* overdensity sources is not significantly different than those within the CLS UDS field, other than a factor of ~ 4 increase in the number of sources. This may suggest that most of these structures are line-of-sight enhancements rather than physically associated.

Using sources within the *Planck* beam and the CLS UDS, we can assess what fraction of the *Planck* 353 GHz flux density we recover at 850 μm with SCUBA-2. To do this, we must first quantify the expected total flux density recovered from the CLS UDS so that we may subtract the expected blank field contribution from the total within the *Planck* beam. Applying the same selection function to the CLS UDS source list as the *Planck* overdensity fields, as described above, we recover a total flux density of 0.39 Jy within the 1.05 deg^2, of the *Planck* beam. From the Cosmic Background Explorer (COBE) satellite, the total flux density of this area should be 46 Jy (although admittedly with a $\sim$30% uncertainty, Fixsen et al., 1998), thus we only recover about 1% of the far-IR background. *Planck* measured an average 850 μm flux density of 470 mJy per field, totalling 23.6 Jy, and with SCUBA-2, we have recovered 1.53 Jy of this flux. Subtracting off the expected blank-field contribution estimated from the CLS UDS field, we conclude that we recover around 5% of the *Planck* flux density within these fields. This means that the 850 μm number counts are enhanced by a larger amount at high flux densities compared to fainter sources. One must also consider that the *Planck* flux densities likely have a significant flux boosting, due to their low signal-to-noise and the large area used to find these overdensities.

We can also try to estimate the contribution of these sources to the cosmic star-formation history. Fig. 4.3 shows the co-moving SFR density for SCUBA-2-detected *Planck* overdensity sources within the *Planck* beam and CLS UDS fields with flux densities greater than 8 mJy (and flux density uncertainty < 2 mJy) assuming a dust temperature prior of 33^{+13}_{-9} K and a conversion factor of $1.08 \times 10^{-10} \mathrm{M_{\odot} yr^{-1} L_{\odot}^{-1}}$ for a Chabrier IMF (Swinbank et al., 2014). We see up to an order of magnitude increase in the *Planck* overdensity fields in comparison with the CLS UDS field, across a broad range of redshifts. Again, this plot is a convolution of the true co-moving SFR density with the redshift error function. This plot is generated by bootstrapping the MCMC chains and is corrected for contributions from spurious sources by subtracting negative SCUBA-2 sources (although with our chosen flux cut, we only have 1 negative source to subtract from the *Planck* overdensity fields and no correction is applied to the CLS UDS field). We add noise to the CLS SCUBA-2 flux densities in order to simulate the *Planck* overdensity selection function, similar to above, but here we match the flux density uncertainty distribution of regions with uncertainty below 2 mJy. With this more strict flux density cut-off, only 0.11 deg^2 and 45 sources of the *Planck* overdensity fields remain. In comparison, an average of 70 CLS UDS sources and the majority of the original survey area are still used. This translates to uncorrected number counts of 409 and 67 sources per square degree brighter than 8 mJy for the *Planck* overdensity and CLS UDS fields, respectively, i.e. the *Planck* fields contain approximately 6 times higher surface density of 850 μm sources than random parts of the sky.

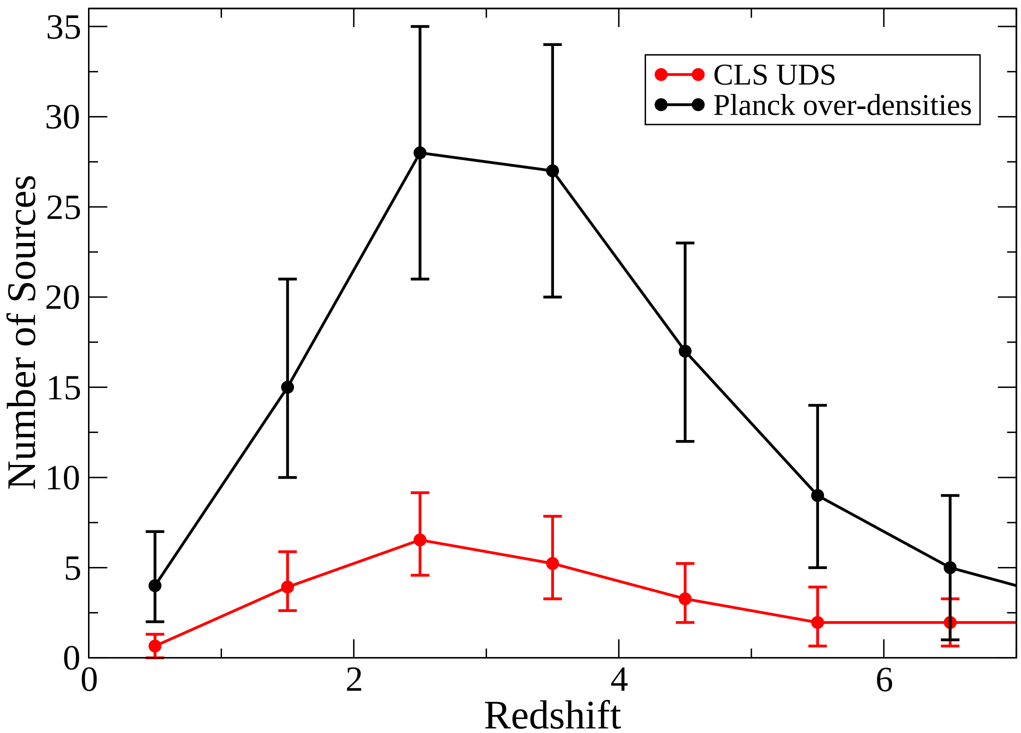

Figure 4.2: Redshift distribution of SCUBA-2-selected sources, assuming a dust temperature prior of 33^{+13}_{-9} K, for the *Planck* overdensity sample within the *Planck* beam. Also plotted is the expected distribution of CLS UDS sources given the same sky coverage and similar selection and flux boosting effects. Error bars are 68% confidence intervals derived from bootstrapping the sample and have been corrected for estimated contributions from spurious sources. The *Planck* overdensity fields contain a factor of about 4 more sources than the CLS UDS field, when given a similar selection function and sky coverage.

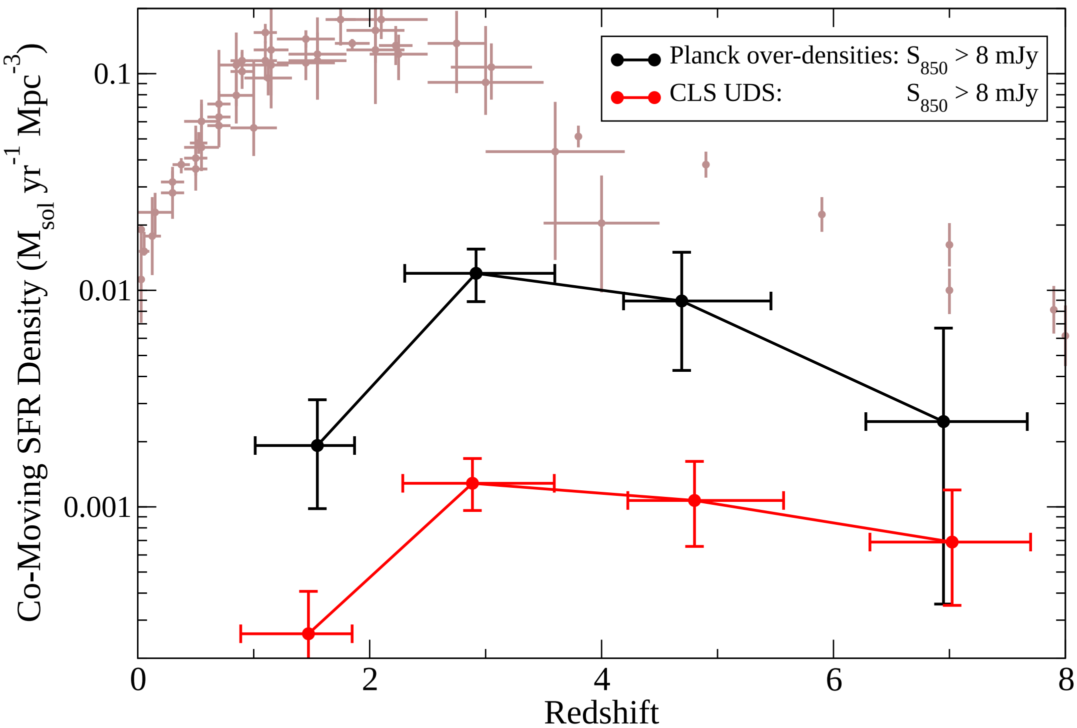

Figure 4.3: Co-moving SFR density vs redshift for SCUBA-2-detected sources with flux densities greater than 8 mJy assuming a dust temperature prior of 33^{+13}_{-9} K. For comparison, we include results from fitting to sources within the CLS UDS field using the same technique, given a similar selection and flux boosing effects. An order of magnitude increase in star formation rate density is seen across all redshifts. The grey points are measurements of the global co-moving star formation density from an assortment of sources, as compiled by Madau and Dickinson (2014). This sample is only expected to have ~ 1 contributing spurious SCUBA-2 source.

4.6 Conclusions

We have followed up 61 *Planck* high-z candidates using SCUBA-2 on the JCMT. Of these, 10 are strong gravitational lenses discussed in Cañameras et al. (2015). The other 51 of the fields are *Planck* overdensities and possible proto-cluster candidates. We have used the same method as in Chapter 3 and the available SCUBA-2 and *Herschel*-SPIRE observations to constrain the redshifts and far-IR luminosity of 172 SCUBA-2-detected sources, assuming a dust temperature prior of 33^{+13}_{-9} K, as found in Chapter 3. A redshift uncertainty of $\delta z/(1+z) \approx 0.28$ is achieved for the majority of sources.

We show that these overdensity fields have a factor of roughly 6 more sources greater than 8 mJy than blank field surveys, peaking between a redshift of 2 and 4. These sources appear to follow approximately the same redshift distribution as those found in blank field surveys. We resolve around 5% of the total *Planck* flux density. Given the same selection function, blank field surveys only recover about 1% of the extragalactic far-IR background, and thus we conclude that the number counts in these fields are more enhanced at high flux densities (>8 mJy) than at lower flux densities. We show that the SFR density in these fields are approximately an order of magnitude higher for sources >8 mJy for redshifts out to $z \sim 6$. Determining if these structures are in fact physically associated will require spectroscopic redshifts at either optical or submm wavelengths. Several such projects and proposals are currently underway.

Chapter 5

Conclusions

5.1 Summary of conclusions

We have developed a new method of deblending SEDs using confused imaging and a forward-modelling technique that preserves important degeneracies that arise when nearby sources are present. To fit the model to the data, we use the inverse of the estimated sky covariance (with or without a catalogue of nearby sources subtracted), where residuals are primarily unresolved faint sources, rather than instrumental noise. We adapted and applied our method to various data sets to show both its flexibility and improvements when compared to traditional methods.

First, in Chapter 2, we discovered several new multiply imaged galaxies behind the massive MS 0451.6−0305 cluster at $z = 0.55$. Using an updated lensing model, we were able to conclude that at least 7 of these multiply imaged galaxies are at a redshift of about 2.9, and possibly constitute an interacting galaxy group. With our new method, we were able to disentangle which of these galaxies were contributing to the "massive submm arc" in the same region of the sky, constraining their dust temperatures, far-IR luminosities, and SFRs. Our method capitalises on the unique fact that the multiple images have unique positions and magnification factors. We also highlight the improbable nature of finding such a lensed interacting galaxy group.

Going forward, the methods developed here give valuable lessons for approaching other strongly lensed submm systems. While several lensed systems appear to be comprised of more than one lensed source (e.g. Cañameras et al., 2015), singly lensed sources can also benefit from our approach. A single galaxy is not a uniform object that looks the same in every waveband, especially so when considering strongly lensed starburst galaxies being found by current large-area submm surveys (Negrello et al., 2010b; Weiß et al., 2013; Cañameras et al., 2015). Such galaxies often have disturbed morphologies and when lensed, different regions of the galaxy are magnified by different amounts. When analysing observations that do not fully resolve the lens, it is critical to employ a forward-modelling approach similar to that which we have developed here. Fu et al. (2012) give a good example of this where they model their source as separate components at multiple wavelengths (optical, submm, and radio), which are then forward-modelled through the lensing potential to recreate the image plane at each wavelength. Using their method, they were able to show that the gas and dust is offset from the stellar mass and that the gas component is significantly more extended than the dust. MS 0451.6−0305 can be seen as a more extreme example of this, where each galaxy in the high-z group has a different SED, and the lens model therefore gives a morphology that varies with wavelength in the image plane. Improving on our method would mean adopting the approach of Fu et al. (2012) for forward modelling sources through the lensing model, as opposed to using point sources at the location of the multiple images, as we have done.

In Chapter 3, we adapted our method for the case of confused point sources and used it to deblend the SEDs of the ALESS sample (Hodge et al., 2013; Swinbank et al., 2014). Through simulations, we were able to show that our method gives realistic estimates of far-IR properties and their uncertainties, and accurately captures the degeneracies among SED parameters of nearby sources, caused by confusion. When compared, our results are similar to those of Swinbank et al. (2014), although significant disagreement is seen when comparing sources individually. Using the sample of Symeonidis et al. (2013) and applying the same selection function as for the ALESS sample, we were able to show that any evolution of the L–$T_{\rm d}$ relation to cooler dust temperatures at high redshifts, are indistinguishable from selection effects.

Implications of this work for the extragalactic submm field are widespread, since confusion limited *Herschel*-SPIRE imaging is currently the highest-impact data available at these wavelengths. Studies of submm populations through large area surveys, such as HerMES (Oliver et al., 2012) and *Herschel*-ATLAS (Eales et al., 2010), are currently being analysed through distorted lens of the two-step SED fitting methods. One current method in use, XID (Roseboom et al., 2010), cannot give independent flux density uncertainty estimates, but relies on assigning flux density uncertainties for populations of sources as a whole. In reality, the flux density uncertainty of an individual source will depend partially on the density of nearby sources. However, XID does make interesting use of a statistic, the AIC (Akaike, 1974), as a tool to determine which sources from their catalogues they use to deblend the *Herschel*-SPIRE images. Such an approach could be used to refine our method. Moving forward, a fraction of the deepest fields within these surveys, such as the Hubble Ultra Deep Field (HUDF), will inevitably be followed-up using ALMA, and thus our methods can be applied directly to the combined data sets.

In Chapter 4, we have followed up 51 *Planck* overdensity fields using SCUBA-2 on the JCMT. We used the same method as in Chapter 3 and the available SCUBA-2 and *Herschel* SPIRE observations to constrain the redshifts and far-IR luminosities of 172 SCUBA-2-detected sources by assuming a dust temperature prior of $33^{+13}_{-9}\,$K, as found in Chapter 3. A redshift uncertainty of $\delta z/(1+z) \approx 0.28$ is achieved for the majority of sources. We show that these so-called "*Planck* overdensity fields" have a factor of roughly 6 more sources brighter than 8 mJy than blank field surveys, with up to an order of magnitude increase in SFR density, which peaks between a redshift of 2 and 4. We resolve around 5% of the total *Planck* flux density into individual SCUBA-2 sources, and when compared to blank field surveys where only about 1% of the extragalactic far-IR background is recovered, we conclude that the number counts in these fields are more enhanced at high flux densities ($> 8\,$mJy) than at lower flux densities.

A comprehensive multi-wavelength follow-up program will be key to unlocking the true nature of the *Planck* overdensities and determining whether they are indeed proto-clusters or simply chance line-of-sight alignments. Such a program is already underway with *Spitzer* IRAC, CFHT MegaCam and WIRCam, and VLT-X-Shooter spectroscopy, for select targets. Once complete, ALMA proposals will follow, and again, joint analysis will benefit from our new methods.

There are two main limiting factors for other researchers to adopt or adapt the methods presented here. One is that each set of data or gravitational lenses are unique, and implementing our methods requires significant more effort than traditional methods. Many would benefit if a generic version were made available, such as was the case for XID (Roseboom et al., 2010), for specific applications. The second limiting factor is computational power. The limiting step here is the *Herschel*-SPIRE likelihood calculation and the need to fit SEDs to all sources in a field simultaneously. We briefly experimented with running our calculations on graphic processing units, but for the specific applications here, we determined that processing power in the form of a computer cluster was more appropriate.

5.2 Future directions

With the large quantities of confusion-limited imaging now available, such as that existing in the *Herschel* archive, several future directions could be pursued to push forward the work we have done here. The first would to be to improve upon the likelihood analysis of the confusion noise. In our current method, we treat confusion noise as Gaussian. In Chapter 2, we saw that if our nearby source catalogue is sufficiently deep, then this assumption would be true; however, a close inspection of Fig. 3.1 shows evidence for faint spurious sources after subtracting all the known sources. In Chapter 2 we used no nearby source catalogue at all, and thus were especially vulnerable to being fooled by any random foreground sources that happen to lie along the "giant submm arc." To improve upon this, instead of the estimated sky covariance used in the likelihood, we could use a multi-wavelength *P(D)* approach (see Patanchon et al., 2009, for the single wavelength case) to estimate likelihoods. *P(D)* is *probability of displacement* for a pixel value in an image, and is what we are approximating when we use the estimated sky covariance. A multi-wavelength *P(D)* analysis would allow us to account for the possibility that we are being mislead by chance alignments of bright sources at the same location on the sky as the source of interest. However, such an analysis will be substantially more computationally intensive.

A second direction that could be taken, is to apply our new method to the ALMA data that will soon be available for the HUDF. With the resolution of ALMA, identification of optical counterparts becomes trivial and confusion noise is no longer an issue. For reasonable integration times, SFRs of only tens of solar masses per year are detectable. The catalogue of sources within this field also has some of the most extensive spectroscopic follow-up available, which can be used to determine redshifts, and those without spectroscopic redshifts, already have reliable photometric estimates based on deep multi-band optical and near-IR imaging. With our method, we could combine the available *Herschel*-SPIRE observations, ALMA observations and available source catalogues, to generate the most accurate SFR history of the Universe to date. In Fig. 3.8, we showed that having ALMA observations at multiple wavelengths can greatly reduce degeneracies with nearby sources in the fit parameters, and thus ambitious proposals to observe at more wavelengths would be extremely worthwhile.

Finally, extending our model SED to shorter as well as longer wavelengths would allow us to include more data to better constrain the properties of the sources. Specifically, extending into the radio would allow us to use existing data from the Very Large Array (VLA) and exploit the submm-radio correlation (e.g. van der Kruit, 1971; Condon et al., 1982; Rickard and Harvey, 1984; Helou et al., 1985, 1988; Ward, 1988). For shorter wavelengths, there is the possibility to move to a two component dust model, to include hot and cold dust components (e.g. Galametz et al., 2012; Izotov et al., 2014), and including polycyclic aromatic hydrocarbon emission would allow even shorter wavelengths to be included (e.g. Allamandola et al., 1985, 1989; Smith et al., 2007; Draine and Li, 2007).

Overall, the study of the history of star-formation in the Universe is becoming an increasingly panchromatic endeavour. The way to fully understand how baryons interact within dark matter halos, forming stars and cycling through the interstellar medium, is to combine data from all available wavebands. Since the same extragalactic fields are targeted by radio, submm, infrared, optical and x-ray facilities, there are already data set that are ripe for truly multi-waveband studies. And as the quality of the data improves, we can expect the biggest questions to be answered not by studying individual objects, but by performing careful statistical analysis for the whole evolving galaxy population. In that context, the sorts of approaches described in this thesis are likely to be increasingly required, and so will need to be built upon and refined.

Through ambitious multi-wavelength statistical surveys, we will be able to build up a complete picture of how light was created in galaxies through cosmic history.

Bibliography

H. Akaike. A New Look at the Statistical Model Identification. *IEEE Transactions on Automatic Control*, 19:716–723, 1974.

L. J. Allamandola, A. G. G. M. Tielens, and J. R. Barker. Polycyclic aromatic hydrocarbons and the unidentified infrared emission bands - Auto exhaust along the Milky Way. ApJ, 290: L25–L28, March 1985. doi: 10.1086/184435.

L. J. Allamandola, A. G. G. M. Tielens, and J. R. Barker. Interstellar polycyclic aromatic hydrocarbons - The infrared emission bands, the excitation/emission mechanism, and the astrophysical implications. ApJS, 71:733–775, December 1989. doi: 10.1086/191396.

A. Amblard et al. Herschel-ATLAS: Dust temperature and redshift distribution of SPIRE and PACS detected sources using submillimetre colours. A&A, 518:L9, July 2010. doi: 10.1051/0004-6361/201014586.

A. J. Barger, L. L. Cowie, and D. B. Sanders. Resolving the Submillimeter Background: The 850 Micron Galaxy Counts. ApJ, 518:L5–L8, June 1999. doi: 10.1086/312054.

J. Barnes. N-body studies of compact groups of galaxies dominated by dark matter. MNRAS, 208:873–885, June 1984.

G. J. Bendo et al. Flux calibration of the Herschel-SPIRE photometer. MNRAS, 433:3062–3078, August 2013. doi: 10.1093/mnras/stt948.

A. Berciano Alba et al. Radio counterpart of the lensed submm emission in the cluster MS0451.6-0305: new evidence for the merger scenario. A&A, 509:A54, January 2010. doi: 10.1051/0004-6361/200912903.

A. W. Blain and M. S. Longair. Submillimetre Cosmology. MNRAS, 264:509, September 1993.

L. E. Bleem, B. Stalder, T. de Haan, et al. Galaxy Clusters Discovered via the Sunyaev-Zel'dovich Effect in the 2500-Square-Degree SPT-SZ Survey. ApJS, 216:27, February 2015. doi: 10.1088/0067-0049/216/2/27.

K. D. Borne, H. Bushouse, R. A. Lucas, and L. Colina. Evidence for Multiple Mergers among Ultraluminous Infrared Galaxies: Remnants of Compact Groups? ApJ, 529:L77–L80, February 2000. doi: 10.1086/312461.

C. Borys, S. Chapman, M. Halpern, and D. Scott. The Hubble Deep Field North SCUBA Super-map - I. Submillimetre maps, sources and number counts. MNRAS, 344:385–398, September 2003. doi: 10.1046/j.1365-8711.2003.06818.x.

C. Borys et al. The nature of a gravitationally lensed submillimetre arc in MS0451.6-0305: two interacting galaxies at z ∼2.9? MNRAS, 352:759–767, August 2004. doi: 10.1111/j.1365-2966.2004.07982.x.

R. J. Bouwens, G. D. Illingworth, P. A. Oesch, et al. UV-continuum Slopes at z ˜ 4-7 from the HUDF09+ERS+CANDELS Observations: Discovery of a Well-defined UV Color-Magnitude Relationship for $z = 4$ Star-forming Galaxies. ApJ, 754:83, August 2012. doi: 10.1088/0004-637X/754/2/83.

F. G. Braglia, D. Pierini, A. Biviano, and H. Böhringer. Multi-wavelength study of X-ray luminous clusters at z ∼ 0.3. I. Star-formation activity of cluster galaxies. A&A, 500:947–963, June 2009. doi: 10.1051/0004-6361/200811589.

F. G. Braglia, P. A. R. Ade, J. J. Bock, et al. Submillimetre observations of galaxy clusters with the BLAST: the star formation activity in Abell 3112. MNRAS, 412:1187–1202, April 2011. doi: 10.1111/j.1365-2966.2010.17973.x.

R. Cañameras, N. P. H. Nesvadba, D. Guery, et al. Planck's dusty GEMS: The brightest gravitationally lensed galaxies discovered with the Planck all-sky survey. A&A, 581:A105, September 2015. doi: 10.1051/0004-6361/201425128.

Capabilities for ALMA Cycle 0. `https://almascience.nrao.edu/documents-and-tools/cycle-0/capabilities/view`.

C. M. Casey. Far-infrared spectral energy distribution fitting for galaxies near and far. MNRAS, 425:3094–3103, October 2012. doi: 10.1111/j.1365-2966.2012.21455.x.

C. M. Casey, S. C. Chapman, R. J. Beswick, et al. Confirming a population of hot-dust dominated, star-forming, ultraluminous galaxies at high redshift. MNRAS, 399:121–128, October 2009. doi: 10.1111/j.1365-2966.2009.15291.x.

A. Cavaliere, S. Colafrancesco, and R. Scaramella. The mass distribution of groups and clusters of galaxies. ApJ, 380:15–23, October 1991. doi: 10.1086/170557.

E. L. Chapin, D. H. Hughes, and I. Aretxaga. The local far-infrared galaxy colour-luminosity distribution: a reference for BLAST and Herschel/SPIRE submillimetre surveys. MNRAS, 393:653–662, February 2009. doi: 10.1111/j.1365-2966.2008.14242.x.

E. L. Chapin, D. S. Berry, A. G. Gibb, et al. SCUBA-2: iterative map-making with the Sub-Millimetre User Reduction Facility. MNRAS, 430:2545–2573, April 2013. doi: 10.1093/mnras/stt052.

E. L. Chapin et al. A joint analysis of BLAST 250-500 μm and LABOCA 870 μm observations in the Extended Chandra Deep Field-South. MNRAS, 411:505–549, February 2011. doi: 10.1111/j.1365-2966.2010.17697.x.

S. C. Chapman, D. Scott, C. Borys, and G. G. Fahlman. Submillimetre sources in rich cluster fields: source counts, redshift estimates and cooling flow limits. MNRAS, 330:92–104, February 2002a. doi: 10.1046/j.1365-8711.2002.05053.x.

S. C. Chapman, I. Smail, R. J. Ivison, G. Helou, D. A. Dale, and G. Lagache. Optically Faint Counterparts to the Infrared Space Observatory FIRBACK 170 Micron Population: Discovery of Cold, Luminous Galaxies at High Redshift. ApJ, 573:66–74, July 2002b. doi: 10.1086/340552.

S. C. Chapman, A. W. Blain, I. Smail, and R. J. Ivison. A Redshift Survey of the Submillimeter Galaxy Population. ApJ, 622:772–796, April 2005. doi: 10.1086/428082.

W. N. Colley, J. A. Tyson, and E. L. Turner. Unlensing Multiple Arcs in 0024+1654: Reconstruction of the Source Image. ApJ, 461:L83, April 1996. doi: 10.1086/310015.

F. Combes et al. A bright z = 5.2 lensed submillimeter galaxy in the field of Abell 773. HLSJ091828.6+514223. A&A, 538:L4, February 2012. doi: 10.1051/0004-6361/201118750.

J. J. Condon, M. A. Condon, G. Gisler, and J. J. Puschell. Strong radio sources in bright spiral galaxies. II - Rapid star formation and galaxy-galaxy interactions. ApJ, 252:102–124, January 1982. doi: 10.1086/159538.

K. Coppin, E. L. Chapin, A. M. J. Mortier, et al. The SCUBA Half-Degree Extragalactic Survey - II. Submillimetre maps, catalogue and number counts. MNRAS, 372:1621–1652, November 2006. doi: 10.1111/j.1365-2966.2006.10961.x.

L. L. Cowie, A. J. Barger, and J.-P. Kneib. Faint Submillimeter Counts from Deep 850 Micron Observations of the Lensing Clusters A370, A851, and A2390. AJ, 123:2197–2205, May 2002. doi: 10.1086/339978.

O. Cucciati, L. Tresse, O. Ilbert, et al. The star formation rate density and dust attenuation evolution over 12 Gyr with the VVDS surveys. A&A, 539:A31, March 2012. doi: 10.1051/0004-6361/201118010.

E. Daddi, M. Dickinson, G. Morrison, et al. Multiwavelength Study of Massive Galaxies at z˜2. I. Star Formation and Galaxy Growth. ApJ, 670:156–172, November 2007. doi: 10.1086/521818.

T. Dahlen, B. Mobasher, M. Dickinson, et al. Evolution of the Luminosity Function, Star Formation Rate, Morphology, and Size of Star-forming Galaxies Selected at Rest-Frame 1500 and 2800 A&A. ApJ, 654:172–185, January 2007. doi: 10.1086/508854.

D. A. Dale et al. Herschel Far-infrared and Submillimeter Photometry for the KINGFISH Sample of nearby Galaxies. ApJ, 745:95, January 2012. doi: 10.1088/0004-637X/745/1/95.

J. T. Dempsey, P. Friberg, T. Jenness, D. Bintley, and W. S. Holland. Extinction correction and on-sky calibration of SCUBA-2. In *Society of Photo-Optical Instrumentation Engineers (SPIE) Conference Series*, volume 7741 of *Society of Photo-Optical Instrumentation Engineers (SPIE) Conference Series*, page 1, July 2010. doi: 10.1117/12.856476.

J. T. Dempsey et al. SCUBA-2: on-sky calibration using submillimetre standard sources. MNRAS, 430:2534–2544, April 2013. doi: 10.1093/mnras/stt090.

J.T. Dempsey and P. Friberg. *SPIE*, 7012:137, 2008. doi: 10.1117/12.787471.

M. Donahue, J. A. Gaskin, S. K. Patel, M. Joy, D. Clowe, and J. P. Hughes. The Mass, Baryonic Fraction, and X-Ray Temperature of the Luminous, High-Redshift Cluster of Galaxies MS 0451.6-0305. ApJ, 598:190–209, November 2003a. doi: 10.1086/378688.

M. Donahue et al. The Mass, Baryonic Fraction, and X-Ray Temperature of the Luminous, High-Redshift Cluster of Galaxies MS 0451.6-0305. ApJ, 598:190–209, November 2003b. doi: 10.1086/378688.

C. D. Dowell, C. A. Allen, R. S. Babu, et al. SHARC II: a Caltech submillimeter observatory facility camera with 384 pixels. In T. G. Phillips and J. Zmuidzinas, editors, *Millimeter and Submillimeter Detectors for Astronomy*, volume 4855 of *Society of Photo-Optical Instrumentation Engineers (SPIE) Conference Series*, pages 73–87, February 2003. doi: 10.1117/12.459360.

B. T. Draine and H. M. Lee. Optical properties of interstellar graphite and silicate grains. ApJ, 285:89–108, October 1984. doi: 10.1086/162480.

B. T. Draine and A. Li. Infrared Emission from Interstellar Dust. IV. The Silicate-Graphite-PAH Model in the Post-Spitzer Era. ApJ, 657:810–837, March 2007. doi: 10.1086/511055.

S. Eales, S. Lilly, W. Gear, et al. The Canada-UK Deep Submillimeter Survey: First Submillimeter Images, the Source Counts, and Resolution of the Background. ApJ, 515:518–524, April 1999. doi: 10.1086/307069.

S. Eales, L. Dunne, D. Clements, et al. The Herschel ATLAS. PASP, 122:499–515, May 2010. doi: 10.1086/653086.

D. Elbaz, M. Dickinson, H. S. Hwang, et al. GOODS-Herschel: an infrared main sequence for star-forming galaxies. A&A, 533:A119, September 2011a. doi: 10.1051/0004-6361/201117239.

D. Elbaz, M. Dickinson, H. S. Hwang, et al. GOODS-Herschel: an infrared main sequence for star-forming galaxies. A&A, 533:A119, September 2011b. doi: 10.1051/0004-6361/201117239.

H. Ezawa, R. Kawabe, K. Kohno, and S. Yamamoto. The Atacama Submillimeter Telescope Experiment (ASTE). In J. M. Oschmann, Jr., editor, *Ground-based Telescopes*, volume 5489 of *Society of Photo-Optical Instrumentation Engineers (SPIE) Conference Series*, pages 763–772, October 2004. doi: 10.1117/12.551391.

E. L. Fitzpatrick. Correcting for the Effects of Interstellar Extinction. PASP, 111:63–75, January 1999. doi: 10.1086/316293.

D. J. Fixsen, E. Dwek, J. C. Mather, C. L. Bennett, and R. A. Shafer. The Spectrum of the Extragalactic Far-Infrared Background from the COBE FIRAS Observations. ApJ, 508:123–128, November 1998. doi: 10.1086/306383.

A. Franceschini, L. Toffolatti, P. Mazzei, L. Danese, and G. de Zotti. Galaxy counts and contributions to the background radiation from 1 micron to 1000 microns. A&AS, 89:285–310, August 1991.

D. T. Frayer, R. J. Ivison, N. Z. Scoville, et al. Molecular Gas in the Z = 2.8 Submillimeter Galaxy SMM 02399-0136. ApJ, 506:L7–L10, October 1998. doi: 10.1086/311639.

H. Fu et al. A Comprehensive View of a Strongly Lensed Planck-Associated Submillimeter Galaxy. ApJ, 753:134, July 2012. doi: 10.1088/0004-637X/753/2/134.

M. Galametz, R. C. Kennicutt, M. Albrecht, et al. Mapping the cold dust temperatures and masses of nearby KINGFISH galaxies with Herschel. MNRAS, 425:763–787, September 2012. doi: 10.1111/j.1365-2966.2012.21667.x.

J. Geach et al. A Panoramic Mid-Infrared Survey of Two Distant Clusters. ApJ, 649:661–672, October 2006. doi: 10.1086/506469.

J. E. Geach, E. L. Chapin, K. E. K. Coppin, et al. The SCUBA-2 Cosmology Legacy Survey: blank-field number counts of 450-μm-selected galaxies and their contribution to the cosmic infrared background. MNRAS, 432:53–61, June 2013. doi: 10.1093/mnras/stt352.

Stuart Geman and Donald Geman. Stochastic relaxation, gibbs distributions and the bayesian restoration of images. *Journal of Applied Statistics*, 20(5-6):25–62, 1993. doi: 10.1080/02664769300000058. URL `http://www.tandfonline.com/doi/abs/10.1080/02664769300000058`.

A.G. Gibb and T. Jenness. *Processing SCUBA-2 Data with ORAC-DR, Starlink User Note 264, Version 1.0.0, http://www.starlink.ac.uk/docs/sun264.htx/sun264.html*. 2010.

I. M. Gioia and G. A. Luppino. The EMSS catalog of X-ray-selected clusters of galaxies. 1: an atlas of CCD images of 41 distant clusters. ApJS, 94:583–614, October 1994. doi: 10.1086/192083.

J. Glenn, J. J. Bock, G. Chattopadhyay, et al. Bolocam: a millimeter-wave bolometric camera. In T. G. Phillips, editor, *Advanced Technology MMW, Radio, and Terahertz Telescopes*, volume 3357 of *Society of Photo-Optical Instrumentation Engineers (SPIE) Conference Series*, pages 326–334, July 1998.

M. J. Griffin, C. E. North, B. Schulz, et al. Flux calibration of broad-band far-infrared and submillimetre photometric instruments: theory and application to Herschel-SPIRE. MNRAS, 434:992–1004, September 2013. doi: 10.1093/mnras/stt999.

M. J. Griffin et al. The Herschel-SPIRE instrument and its in-flight performance. A&A, 518: L3, July 2010. doi: 10.1051/0004-6361/201014519.

C. Gruppioni, F. Pozzi, G. Rodighiero, et al. The Herschel PEP/HerMES luminosity function - I. Probing the evolution of PACS selected Galaxies to z 4. MNRAS, 432:23–52, June 2013. doi: 10.1093/mnras/stt308.

M. Hasselfield, M. Hilton, T. A. Marriage, et al. The Atacama Cosmology Telescope: Sunyaev-Zel'dovich selected galaxy clusters at 148 GHz from three seasons of data. J. Cosmology Astropart. Phys., 7:008, July 2013. doi: 10.1088/1475-7516/2013/07/008.

W. K. Hastings. Monte carlo sampling methods using markov chains and their applications. *Biometrika*, 57(1):97–109, 1970. doi: 10.1093/biomet/57.1.97. URL `http://biomet.oxfordjournals.org/content/57/1/97.abstract`.

G. Helou, B. T. Soifer, and M. Rowan-Robinson. Thermal infrared and nonthermal radio - Remarkable correlation in disks of galaxies. ApJ, 298:L7–L11, November 1985. doi: 10.1086/184556.

G. Helou, I. R. Khan, L. Malek, and L. Boehmer. IRAS observations of galaxies in the Virgo cluster area. ApJS, 68:151–172, October 1988. doi: 10.1086/191285.

Y. D. Hezaveh et al. ALMA Observations of SPT-discovered, Strongly Lensed, Dusty, Star-forming Galaxies. ApJ, 767:132, April 2013. doi: 10.1088/0004-637X/767/2/132.

P. Hickson. Systematic properties of compact groups of galaxies. ApJ, 255:382–391, April 1982. doi: 10.1086/159838.

P. Hickson. Compact Groups of Galaxies. ARA&A, 35:357–388, 1997. doi: 10.1146/annurev.astro.35.1.357.

J. A. Hodge et al. An ALMA Survey of Submillimeter Galaxies in the Extended Chandra Deep Field South: Source Catalog and Multiplicity. ApJ, 768:91, May 2013. doi: 10.1088/0004-637X/768/1/91.

W. S. Holland, E. I. Robson, W. K. Gear, et al. SCUBA: a common-user submillimetre camera operating on the James Clerk Maxwell Telescope. MNRAS, 303:659–672, March 1999. doi: 10.1046/j.1365-8711.1999.02111.x.

W. S. Holland et al. SCUBA-2: the 10 000 pixel bolometer camera on the James Clerk Maxwell Telescope. MNRAS, 430:2513–2533, April 2013. doi: 10.1093/mnras/sts612.

D.H. Hughes, S. Serjeant, J. Dunlop, M. Rowan-Robinson, A. Blain, et al. High - redshift star formation in the Hubble Deep Field revealed by a submillimeter - wavelength survey. *Nature*, 394:241–247, 1998. doi: 10.1038/28328.

R. J. Ivison, I. Smail, J.-F. Le Borgne, et al. A hyperluminous galaxy at z=2.8 found in a deep submillimetre survey. MNRAS, 298:583–593, August 1998. doi: 10.1046/j.1365-8711.1998.01677.x.

R. J. Ivison, I. Smail, P. P. Papadopoulos, et al. Gas, dust and stars in the SCUBA galaxy, SMMJ02399-0136: the EVLA reveals a colossal galactic nursery. MNRAS, 404:198–205, May 2010a. doi: 10.1111/j.1365-2966.2010.16322.x.

R. J. Ivison et al. The far-infrared/radio correlation as probed by Herschel. A&A, 518:L31, July 2010b. doi: 10.1051/0004-6361/201014552.

R. J. Ivison et al. Herschel-ATLAS: A Binary HyLIRG Pinpointing a Cluster of Starbursting Protoellipticals. ApJ, 772:137, August 2013. doi: 10.1088/0004-637X/772/2/137.

Y. I. Izotov, N. G. Guseva, K. J. Fricke, E. Krügel, and C. Henkel. Dust emission in star-forming dwarf galaxies: General properties and the nature of the submm excess. A&A, 570:A97, October 2014. doi: 10.1051/0004-6361/201423539.

E. Jullo and J.-P. Kneib. Multiscale cluster lens mass mapping - I. Strong lensing modelling. MNRAS, 395:1319–1332, May 2009. doi: 10.1111/j.1365-2966.2009.14654.x.

E. Jullo, J.-P. Kneib, M. Limousin, Á. Elíasdóttir, P. J. Marshall, and T. Verdugo. A Bayesian approach to strong lensing modelling of galaxy clusters. *New Journal of Physics*, 9:447, December 2007. doi: 10.1088/1367-2630/9/12/447.

A. Karim et al. An ALMA survey of submillimetre galaxies in the Extended Chandra Deep Field South: high-resolution 870 μm source counts. MNRAS, 432:2–9, June 2013. doi: 10.1093/mnras/stt196.

R. C. Kennicutt, Jr. Star Formation in Galaxies Along the Hubble Sequence. ARA&A, 36:189–232, 1998. doi: 10.1146/annurev.astro.36.1.189.

D. E. Kleinmann and F. J. Low. Observations of Infrared Galaxies. ApJ, 159:L165, March 1970a. doi: 10.1086/180503.

D. E. Kleinmann and F. J. Low. Infrared Observations of Galaxies and of the Extended Nucleus in M82. ApJ, 161:L203, September 1970b. doi: 10.1086/180603.

J.-P. Kneib, R. S. Ellis, I. Smail, W. J. Couch, and R. M. Sharples. Hubble Space Telescope Observations of the Lensing Cluster Abell 2218. ApJ, 471:643, November 1996. doi: 10.1086/177995.

J.-P. Kneib, P. P. van der Werf, K. Kraiberg Knudsen, et al. A multiply imaged, submillimetre-selected ultraluminous infrared galaxy in a galaxy group at $z \sim 2.5$. MNRAS, 349:1211–1217, April 2004. doi: 10.1111/j.1365-2966.2004.07618.x.

C. S. Kochanek and R. Narayan. LensClean - an algorithm for inverting extended, gravitationally lensed images with application to the radio ring lens PKS 1830-211. ApJ, 401:461–473, December 1992. doi: 10.1086/172078.

K. Kodaira, M. Doi, S.-I. Ichikawa, and S. Okamura. An observational study of Shakhbazyan's compact groups of galaxies. II - SCGG 202, 205, 223, 245, and 348. *Publications of the National Astronomical Observatory of Japan*, 1:283–295, 1990.

T. Kodama et al. Panoramic Views of Cluster-Scale Assemblies Explored by Subaru Wide-Field Imaging. PASJ, 57:309–323, April 2005.

E. Komatsu et al. Seven-year Wilkinson Microwave Anisotropy Probe (WMAP) Observations: Cosmological Interpretation. ApJS, 192:18, February 2011. doi: 10.1088/0067-0049/192/2/18.

A. Kovács, S. C. Chapman, C. D. Dowell, et al. SHARC-2 350 μm Observations of Distant Submillimeter-selected Galaxies. ApJ, 650:592–603, October 2006. doi: 10.1086/506341.

E. Kreysa, H.-P. Gemuend, J. Gromke, et al. Bolometer array development at the Max-Planck-Institut fuer Radioastronomie. In T. G. Phillips, editor, *Advanced Technology MMW, Radio, and Terahertz Telescopes*, volume 3357 of *Society of Photo-Optical Instrumentation Engineers (SPIE) Conference Series*, pages 319–325, July 1998.

A. Lawrence, S. J. Warren, O. Almaini, et al. The UKIRT Infrared Deep Sky Survey (UKIDSS). MNRAS, 379:1599–1617, August 2007. doi: 10.1111/j.1365-2966.2007.12040.x.

M. J. Ledlow, I. Smail, F. N. Owen, W. C. Keel, R. J. Ivison, and G. E. Morrison. Gemini Multi-Object Spectrograph Observations of SCUBA Galaxies behind A851. ApJ, 577:L79–L82, October 2002. doi: 10.1086/344334.

M. D. Lehnert and T. M. Heckman. The Nature of Starburst Galaxies. ApJ, 472:546, December 1996. doi: 10.1086/178086.

L. Levenson et al. HerMES: SPIRE Science Demonstration Phase maps. MNRAS, 409:83–91, November 2010. doi: 10.1111/j.1365-2966.2010.17771.x.

A. Lewis and S. Bridle. Cosmological parameters from CMB and other data: A Monte Carlo approach. *Phys. Rev. D*, 66(10):103511, November 2002. doi: 10.1103/PhysRevD.66.103511.

S. J. Lilly, O. Le Fevre, F. Hammer, and D. Crampton. The Canada-France Redshift Survey: The Luminosity Density and Star Formation History of the Universe to Z approximately 1. ApJ, 460:L1, March 1996. doi: 10.1086/309975.

J. Low and D. E. Kleinmann. Proceedings of the Conference on Seyfert Galaxies and Related Objects: 17. Infrared Observations of Seyfert Galaxies, Quasistellar Sources, and Planetary Nebulae. AJ, 73:868, November 1968. doi: 10.1086/110722.

D. Lutz et al. PACS Evolutionary Probe (PEP) - A Herschel key program. A&A, 532:A90, August 2011. doi: 10.1051/0004-6361/201117107.

T. MacKenzie et al. A pilot study for the SCUBA-2 'All-Sky' Survey. MNRAS, page 882, June 2011. doi: 10.1111/j.1365-2966.2011.18840.x.

T. P. MacKenzie et al. Disentangling a group of lensed submm galaxies at z 2.9. MNRAS, 445:201–212, November 2014. doi: 10.1093/mnras/stu1623.

P. Madau and M. Dickinson. Cosmic Star-Formation History. ARA&A, 52:415–486, August 2014. doi: 10.1146/annurev-astro-081811-125615.

P. Madau, H. C. Ferguson, M. E. Dickinson, M. Giavalisco, C. C. Steidel, and A. Fruchter. High-redshift galaxies in the Hubble Deep Field: colour selection and star formation history to z ∼ 4. MNRAS, 283:1388–1404, December 1996.

B. Magnelli, D. Elbaz, R. R. Chary, et al. Evolution of the dusty infrared luminosity function from z = 0 to z = 2.3 using observations from Spitzer. A&A, 528:A35, April 2011. doi: 10.1051/0004-6361/200913941.

B. Magnelli, D. Lutz, P. Santini, et al. A Herschel view of the far-infrared properties of submillimetre galaxies. A&A, 539:A155, March 2012. doi: 10.1051/0004-6361/201118312.

B. Magnelli, P. Popesso, S. Berta, et al. The deepest Herschel-PACS far-infrared survey: number counts and infrared luminosity functions from combined PEP/GOODS-H observations. A&A, 553:A132, May 2013. doi: 10.1051/0004-6361/201321371.

D. Makovoz and F. R. Marleau. Point-Source Extraction with MOPEX. PASP, 117:1113–1128, October 2005. doi: 10.1086/432977.

G. Marsden et al. BLAST: Resolving the Cosmic Submillimeter Background. ApJ, 707:1729–1739, December 2009. doi: 10.1088/0004-637X/707/2/1729.

N. Metropolis, A. W. Rosenbluth, M. N. Rosenbluth, A. H. Teller, and E. Teller. Equation of State Calculations by Fast Computing Machines. J. Chem. Phys., 21:1087–1092, June 1953. doi: 10.1063/1.1699114.

G. R. Meurer, T. M. Heckman, M. D. Lehnert, C. Leitherer, and J. Lowenthal. The Panchromatic Starburst Intensity Limit at Low and High Redshift. AJ, 114:54–68, July 1997. doi: 10.1086/118452.

S. M. Moran et al. A Wide-Field Survey of Two z ˜ 0.5 Galaxy Clusters: Identifying the Physical Processes Responsible for the Observed Transformation of Spirals into S0s. ApJ, 671:1503–1522, December 2007. doi: 10.1086/522303.

T Müller, M Nielbock, Z Balog, U Klaas, and E Vilenius. Pacs photometer-point-source flux calibration. Technical report, 2011.

T. Muller, M. Nielbock, Z. Balog, U. Klass, and E. Vilenius. PACS Photometer - Point-Source Flux Calibration. *Technical Report PICC-ME-TN-037*, April 2011.

E. J. Murphy et al. Calibrating Extinction-free Star Formation Rate Diagnostics with 33 GHz Free-free Emission in NGC 6946. ApJ, 737:67, August 2011. doi: 10.1088/0004-637X/737/2/67.

J. F. Navarro, M. B. Mosconi, and D. Garcia Lambas. Merging instability in groups of galaxies with dark matter. MNRAS, 228:501–511, September 1987.

M. Negrello et al. The Detection of a Population of Submillimeter-Bright, Strongly Lensed Galaxies. *Science*, 330:800–, November 2010a. doi: 10.1126/science.1193420.

M. Negrello et al. The Detection of a Population of Submillimeter-Bright, Strongly Lensed Galaxies. *Science*, 330:800–, November 2010b. doi: 10.1126/science.1193420.

H. T. Nguyen et al. HerMES: The SPIRE confusion limit. A&A, 518:L5, July 2010. doi: 10.1051/0004-6361/201014680.

K. G. Noeske, B. J. Weiner, S. M. Faber, et al. Star Formation in AEGIS Field Galaxies since z=1.1: The Dominance of Gradually Declining Star Formation, and the Main Sequence of Star-forming Galaxies. ApJ, 660:L43–L46, May 2007. doi: 10.1086/517926.

S. J. Oliver et al. The Herschel Multi-tiered Extragalactic Survey: HerMES. MNRAS, 424:1614–1635, August 2012. doi: 10.1111/j.1365-2966.2012.20912.x.

S. Ott. The Herschel Data Processing System – HIPE and Pipelines – Up and Running Since the Start of the Mission. In Y. Mizumoto, K.-I. Morita, and M. Ohishi, editors, *Astronomical Data Analysis Software and Systems XIX*, volume 434 of *Astronomical Society of the Pacific Conference Series*, page 139, December 2010.

E. Pascale, P. A. R. Ade, J. J. Bock, et al. The Balloon-borne Large Aperture Submillimeter Telescope: BLAST. ApJ, 681:400–414, July 2008. doi: 10.1086/588541.

E. Pascale et al. BLAST: A Far-Infrared Measurement of the History of Star Formation. ApJ, 707:1740–1749, December 2009. doi: 10.1088/0004-637X/707/2/1740.

G. Patanchon, P. A. R. Ade, J. J. Bock, et al. Submillimeter Number Counts from Statistical Analysis of BLAST Maps. ApJ, 707:1750–1765, December 2009. doi: 10.1088/0004-637X/707/2/1750.

P. J. E. Peebles and E. Harrison. Principles of Physical Cosmology. *American Journal of Physics*, 62:381–381, April 1994. doi: 10.1119/1.17585.

G. L. Pilbratt, J. R. Riedinger, T. Passvogel, et al. Herschel Space Observatory. An ESA facility for far-infrared and submillimetre astronomy. A&A, 518:L1, July 2010a. doi: 10.1051/0004-6361/201014759.

G. L. Pilbratt et al. Herschel Space Observatory. An ESA facility for far-infrared and submillimetre astronomy. A&A, 518:L1, July 2010b. doi: 10.1051/0004-6361/201014759.

Planck Collaboration VIII. Planck early results. VIII. The all-sky early Sunyaev-Zeldovich cluster sample. A&A, 536:A8, December 2011. doi: 10.1051/0004-6361/201116459.

Planck Collaboration XX. Planck 2013 results. XX. Cosmology from Sunyaev-Zeldovich cluster counts. A&A, 571:A20, November 2014. doi: 10.1051/0004-6361/201321521.

Planck Collaboration XXIX. Planck 2013 results. XXIX. Planck catalogue of Sunyaev-Zeldovich sources. *ArXiv e-prints*, March 2013.

Planck Collaboration XXIX. Planck 2013 results. XXIX. The Planck catalogue of Sunyaev-Zeldovich sources. A&A, 571:A29, November 2014. doi: 10.1051/0004-6361/201321523.

Planck Collaboration XXVII. Planck intermediate results. XXVII. High-redshift infrared galaxy overdensity candidates and lensed sources discovered by Planck and confirmed by Herschel-SPIRE. *ArXiv e-prints*, March 2015.

Planck Collaboration XXVIII. Planck 2013 results. XXVIII. The Planck Catalogue of Compact Sources. A&A, 571:A28, November 2014. doi: 10.1051/0004-6361/201321524.

Planck Collaboration XXXIX. Planck intermediate results. XXXIX. The Planck list of high-redshift source candidates. *ArXiv e-prints*, August 2015.

A. Poglitsch et al. The Photodetector Array Camera and Spectrometer (PACS) on the Herschel Space Observatory. A&A, 518:L2, July 2010. doi: 10.1051/0004-6361/201014535.

A. Pope, D. Scott, M. Dickinson, et al. The Hubble Deep Field-North SCUBA Super-map - IV. Characterizing submillimetre galaxies using deep Spitzer imaging. MNRAS, 370:1185–1207, August 2006. doi: 10.1111/j.1365-2966.2006.10575.x.

W. H. Press and P. Schechter. Formation of Galaxies and Clusters of Galaxies by Self-Similar Gravitational Condensation. ApJ, 187:425–438, February 1974. doi: 10.1086/152650.

N. A. Reddy and C. C. Steidel. A Steep Faint-End Slope of the UV Luminosity Function at z ˜ 2-3: Implications for the Global Stellar Mass Density and Star Formation in Low-Mass Halos. ApJ, 692:778–803, February 2009. doi: 10.1088/0004-637X/692/1/778.

E. D. Reese et al. Sunyaev-Zeldovich Effect-derived Distances to the High-Redshift Clusters MS 0451.6-0305 and CL 0016+16. ApJ, 533:38–49, April 2000. doi: 10.1086/308662.

L. J. Rickard and P. M. Harvey. Far-infrared observations of galactic nuclei. AJ, 89:1520–1530, October 1984. doi: 10.1086/113652.

A. S. G. Robotham and S. P. Driver. The GALEX-SDSS NUV and FUV flux density and local star formation rate. MNRAS, 413:2570–2582, June 2011. doi: 10.1111/j.1365-2966.2011.18327.x.

I. G. Roseboom, S. J. Oliver, M. Kunz, et al. The Herschel Multi-Tiered Extragalactic Survey: source extraction and cross-identifications in confusion-dominated SPIRE images. MNRAS, 409:48–65, November 2010. doi: 10.1111/j.1365-2966.2010.17634.x.

E. E. Salpeter. The Luminosity Function and Stellar Evolution. ApJ, 121:161, January 1955. doi: 10.1086/145971.

D. B. Sanders and I. F. Mirabel. Luminous Infrared Galaxies. ARA&A, 34:749, 1996. doi: 10.1146/annurev.astro.34.1.749.

D. B. Sanders, J. M. Mazzarella, D.-C. Kim, J. A. Surace, and B. T. Soifer. The IRAS Revised Bright Galaxy Sample. AJ, 126:1607–1664, October 2003. doi: 10.1086/376841.

M. A. Schenker, B. E. Robertson, R. S. Ellis, et al. The UV Luminosity Function of Star-forming Galaxies via Dropout Selection at Redshifts z$\sim$7 and 8 from the 2012 Ultra Deep Field Campaign. ApJ, 768:196, May 2013. doi: 10.1088/0004-637X/768/2/196.

P. A. G. Scheuer. A statistical method for analysing observations of faint radio stars. *Proceedings of the Cambridge Philosophical Society*, 53:764–773, 1957. doi: 10.1017/S0305004100032825.

D. Schiminovich, O. Ilbert, S. Arnouts, et al. The GALEX-VVDS Measurement of the Evolution of the Far-Ultraviolet Luminosity Density and the Cosmic Star Formation Rate. ApJ, 619: L47–L50, January 2005. doi: 10.1086/427077.

K. S. Scott, M. S. Yun, G. W. Wilson, et al. Deep 1.1mm-wavelength imaging of the GOODS-S field by AzTEC/ASTE - I. Source catalogue and number counts. MNRAS, 405:2260–2278, July 2010. doi: 10.1111/j.1365-2966.2010.16644.x.

S. E. Scott, M. J. Fox, J. S. Dunlop, et al. The SCUBA 8-mJy survey - I. Submillimetre maps, sources and number counts. MNRAS, 331:817–838, April 2002. doi: 10.1046/j.1365-8711.2002.05193.x.

S. Serjeant. Strong biases in infrared-selected gravitational lenses. MNRAS, 424:2429–2441, August 2012. doi: 10.1111/j.1365-2966.2012.20761.x.

K. Sheth, A. W. Blain, J.-P. Kneib, D. T. Frayer, P. P. van der Werf, and K. K. Knudsen. Detection of CO from SMM J16359+6612, the Multiply Imaged Submillimeter Galaxy behind A2218. ApJ, 614:L5–L8, October 2004. doi: 10.1086/425308.

J. M. Simpson, A. M. Swinbank, I. Smail, et al. An ALMA Survey of Submillimeter Galaxies in the Extended Chandra Deep Field South: The Redshift Distribution and Evolution of Submillimeter Galaxies. ApJ, 788:125, June 2014. doi: 10.1088/0004-637X/788/2/125.

J. M. Simpson, I. Smail, A. M. Swinbank, et al. The SCUBA-2 Cosmology Legacy Survey: ALMA Resolves the Rest-frame Far-infrared Emission of Sub-millimeter Galaxies. ApJ, 799: 81, January 2015. doi: 10.1088/0004-637X/799/1/81.

G. Siringo, E. Kreysa, A. Kovács, et al. The Large APEX BOlometer CAmera LABOCA. A&A, 497:945–962, April 2009. doi: 10.1051/0004-6361/200811454.

P. Sklias et al. Star formation histories, extinction, and dust properties of strongly lensed z$\sim$1.5-3 star-forming galaxies from the Herschel Lensing Survey. A&A, 561:A149, January 2014. doi: 10.1051/0004-6361/201322424.

I. Smail, R. J. Ivison, and A. W. Blain. A Deep Sub-millimeter Survey of Lensing Clusters: A New Window on Galaxy Formation and Evolution. ApJ, 490:L5, November 1997. doi: 10.1086/311017.

I Smail et al. The SCUBA-2 Cosmology Legacy Survey: Ultraluminous Star-forming Galaxies in a z = 1.6 Cluster. ApJ, 782:19, February 2014. doi: 10.1088/0004-637X/782/1/19.

J. D. T. Smith et al. The Mid-Infrared Spectrum of Star-forming Galaxies: Global Properties of Polycyclic Aromatic Hydrocarbon Emission. ApJ, 656:770–791, February 2007. doi: 10.1086/510549.

B. T. Soifer, M. Rowan-Robinson, J. R. Houck, et al. Infrared galaxies in the IRAS minisurvey. ApJ, 278:L71–L74, March 1984. doi: 10.1086/184226.

B. T. Soifer, D. B. Sanders, B. F. Madore, et al. The IRAS bright galaxy sample. II - The sample and luminosity function. ApJ, 320:238–257, September 1987. doi: 10.1086/165536.

C. C. Steidel, K. L. Adelberger, M. Giavalisco, M. Dickinson, and M. Pettini. Lyman-Break Galaxies at $z > 4$ and the Evolution of the Ultraviolet Luminosity Density at High Redshift. ApJ, 519:1–17, July 1999. doi: 10.1086/307363.

M. Stephan. Nebulae (new) discovered and observed at the observatory of Marseilles, 1876 and 1877, M. Stephan. MNRAS, 37:334, April 1877.

R. A. Sunyaev and Y. B. Zeldovich. The interaction of matter and radiation in the hot model of the Universe, II. Ap&SS, 7:20–30, April 1970. doi: 10.1007/BF00653472.

A. M. Swinbank et al. An ALMA survey of sub-millimetre Galaxies in the Extended Chandra Deep Field South: the far-infrared properties of SMGs. MNRAS, 438:1267–1287, February 2014. doi: 10.1093/mnras/stt2273.

B. M. Swinyard et al. In-flight calibration of the Herschel-SPIRE instrument. A&A, 518:L4, July 2010. doi: 10.1051/0004-6361/201014605.

M. Symeonidis et al. The Herschel census of infrared SEDs through cosmic time. MNRAS, 431: 2317–2340, May 2013. doi: 10.1093/mnras/stt330.

L. J. Tacconi et al. Submillimeter Galaxies at $z \sim 2$: Evidence for Major Mergers and Constraints on Lifetimes, IMF, and CO-H_2 Conversion Factor. ApJ, 680:246–262, June 2008. doi: 10.1086/587168.

T. Takata et al. Dusty ERO Search behind Two Massive Clusters. PASJ, 55:789–800, June 2003.

T. T. Takeuchi, K. Yoshikawa, and T. T. Ishii. The Luminosity Function of IRAS Point Source Catalog Redshift Survey Galaxies. ApJ, 587:L89–L92, April 2003. doi: 10.1086/375181.

S. C. Trager, S. M. Faber, A. Dressler, and A. Oemler, Jr. Galaxies at Z 4 and the Formation of Population II. ApJ, 485:92, August 1997. doi: 10.1086/304429.

P. C. van der Kruit. Observations of core sources in Seyfert and normal galaxies with the Westerbork synthesis radio telescope at 1415 MHz. A&A, 15:110–122, November 1971.

M. Verdugo, B. L. Ziegler, and B. Gerken. The galaxy populations from the centers to the infall regions in z 0.25 clusters. A&A, 486:9–24, July 2008. doi: 10.1051/0004-6361:20078735.

T. Vernstrom, D. Scott, J. V. Wall, et al. Deep 3 GHz number counts from a P(D) fluctuation analysis. MNRAS, 440:2791–2809, May 2014. doi: 10.1093/mnras/stu470.

M. P. Viero et al. HerMES: Cosmic Infrared Background Anisotropies and the Clustering of Dusty Star-forming Galaxies. ApJ, 772:77, July 2013. doi: 10.1088/0004-637X/772/1/77.

Wei-Hao Wang, Lennox L. Cowie, Amy J. Barger, and Jonathan P. Williams. Sma observations of goods 85011 and goods 85013: First examples of multiple submillimeter sources resolved by an interferometer. *The Astrophysical Journal Letters*, 726(2):L18, 2011. URL `http://stacks.iop.org/2041-8205/726/i=2/a=L18`.

M. J. Ward. X-ray emission from starburst nuclei. MNRAS, 231:1P–5P, March 1988.

J. L. Wardlow et al. An AzTEC 1.1-mm survey for ULIRGs in the field of the Galaxy Cluster MS0451.6-0305. MNRAS, 401:2299–2317, February 2010. doi: 10.1111/j.1365-2966.2009.15847.x.

J. L. Wardlow et al. HerMES: Candidate Gravitationally Lensed Galaxies and Lensing Statistics at Submillimeter Wavelengths. ApJ, 762:59, January 2013. doi: 10.1088/0004-637X/762/1/59.

A. Weiß, C. De Breuck, D. P. Marrone, et al. ALMA Redshifts of Millimeter-selected Galaxies from the SPT Survey: The Redshift Distribution of Dusty Star-forming Galaxies. ApJ, 767:88, April 2013. doi: 10.1088/0004-637X/767/1/88.

A. Weiß et al. The Large Apex Bolometer Camera Survey of the Extended Chandra Deep Field South. ApJ, 707:1201–1216, December 2009. doi: 10.1088/0004-637X/707/2/1201.

A. E. Whitford. The law of interstellar reddening. AJ, 63:201–207, May 1958. doi: 10.1086/107725.

T. K. Wyder, M. A. Treyer, B. Milliard, et al. The Ultraviolet Galaxy Luminosity Function in the Local Universe from GALEX Data. ApJ, 619:L15–L18, January 2005. doi: 10.1086/424735.

Y. B. Zeldovich and R. A. Sunyaev. The Interaction of Matter and Radiation in a Hot-Model Universe. Ap&SS, 4:301–316, July 1969. doi: 10.1007/BF00661821.

A. Zitrin, T. Broadhurst, R. Barkana, Y. Rephaeli, and N. Benítez. Strong-lensing analysis of a complete sample of 12 MACS clusters at z 0.5: mass models and Einstein radii. MNRAS, 410:1939–1956, January 2011. doi: 10.1111/j.1365-2966.2010.17574.x.

Appendix

Appendix A

Source lists and far-IR property tables

A.1 Far-IR properties of the ALESS sample

Table A.1: The model fit parameters and credible intervals for the ALESS sample. The ALMA flux density estimates are those of Hodge et al. (2013) and the photometeric redshift estimates are those of Simpson et al. (2014). We report the median values from our MCMC chains for the far-IR luminosities and dust temperatures. We report 68% credible intervals for both dust temperatures and far-IR luminosities. In the case where the lower credible interval is either zero for the far-IR luminosity or 10 K for the dust temperature, we report the 84% upper credible interval as an upper limit.

Gal ID	ALMA 870 μm (mJy)	$z_{\rm phot}$	Far-IR Luminosity ($L_\odot$)	Dust Temp. (K)
ALESS001.1	6.75 ± 0.49	$4.34^{+2.66}_{-1.43}$	$9.0^{+5.6}_{-8.1} \times 10^{12}$	37^{+12}_{-14}
ALESS001.2	3.48 ± 0.43	$4.65^{+2.34}_{-1.02}$	$8.1^{+4.0}_{-6.8} \times 10^{12}$	46^{+14}_{-14}
ALESS001.3	1.89 ± 0.42	$2.85^{+0.20}_{-0.30}$	$1.2^{+0.5}_{-0.6} \times 10^{12}$	29^{+4}_{-3}
ALESS002.1	3.81 ± 0.42	$1.96^{+0.27}_{-0.20}$	$2.1^{+0.8}_{-2.0} \times 10^{12}$	30^{+7}_{-11}
ALESS002.2	4.23 ± 0.67	$3.92^{+0.48}_{-1.42}$	$2.1^{+2.3}_{-2.0} \times 10^{12}$	< 39
ALESS003.1	8.28 ± 0.40	$3.90^{+0.50}_{-0.59}$	$1.1^{+0.3}_{-0.4} \times 10^{13}$	38^{+5}_{-4}
ALESS005.1	7.78 ± 0.68	$2.86^{+0.05}_{-0.04}$	$5.3^{+0.6}_{-0.6} \times 10^{12}$	30^{+1}_{-1}
ALESS006.1	5.98 ± 0.41	$0.45^{+0.06}_{-0.04}$	$4.3^{+1.1}_{-1.6} \times 10^{10}$	11^{+1}_{-1}
ALESS007.1	6.10 ± 0.32	$2.50^{+0.12}_{-0.16}$	$8.8^{+1.1}_{-1.1} \times 10^{12}$	34^{+1}_{-1}
ALESS009.1	8.75 ± 0.47	$4.50^{+0.54}_{-2.33}$	$< 1.8 \times 10^{13}$	36^{+13}_{-10}
ALESS010.1	5.25 ± 0.50	$2.02^{+0.09}_{-0.09}$	$3.6^{+0.2}_{-0.2} \times 10^{12}$	31^{+1}_{-1}
ALESS011.1	7.29 ± 0.41	$2.83^{+1.88}_{-0.50}$	$1.6^{+0.8}_{-1.3} \times 10^{13}$	43^{+8}_{-15}
ALESS013.1	8.01 ± 0.59	$3.25^{+0.64}_{-0.46}$	$5.2^{+1.6}_{-2.1} \times 10^{12}$	30^{+3}_{-4}
ALESS014.1	7.47 ± 0.52	$4.47^{+2.54}_{-0.88}$	$3.5^{+1.6}_{-2.4} \times 10^{13}$	54^{+11}_{-15}
ALESS015.1	9.01 ± 0.37	$1.93^{+0.62}_{-0.33}$	$3.1^{+1.3}_{-1.9} \times 10^{12}$	25^{+4}_{-4}
ALESS015.3	1.95 ± 0.52	$3.15^{+0.65}_{-0.65}$	$7.8^{+3.6}_{-5.6} \times 10^{11}$	26^{+8}_{-7}
ALESS017.1	8.44 ± 0.46	$1.51^{+0.10}_{-0.07}$	$2.2^{+0.2}_{-0.3} \times 10^{12}$	24^{+1}_{-1}
ALESS018.1	4.38 ± 0.54	$2.04^{+0.10}_{-0.06}$	$4.3^{+1.2}_{-1.0} \times 10^{12}$	35^{+3}_{-2}
ALESS019.1	4.98 ± 0.42	$2.41^{+0.17}_{-0.11}$	$3.7^{+0.5}_{-0.5} \times 10^{12}$	32^{+1}_{-1}
ALESS019.2	1.98 ± 0.47	$2.17^{+0.09}_{-0.10}$	$1.4^{+0.3}_{-0.3} \times 10^{12}$	29^{+2}_{-2}
ALESS022.1	4.48 ± 0.54	$1.88^{+0.18}_{-0.23}$	$3.4^{+0.8}_{-0.9} \times 10^{12}$	30^{+2}_{-2}
ALESS023.1	6.74 ± 0.37	$4.99^{+2.01}_{-2.55}$	$< 2.7 \times 10^{13}$	50^{+17}_{-19}
ALESS023.7	1.76 ± 0.49	$2.90^{+1.20}_{-0.40}$	$1.4^{+0.8}_{-1.3} \times 10^{12}$	33^{+13}_{-11}
ALESS025.1	6.21 ± 0.47	$2.24^{+0.07}_{-0.17}$	$5.4^{+0.7}_{-0.6} \times 10^{12}$	33^{+1}_{-1}
ALESS029.1	5.90 ± 0.43	$2.66^{+2.94}_{-0.76}$	$< 2.2 \times 10^{13}$	44^{+14}_{-20}
ALESS031.1	8.12 ± 0.37	$2.89^{+1.80}_{-0.41}$	$1.1^{+0.6}_{-0.8} \times 10^{13}$	40^{+8}_{-12}

Gal ID	ALMA 870 μm (mJy)	$z_{\rm phot}$	Far-IR Luminosity ($L_\odot$)	Dust Temp. (K)
ALESS037.1	2.92 ± 0.41	$3.53^{+0.56}_{-0.31}$	$6.7^{+1.9}_{-2.5} \times 10^{12}$	44^{+5}_{-5}
ALESS037.2	1.65 ± 0.44	$4.87^{+0.21}_{-0.40}$	$1.2^{+0.4}_{-0.4} \times 10^{13}$	64^{+6}_{-6}
ALESS039.1	4.33 ± 0.34	$2.44^{+0.17}_{-0.23}$	$2.9^{+0.6}_{-0.6} \times 10^{12}$	30^{+2}_{-2}
ALESS041.1	4.88 ± 0.61	$2.75^{+4.25}_{-0.72}$	$< 4.6 \times 10^{13}$	62^{+18}_{-28}
ALESS041.3	2.68 ± 0.75	$3.10^{+1.30}_{-0.60}$	$1.5^{+0.7}_{-1.1} \times 10^{12}$	28^{+9}_{-8}
ALESS043.1	2.30 ± 0.42	$1.71^{+0.20}_{-0.12}$	$1.0^{+0.2}_{-0.3} \times 10^{12}$	28^{+2}_{-2}
ALESS045.1	6.03 ± 0.54	$2.34^{+0.26}_{-0.67}$	$3.0^{+1.5}_{-1.5} \times 10^{12}$	28^{+4}_{-4}
ALESS049.1	6.00 ± 0.68	$2.76^{+0.11}_{-0.14}$	$7.2^{+0.9}_{-1.0} \times 10^{12}$	37^{+2}_{-2}
ALESS049.2	1.80 ± 0.46	$1.47^{+0.07}_{-0.10}$	$1.3^{+0.2}_{-0.3} \times 10^{12}$	31^{+2}_{-2}
ALESS051.1	4.70 ± 0.39	$1.22^{+0.03}_{-0.06}$	$5.5^{+0.8}_{-0.8} \times 10^{11}$	20^{+1}_{-1}
ALESS055.1	3.99 ± 0.36	$2.05^{+0.15}_{-0.13}$	$3.1^{+1.6}_{-1.5} \times 10^{11}$	< 18
ALESS055.2	2.35 ± 0.60	$4.20^{+0.50}_{-0.90}$	$7.3^{+3.0}_{-4.2} \times 10^{11}$	< 21
ALESS055.5	1.37 ± 0.37	$2.35^{+0.11}_{-0.13}$	$4.4^{+1.7}_{-3.9} \times 10^{11}$	26^{+7}_{-7}
ALESS057.1	3.56 ± 0.61	$2.95^{+0.05}_{-0.10}$	$5.9^{+0.6}_{-0.7} \times 10^{12}$	40^{+2}_{-2}
ALESS059.2	1.94 ± 0.44	$2.09^{+0.78}_{-0.29}$	$1.2^{+0.6}_{-0.8} \times 10^{12}$	31^{+6}_{-6}
ALESS061.1	4.29 ± 0.51	$6.52^{+0.36}_{-0.34}$	$2.2^{+0.3}_{-0.3} \times 10^{13}$	60^{+3}_{-3}
ALESS063.1	5.59 ± 0.35	$1.87^{+0.10}_{-0.33}$	$1.1^{+0.3}_{-0.3} \times 10^{12}$	22^{+2}_{-2}
ALESS065.1	4.16 ± 0.43	$2.82^{+0.95}_{-0.36}$	$5.0^{+1.8}_{-2.6} \times 10^{12}$	35^{+5}_{-6}
ALESS066.1	2.50 ± 0.48	$2.33^{+0.05}_{-0.04}$	$6.0^{+0.4}_{-0.4} \times 10^{12}$	42^{+1}_{-1}
ALESS067.1	4.50 ± 0.38	$2.14^{+0.05}_{-0.09}$	$1.1^{+0.6}_{-0.9} \times 10^{12}$	23^{+4}_{-13}
ALESS067.2	1.73 ± 0.41	$2.05^{+0.06}_{-0.16}$	$3.3^{+1.8}_{-2.7} \times 10^{11}$	22^{+7}_{-7}
ALESS068.1	3.70 ± 0.56	$3.60^{+1.10}_{-1.10}$	$5.8^{+1.0}_{-1.0} \times 10^{12}$	42^{+2}_{-2}
ALESS069.1	4.85 ± 0.63	$2.34^{+0.27}_{-0.44}$	$2.3^{+0.8}_{-0.8} \times 10^{12}$	29^{+3}_{-3}
ALESS069.2	2.36 ± 0.56	$4.75^{+0.35}_{-1.05}$	$9.4^{+3.4}_{-5.2} \times 10^{11}$	< 19
ALESS069.3	2.05 ± 0.56	$4.80^{+0.30}_{-1.10}$	$8.7^{+3.7}_{-5.5} \times 10^{11}$	< 23
ALESS070.1	5.23 ± 0.45	$2.28^{+0.05}_{-0.06}$	$7.6^{+0.5}_{-0.5} \times 10^{12}$	36^{+1}_{-1}
ALESS071.1	2.85 ± 0.60	$2.48^{+0.21}_{-0.11}$	$1.7^{+0.2}_{-0.3} \times 10^{13}$	49^{+2}_{-2}
ALESS071.3	1.36 ± 0.38	$2.73^{+0.22}_{-0.25}$	$1.1^{+0.5}_{-0.5} \times 10^{12}$	35^{+4}_{-5}
ALESS072.1	4.91 ± 0.50	$4.15^{+0.55}_{-1.65}$	$5.4^{+2.5}_{-4.9} \times 10^{12}$	37^{+10}_{-8}
ALESS073.1	6.09 ± 0.47	$5.18^{+0.43}_{-0.45}$	$7.6^{+1.6}_{-1.7} \times 10^{12}$	38^{+4}_{-3}
ALESS074.1	4.64 ± 0.69	$1.80^{+0.13}_{-0.13}$	$2.4^{+0.2}_{-0.2} \times 10^{12}$	30^{+1}_{-1}
ALESS075.1	3.17 ± 0.45	$2.39^{+0.08}_{-0.06}$	$5.8^{+0.4}_{-0.5} \times 10^{12}$	36^{+1}_{-1}
ALESS075.4	1.30 ± 0.37	$2.10^{+0.29}_{-0.34}$	$5.7^{+1.9}_{-2.4} \times 10^{11}$	23^{+3}_{-3}
ALESS076.1	6.42 ± 0.58	$4.50^{+0.20}_{-2.00}$	$< 6.1 \times 10^{12}$	33^{+10}_{-7}
ALESS079.1	4.12 ± 0.37	$2.04^{+0.63}_{-0.31}$	$2.1^{+1.0}_{-1.3} \times 10^{12}$	29^{+5}_{-5}
ALESS079.2	1.98 ± 0.40	$1.55^{+0.11}_{-0.18}$	$1.5^{+0.6}_{-0.6} \times 10^{12}$	33^{+4}_{-4}
ALESS079.4	1.81 ± 0.51	$4.60^{+1.20}_{-0.60}$	$1.2^{+0.6}_{-0.9} \times 10^{12}$	< 31
ALESS080.1	4.03 ± 0.86	$1.96^{+0.16}_{-0.14}$	$1.1^{+0.3}_{-0.4} \times 10^{12}$	23^{+2}_{-2}
ALESS080.2	3.54 ± 0.90	$1.37^{+0.17}_{-0.08}$	$4.6^{+1.6}_{-1.8} \times 10^{11}$	19^{+2}_{-2}
ALESS082.1	1.93 ± 0.47	$2.10^{+3.27}_{-0.44}$	$8.0^{+6.1}_{-7.7} \times 10^{12}$	56^{+16}_{-26}
ALESS084.1	3.17 ± 0.63	$1.92^{+0.09}_{-0.07}$	$1.6^{+0.7}_{-1.4} \times 10^{12}$	28^{+9}_{-6}
ALESS084.2	3.25 ± 0.77	$1.75^{+0.08}_{-0.19}$	$1.0^{+0.3}_{-0.3} \times 10^{12}$	26^{+3}_{-3}
ALESS087.1	1.34 ± 0.35	$3.20^{+0.08}_{-0.47}$	$1.0^{+0.2}_{-0.2} \times 10^{13}$	58^{+5}_{-5}
ALESS087.3	2.44 ± 0.59	$4.00^{+1.10}_{-0.30}$	$2.5^{+0.9}_{-1.3} \times 10^{12}$	33^{+6}_{-6}
ALESS088.1	4.62 ± 0.58	$1.84^{+0.12}_{-0.11}$	$1.1^{+0.5}_{-0.5} \times 10^{12}$	22^{+4}_{-3}

Gal ID	ALMA 870 μm (mJy)	z_{phot}	Far-IR Luminosity ($L_{\odot}$)	Dust Temp. (K)
ALESS088.2	2.14 ± 0.50	$5.20^{+0.60}_{-1.20}$	$1.5^{+0.7}_{-1.0} \times 10^{12}$	< 32
ALESS088.5	2.86 ± 0.72	$2.30^{+0.11}_{-0.50}$	$3.7^{+1.2}_{-1.1} \times 10^{12}$	37^{+5}_{-3}
ALESS088.11	2.51 ± 0.71	$2.57^{+0.04}_{-0.12}$	$7.2^{+4.0}_{-6.0} \times 10^{11}$	24^{+8}_{-8}
ALESS092.2	2.42 ± 0.68	$1.90^{+0.28}_{-0.75}$	$1.3^{+0.6}_{-1.0} \times 10^{11}$	< 17
ALESS094.1	3.18 ± 0.52	$2.87^{+0.37}_{-0.64}$	$3.5^{+1.3}_{-1.5} \times 10^{12}$	35^{+5}_{-4}
ALESS098.1	4.78 ± 0.60	$1.63^{+0.17}_{-0.09}$	$7.2^{+1.1}_{-1.5} \times 10^{12}$	33^{+1}_{-2}
ALESS099.1	2.05 ± 0.43	$5.00^{+1.20}_{-0.60}$	$1.5^{+0.6}_{-0.9} \times 10^{12}$	< 25
ALESS102.1	3.08 ± 0.50	$1.76^{+0.16}_{-0.18}$	$1.3^{+0.3}_{-0.3} \times 10^{12}$	26^{+2}_{-1}
ALESS103.3	1.43 ± 0.41	$4.40^{+0.70}_{-0.70}$	$1.5^{+1.0}_{-1.3} \times 10^{12}$	38^{+11}_{-22}
ALESS107.1	1.91 ± 0.39	$3.75^{+0.09}_{-0.08}$	$4.9^{+2.1}_{-1.8} \times 10^{12}$	47^{+7}_{-5}
ALESS107.3	1.46 ± 0.40	$2.12^{+1.54}_{-0.81}$	$< 17.6 \times 10^{11}$	31^{+11}_{-16}
ALESS110.1	4.11 ± 0.47	$2.55^{+0.70}_{-0.50}$	$5.5^{+2.2}_{-3.2} \times 10^{12}$	41^{+6}_{-7}
ALESS110.5	2.39 ± 0.60	$3.70^{+0.40}_{-1.20}$	$4.4^{+1.6}_{-2.6} \times 10^{11}$	< 16
ALESS112.1	7.62 ± 0.49	$1.95^{+0.15}_{-0.26}$	$2.8^{+0.7}_{-0.7} \times 10^{12}$	27^{+2}_{-2}
ALESS114.1	2.99 ± 0.78	$3.00^{+1.40}_{-0.50}$	$1.1^{+0.5}_{-0.8} \times 10^{13}$	46^{+8}_{-12}
ALESS114.2	1.98 ± 0.50	$1.56^{+0.07}_{-0.07}$	$4.2^{+0.3}_{-0.3} \times 10^{12}$	36^{+1}_{-1}
ALESS116.1	3.08 ± 0.47	$3.54^{+1.47}_{-0.87}$	$3.3^{+2.0}_{-3.0} \times 10^{12}$	36^{+13}_{-14}
ALESS116.2	3.42 ± 0.57	$4.02^{+1.19}_{-2.19}$	$< 8.5 \times 10^{12}$	40^{+16}_{-14}
ALESS118.1	3.20 ± 0.54	$2.26^{+0.50}_{-0.23}$	$2.5^{+0.9}_{-1.2} \times 10^{12}$	33^{+5}_{-5}
ALESS119.1	8.27 ± 0.54	$3.50^{+0.95}_{-0.35}$	$1.1^{+0.3}_{-0.5} \times 10^{13}$	39^{+5}_{-6}
ALESS122.1	3.69 ± 0.42	$2.06^{+0.05}_{-0.06}$	$8.5^{+0.6}_{-0.6} \times 10^{12}$	38^{+1}_{-1}
ALESS124.1	3.64 ± 0.57	$6.07^{+0.94}_{-1.16}$	$5.3^{+3.0}_{-4.0} \times 10^{12}$	< 47
ALESS124.4	2.24 ± 0.58	$5.60^{+0.60}_{-1.20}$	$5.2^{+2.2}_{-3.1} \times 10^{12}$	45^{+9}_{-9}
ALESS126.1	2.23 ± 0.55	$1.82^{+0.28}_{-0.08}$	$8.4^{+1.9}_{-2.3} \times 10^{11}$	30^{+3}_{-3}

A.2 Redshift and far-IR estimates for SCUBA-2 selected sources within the *Planck* overdensity fields

Table A.2: SCUBA-2 detected sources within the Planck proto-cluster candidate fields. We report the median values from the MCMC chain points and plot 68% confidence intervals for both far-IR luminosities and photometric redshifts. Photometric redshifts for sources with redshifts less than 1 or greater than 7 are not possible, due to the peak of the SED being located outside the wavelength coverage. These sources are shown with red points and 84% upper/lower confidence intervals.

Gal ID	RA J2000	Dec J2000	S_{850} (mJy)	z_{phot}	Far-IR Luminosity ($L_{\odot}$)	In Planck Beam
PLCK_DU_G045.7-41.2-0	21:39:51.055	-8:47:16.80	13.1 ± 2.5	$4.1^{+1.6}_{-1.3}$	$1.7^{+1.9}_{-1.1} \times 10^{13}$	Y
PLCK_DU_G045.7-41.2-1	21:39:30.820	-8:44:08.79	11.1 ± 2.4	$2.7^{+1.0}_{-0.9}$	$1.3^{+1.5}_{-0.8} \times 10^{13}$	Y
PLCK_DU_G045.7-41.2-2	21:39:47.817	-8:44:20.80	9.9 ± 2.1	$0.1^{+0.1}_{-0.0}$	$9.7^{+46.4}_{-8.4} \times 10^{10}$	Y
PLCK_DU_G045.7-41.2-3	21:39:29.200	-8:46:04.78	13.1 ± 3.2	$3.9^{+1.4}_{-1.2}$	$1.4^{+1.3}_{-0.8} \times 10^{13}$	N
PLCK_DU_G059.1-67.1-0	23:26:25.977	-15:28:05.40	14.5 ± 1.6	$3.3^{+1.3}_{-1.1}$	$1.5^{+1.6}_{-0.9} \times 10^{13}$	Y
PLCK_DU_G059.1-67.1-1	23:26:01.346	-15:30:45.32	18.1 ± 3.8	> 7.0	$2.7^{+6.3}_{-1.2} \times 10^{13}$	N
PLCK_DU_G059.1-67.1-2	23:26:41.749	-15:28:57.36	13.3 ± 2.8	$3.3^{+1.2}_{-1.0}$	$1.2^{+1.2}_{-0.7} \times 10^{13}$	N
PLCK_DU_G059.1-67.1-3	23:26:47.004	-15:27:17.34	14.8 ± 3.5	> 7.1	$2.2^{+5.2}_{-1.0} \times 10^{13}$	N
PLCK_DU_G073.4-57.5-0	23:14:42.344	-4:16:40.20	10.4 ± 1.8	$2.6^{+1.0}_{-0.9}$	$9.4^{+11.0}_{-6.1} \times 10^{12}$	Y

Gal ID	RA J2000	Dec J2000	S_{850} (mJy)	$z_{\rm phot}$	Far-IR Luminosity ($L_\odot$)	In Planck Beam
PLCK_DU_G073.4-57.5-1	23:14:42.611	-4:20:00.20	13.6 ± 2.5	$4.8^{+1.7}_{-1.4}$	$1.6^{+1.4}_{-0.8} \times 10^{13}$	N
PLCK_DU_G073.4-57.5-2	23:14:41.809	-4:17:44.20	8.3 ± 2.0	> 3.6	$9.8^{+9.9}_{-5.5} \times 10^{12}$	Y
PLCK_DU_G073.4-57.5-3	23:14:34.589	-4:17:00.20	7.2 ± 1.8	$3.7^{+1.5}_{-1.2}$	$7.9^{+8.2}_{-4.6} \times 10^{12}$	Y
PLCK_G006.1+61.8-0	14:33:47.184	12:12:60.00	16.0 ± 2.8	$2.8^{+1.1}_{-1.0}$	$1.3^{+1.6}_{-0.9} \times 10^{13}$	Y
PLCK_G006.1+61.8-1	14:33:39.817	12:14:52.00	14.0 ± 3.0	$3.7^{+1.4}_{-1.1}$	$1.7^{+1.8}_{-1.0} \times 10^{13}$	Y
PLCK_G009.8+72.6-0	13:59:19.151	19:19:15.97	18.7 ± 2.2	$3.2^{+1.2}_{-1.1}$	$2.2^{+2.3}_{-1.4} \times 10^{13}$	Y
PLCK_G009.8+72.6-1	13:59:02.479	19:19:32.00	10.1 ± 2.2	$5.3^{+2.0}_{-1.6}$	$1.2^{+1.0}_{-0.6} \times 10^{13}$	Y
PLCK_G009.8+72.6-2	13:59:28.188	19:16:27.92	11.9 ± 2.9	$3.9^{+1.4}_{-1.2}$	$1.3^{+1.2}_{-0.7} \times 10^{13}$	N
PLCK_G009.8+72.6-3	13:58:57.958	19:18:15.99	11.1 ± 2.7	$5.8^{+3.0}_{-2.8}$	$1.2^{+1.1}_{-0.7} \times 10^{13}$	Y
PLCK_G056.7+62.6-0	14:54:39.298	34:43:28.00	15.9 ± 2.7	$2.9^{+1.2}_{-1.0}$	$1.8^{+2.1}_{-1.2} \times 10^{13}$	Y
PLCK_G056.7+62.6-1	14:54:38.649	34:46:24.00	10.7 ± 2.4	$3.2^{+1.3}_{-1.1}$	$1.3^{+1.6}_{-0.8} \times 10^{13}$	Y
PLCK_G056.7+62.6-2	14:54:28.259	34:47:11.98	14.4 ± 3.3	$3.6^{+1.4}_{-1.1}$	$1.2^{+1.2}_{-0.7} \times 10^{13}$	Y
PLCK_G068.3+31.9-0	17:33:13.960	42:42:21.70	18.8 ± 2.8	$2.2^{+0.9}_{-0.8}$	$2.5^{+3.1}_{-1.6} \times 10^{13}$	Y
PLCK_G068.3+31.9-1	17:33:32.479	42:45:09.63	14.4 ± 3.6	$3.3^{+1.2}_{-1.0}$	$1.3^{+1.3}_{-0.7} \times 10^{13}$	N
PLCK_G075.1+33.2-0	17:29:51.000	48:31:35.00	13.1 ± 2.7	$6.2^{+1.6}_{-2.2}$	$1.5^{+1.0}_{-0.8} \times 10^{13}$	Y
PLCK_G077.7+32.6-0	17:33:47.863	50:44:56.17	14.9 ± 3.7	$2.0^{+0.8}_{-0.7}$	$8.4^{+10.5}_{-5.5} \times 10^{12}$	N
PLCK_G078.9+48.2-0	15:56:11.488	50:04:32.77	12.8 ± 2.4	$4.1^{+1.5}_{-1.4}$	$1.4^{+1.3}_{-0.8} \times 10^{13}$	Y
PLCK_G078.9+48.2-1	15:55:36.170	50:04:28.63	14.2 ± 3.3	> 5.4	$1.9^{+3.2}_{-1.0} \times 10^{13}$	Y
PLCK_G082.5+38.4-0	16:55:59.511	54:30:00.89	18.1 ± 2.0	> 7.0	$3.3^{+15.3}_{-1.5} \times 10^{13}$	Y
PLCK_G082.5+38.4-1	16:55:31.952	54:30:36.77	11.6 ± 2.8	$2.0^{+0.9}_{-0.7}$	$7.7^{+9.8}_{-5.0} \times 10^{12}$	Y
PLCK_G082.5+38.4-2	16:55:39.750	54:32:28.85	10.1 ± 2.5	$2.5^{+0.9}_{-0.8}$	$8.2^{+8.9}_{-5.0} \times 10^{12}$	N
PLCK_G083.3+51.0-0	15:33:13.312	51:47:39.00	12.2 ± 2.2	$3.4^{+1.3}_{-1.1}$	$1.3^{+1.4}_{-0.8} \times 10^{13}$	Y
PLCK_G083.3+51.0-1	15:32:51.293	51:52:06.92	16.5 ± 3.5	$4.1^{+1.5}_{-1.3}$	$1.7^{+1.6}_{-1.0} \times 10^{13}$	Y
PLCK_G083.3+51.0-2	15:32:57.793	51:46:54.97	13.0 ± 2.9	$3.2^{+1.7}_{-1.0}$	$9.2^{+10.0}_{-5.4} \times 10^{12}$	Y
PLCK_G091.9+43.0-0	16:09:59.845	60:19:52.00	17.2 ± 3.2	$3.6^{+1.3}_{-1.2}$	$1.5^{+1.6}_{-0.9} \times 10^{13}$	Y
PLCK_G091.9+43.0-1	16:10:14.926	60:19:15.96	15.5 ± 3.1	$3.4^{+1.3}_{-1.1}$	$1.8^{+1.9}_{-1.1} \times 10^{13}$	Y
PLCK_G093.6+55.9-0	14:44:05.173	54:16:45.00	17.3 ± 3.7	> 5.7	$2.4^{+2.5}_{-1.2} \times 10^{13}$	N
PLCK_G093.6+55.9-1	14:43:56.475	54:21:16.97	11.5 ± 2.5	$3.1^{+1.3}_{-1.0}$	$1.6^{+1.9}_{-1.0} \times 10^{13}$	Y
PLCK_G132.9-76.0-0	1:01:00.549	-13:17:54.25	16.1 ± 3.8	$2.6^{+1.0}_{-0.9}$	$1.6^{+1.9}_{-1.1} \times 10^{13}$	N
PLCK_G144.1+81.0-0	12:35:34.282	35:28:40.50	13.0 ± 2.7	$3.4^{+1.3}_{-1.0}$	$1.3^{+1.4}_{-0.7} \times 10^{13}$	Y
PLCK_G144.1+81.0-1	12:35:46.730	35:30:08.45	14.2 ± 3.5	> 6.3	$2.0^{+2.4}_{-1.0} \times 10^{13}$	N
PLCK_G160.7+41.0-0	9:07:54.534	56:03:10.89	22.3 ± 3.9	$3.9^{+1.5}_{-1.3}$	$2.9^{+3.2}_{-1.7} \times 10^{13}$	Y
PLCK_G162.1-59.3-0	2:06:51.367	-2:16:05.80	8.1 ± 1.6	$2.5^{+1.0}_{-0.9}$	$9.1^{+10.7}_{-5.9} \times 10^{12}$	Y
PLCK_G162.1-59.3-1	2:06:39.892	-2:11:21.80	14.3 ± 3.2	$3.1^{+1.1}_{-1.1}$	$2.0^{+2.1}_{-1.3} \times 10^{13}$	Y
PLCK_G162.1-59.3-2	2:06:39.090	-2:16:57.80	8.4 ± 2.0	$3.1^{+1.2}_{-1.1}$	$9.8^{+10.9}_{-6.1} \times 10^{12}$	N
PLCK_G162.1-59.3-3	2:06:49.232	-2:15:49.80	6.8 ± 1.6	> 4.5	$8.9^{+7.9}_{-4.5} \times 10^{12}$	Y
PLCK_G165.8+45.3-0	9:30:34.209	51:28:06.19	14.2 ± 3.5	> 5.7	$1.9^{+1.7}_{-0.9} \times 10^{13}$	N
PLCK_G173.8+59.3-0	10:40:31.859	42:43:23.00	12.6 ± 2.1	$3.2^{+1.3}_{-1.1}$	$1.2^{+1.4}_{-0.8} \times 10^{13}$	Y
PLCK_G173.8+59.3-1	10:40:30.765	42:48:11.00	17.1 ± 3.4	> 7.3	$2.9^{+13.7}_{-1.3} \times 10^{13}$	Y
PLCK_G177.0+35.9-0	8:30:58.465	43:40:11.16	11.0 ± 2.3	$5.6^{+1.9}_{-1.6}$	$1.4^{+1.1}_{-0.7} \times 10^{13}$	N
PLCK_G177.0+35.9-1	8:31:13.948	43:38:03.20	8.1 ± 1.7	$1.7^{+0.7}_{-0.7}$	$6.0^{+8.2}_{-4.3} \times 10^{12}$	Y
PLCK_G177.0+35.9-2	8:31:18.741	43:39:39.18	8.6 ± 1.8	$5.5^{+2.8}_{-2.0}$	$1.0^{+0.9}_{-0.5} \times 10^{13}$	Y
PLCK_G177.0+35.9-3	8:31:41.579	43:37:50.95	14.9 ± 3.4	> 5.3	$1.9^{+1.6}_{-0.9} \times 10^{13}$	N
PLCK_G177.0+35.9-4	8:31:02.153	43:39:59.18	9.0 ± 2.2	$0.5^{+0.5}_{-0.3}$	$2.5^{+10.3}_{-2.3} \times 10^{12}$	Y
PLCK_G179.3+50.7-0	9:51:38.990	41:39:15.59	12.2 ± 1.6	$2.8^{+1.2}_{-1.1}$	$1.2^{+1.6}_{-0.8} \times 10^{13}$	Y
PLCK_G179.3+50.7-1	9:51:41.131	41:39:43.60	8.4 ± 1.5	$2.9^{+1.2}_{-1.0}$	$9.1^{+11.6}_{-5.6} \times 10^{12}$	Y
PLCK_G179.3+50.7-2	9:51:44.700	41:40:07.60	7.0 ± 1.5	$3.7^{+1.7}_{-1.2}$	$7.5^{+7.5}_{-4.2} \times 10^{12}$	Y
PLCK_G179.3+50.7-3	9:52:00.771	41:41:47.53	9.0 ± 2.0	$4.3^{+1.6}_{-1.4}$	$1.0^{+1.0}_{-0.6} \times 10^{13}$	Y
PLCK_G179.3+50.7-4	9:51:45.413	41:35:39.60	10.6 ± 2.4	> 7.0	$1.6^{+3.5}_{-0.7} \times 10^{13}$	N
PLCK_G179.3+50.7-5	9:51:45.414	41:37:59.60	7.3 ± 1.7	$3.2^{+1.4}_{-1.1}$	$7.5^{+8.0}_{-4.5} \times 10^{12}$	Y
PLCK_G186.3-72.7-0	1:56:33.074	-18:27:31.60	11.3 ± 1.8	$3.0^{+1.3}_{-1.0}$	$1.3^{+1.7}_{-0.8} \times 10^{13}$	Y
PLCK_G186.3-72.7-1	1:56:33.636	-18:28:47.60	8.7 ± 2.0	$5.2^{+2.4}_{-1.7}$	$1.2^{+1.0}_{-0.6} \times 10^{13}$	Y
PLCK_G186.3-72.7-2	1:56:34.199	-18:28:39.60	8.7 ± 2.0	$2.9^{+1.2}_{-1.0}$	$1.4^{+1.8}_{-0.9} \times 10^{13}$	Y
PLCK_G186.6+66.7-0	11:08:36.022	35:06:04.00	12.7 ± 2.4	$4.8^{+1.8}_{-1.5}$	$1.5^{+1.3}_{-0.8} \times 10^{13}$	Y
PLCK_G188.6-68.9-0	2:11:48.227	-17:00:57.40	13.4 ± 1.9	$2.4^{+1.1}_{-1.0}$	$1.3^{+2.0}_{-1.0} \times 10^{13}$	Y
PLCK_G188.6-68.9-1	2:11:49.063	-17:02:49.40	8.8 ± 1.5	$2.5^{+1.0}_{-0.8}$	$8.7^{+10.7}_{-5.3} \times 10^{12}$	Y
PLCK_G188.6-68.9-2	2:11:52.131	-17:02:45.40	8.3 ± 1.5	> 5.1	$1.2^{+1.2}_{-0.6} \times 10^{13}$	Y
PLCK_G188.6-68.9-3	2:11:38.745	-17:01:09.38	10.4 ± 2.0	$2.5^{+1.1}_{-0.9}$	$1.2^{+1.6}_{-0.8} \times 10^{13}$	Y
PLCK_G188.6-68.9-4	2:11:33.720	-17:04:21.36	11.6 ± 2.4	$3.1^{+1.2}_{-1.1}$	$1.4^{+1.5}_{-0.9} \times 10^{13}$	Y
PLCK_G188.6-68.9-5	2:11:44.878	-17:05:57.40	9.2 ± 2.0	$2.6^{+1.0}_{-0.9}$	$9.9^{+11.7}_{-6.6} \times 10^{12}$	N

Gal ID	RA J2000	Dec J2000	S_{850} (mJy)	$z_{\rm phot}$	Far-IR Luminosity ($L_\odot$)	In Planck Beam
PLCK_G188.6-68.9-6	2:11:51.853	−17:05:49.40	11.2 ± 2.5	$3.0^{+1.2}_{-1.0}$	$1.7^{+2.1}_{-1.1} \times 10^{13}$	N
PLCK_G188.6-68.9-7	2:11:42.649	−17:00:57.39	8.9 ± 2.0	> 5.7	$1.2^{+1.1}_{-0.6} \times 10^{13}$	Y
PLCK_G188.6-68.9-8	2:11:47.669	−17:01:45.40	7.1 ± 1.6	$3.1^{+1.1}_{-1.0}$	$1.0^{+1.1}_{-0.6} \times 10^{13}$	Y
PLCK_G188.6-68.9-9	2:11:56.315	−17:03:21.39	7.8 ± 1.8	$4.6^{+2.2}_{-1.4}$	$8.8^{+8.0}_{-4.7} \times 10^{12}$	Y
PLCK_G188.6-68.9-10	2:11:45.159	−17:00:41.40	9.1 ± 2.1	$2.5^{+1.1}_{-1.0}$	$1.1^{+1.6}_{-0.8} \times 10^{13}$	Y
PLCK_G188.6-68.9-11	2:11:52.688	−16:59:01.40	9.9 ± 2.4	$4.2^{+2.2}_{-1.4}$	$9.5^{+9.1}_{-5.3} \times 10^{12}$	Y
PLCK_G191.3+62.0-0	10:44:57.144	33:51:38.09	12.2 ± 3.0	$1.6^{+0.8}_{-0.7}$	$1.2^{+1.9}_{-0.9} \times 10^{13}$	Y
PLCK_G191.3+62.0-1	10:45:07.096	33:50:50.03	16.0 ± 3.9	$3.3^{+1.3}_{-1.0}$	$1.1^{+1.1}_{-0.6} \times 10^{13}$	Y
PLCK_G191.8-83.4-0	1:18:28.190	−24:34:10.19	9.6 ± 1.6	$4.1^{+1.6}_{-1.4}$	$1.0^{+1.0}_{-0.6} \times 10^{13}$	Y
PLCK_G191.8-83.4-1	1:18:23.791	−24:34:26.17	12.8 ± 2.2	$3.4^{+1.3}_{-1.1}$	$1.4^{+1.6}_{-0.8} \times 10^{13}$	Y
PLCK_G191.8-83.4-2	1:18:21.148	−24:36:42.15	10.9 ± 1.9	$3.2^{+1.3}_{-1.1}$	$1.1^{+1.2}_{-0.7} \times 10^{13}$	Y
PLCK_G191.8-83.4-3	1:18:30.241	−24:35:38.19	9.1 ± 1.6	$3.0^{+1.2}_{-1.0}$	$1.2^{+1.5}_{-0.7} \times 10^{13}$	Y
PLCK_G191.8-83.4-4	1:18:25.253	−24:37:30.17	9.4 ± 1.8	$2.0^{+0.9}_{-0.8}$	$1.2^{+1.8}_{-0.9} \times 10^{13}$	Y
PLCK_G191.8-83.4-5	1:18:39.920	−24:36:10.20	8.7 ± 1.7	$2.1^{+0.9}_{-0.8}$	$9.2^{+11.6}_{-6.4} \times 10^{12}$	Y
PLCK_G191.8-83.4-6	1:18:27.605	−24:32:46.18	8.7 ± 1.9	> 6.2	$1.3^{+1.3}_{-0.6} \times 10^{13}$	Y
PLCK_G191.8-83.4-7	1:18:36.693	−24:34:38.20	6.8 ± 1.5	$2.5^{+1.8}_{-1.0}$	$7.7^{+10.2}_{-5.0} \times 10^{12}$	Y
PLCK_G191.8-83.4-8	1:18:41.680	−24:36:46.19	7.5 ± 1.8	$3.0^{+1.1}_{-1.0}$	$8.7^{+9.5}_{-5.3} \times 10^{12}$	Y
PLCK_G191.8-83.4-9	1:18:36.986	−24:34:42.20	6.0 ± 1.5	$3.5^{+3.3}_{-1.6}$	$6.8^{+7.2}_{-4.0} \times 10^{12}$	Y
PLCK_G201.1+50.7-0	9:53:11.581	27:54:30.40	9.2 ± 1.7	$3.3^{+1.2}_{-1.1}$	$1.1^{+1.2}_{-0.7} \times 10^{13}$	Y
PLCK_G201.1+50.7-1	9:53:08.864	27:55:38.39	8.3 ± 1.8	$1.9^{+1.4}_{-0.8}$	$9.2^{+12.5}_{-6.3} \times 10^{12}$	N
PLCK_G201.1+50.7-2	9:53:14.598	27:56:02.40	7.2 ± 1.6	$3.7^{+1.5}_{-1.2}$	$8.5^{+9.0}_{-5.0} \times 10^{12}$	Y
PLCK_G201.1+50.7-3	9:53:08.562	27:55:34.39	7.6 ± 1.8	$3.0^{+2.5}_{-1.4}$	$8.3^{+9.5}_{-5.4} \times 10^{12}$	N
PLCK_G213.0+65.9-0	11:04:38.213	24:36:35.50	12.3 ± 3.0	$3.6^{+1.3}_{-1.1}$	$1.3^{+1.2}_{-0.7} \times 10^{13}$	Y
PLCK_G213.0+65.9-1	11:04:44.075	24:33:39.48	13.7 ± 3.4	$4.8^{+1.6}_{-1.3}$	$1.5^{+1.2}_{-0.8} \times 10^{13}$	Y
PLCK_G223.9+41.2-0	9:37:14.190	10:00:05.39	16.2 ± 1.9	$2.5^{+1.1}_{-0.9}$	$1.6^{+2.2}_{-1.1} \times 10^{13}$	Y
PLCK_G223.9+41.2-1	9:36:45.214	10:01:45.37	14.0 ± 2.3	$3.2^{+1.2}_{-1.1}$	$1.4^{+1.5}_{-0.9} \times 10^{13}$	N
PLCK_G223.9+41.2-2	9:37:03.088	9:58:25.40	7.2 ± 1.2	$1.2^{+0.7}_{-0.6}$	$6.1^{+12.5}_{-4.7} \times 10^{12}$	Y
PLCK_G223.9+41.2-3	9:36:52.257	9:58:45.39	9.4 ± 1.7	$2.9^{+1.2}_{-1.0}$	$1.2^{+1.4}_{-0.7} \times 10^{13}$	Y
PLCK_G223.9+41.2-4	9:37:18.523	10:00:41.38	12.4 ± 2.4	> 5.6	$1.7^{+1.3}_{-0.8} \times 10^{13}$	Y
PLCK_G223.9+41.2-5	9:37:01.192	9:58:29.40	5.9 ± 1.2	$2.4^{+0.9}_{-0.9}$	$6.3^{+7.6}_{-4.2} \times 10^{12}$	Y
PLCK_G223.9+41.2-6	9:36:42.512	9:56:21.36	10.2 ± 2.3	$4.4^{+2.0}_{-1.4}$	$1.1^{+0.9}_{-0.6} \times 10^{13}$	N
PLCK_G223.9+41.2-7	9:36:50.633	9:58:25.38	7.5 ± 1.8	$4.3^{+1.9}_{-1.4}$	$8.4^{+7.9}_{-4.7} \times 10^{12}$	Y
PLCK_G328.9+71.4-0	13:24:12.114	10:15:42.39	15.5 ± 3.0	$3.4^{+1.3}_{-1.2}$	$1.8^{+2.0}_{-1.1} \times 10^{13}$	N
PLCK_G328.9+71.4-1	13:24:03.171	10:12:22.40	10.5 ± 2.1	$2.2^{+0.9}_{-0.8}$	$1.3^{+1.7}_{-0.9} \times 10^{13}$	Y
PLCK_G328.9+71.4-2	13:23:44.744	10:14:10.37	13.6 ± 3.1	> 6.8	$2.0^{+3.1}_{-0.9} \times 10^{13}$	Y
PLCK_G328.9+71.4-3	13:23:46.372	10:12:22.37	12.9 ± 3.1	> 6.9	$2.0^{+4.6}_{-0.9} \times 10^{13}$	Y
PLCK_G49.6-42.9-0	21:51:38.531	−7:05:06.90	9.9 ± 1.6	$2.4^{+1.0}_{-0.9}$	$1.2^{+1.6}_{-0.8} \times 10^{13}$	Y
PLCK_G49.6-42.9-1	21:51:41.219	−7:05:54.90	7.8 ± 1.9	$2.7^{+1.1}_{-0.9}$	$7.4^{+8.4}_{-4.4} \times 10^{12}$	Y
PLCK_G49.6-42.9-2	21:51:33.694	−7:05:02.90	6.5 ± 1.6	> 5.6	$8.7^{+8.5}_{-4.3} \times 10^{12}$	Y
PLCK_G84.0-71.5-0	0:04:16.645	−12:18:09.58	16.5 ± 2.6	$4.2^{+1.5}_{-1.3}$	$1.8^{+1.8}_{-1.0} \times 10^{13}$	Y
PLCK_G84.0-71.5-1	0:04:17.194	−12:14:05.58	15.5 ± 3.6	> 4.8	$1.9^{+1.7}_{-1.0} \times 10^{13}$	N
PLCK_G84.0-71.5-2	0:04:30.019	−12:17:53.60	9.1 ± 2.2	> 5.6	$1.2^{+1.0}_{-0.6} \times 10^{13}$	Y
PLCK_HZ_G038.0-51.5-0	22:08:50.400	−17:55:47.90	15.9 ± 2.0	$2.7^{+1.1}_{-1.0}$	$1.9^{+2.2}_{-1.3} \times 10^{13}$	Y
PLCK_HZ_G038.0-51.5-1	22:08:48.438	−17:57:35.90	10.3 ± 2.0	$3.1^{+1.2}_{-1.1}$	$1.1^{+1.3}_{-0.7} \times 10^{13}$	Y
PLCK_HZ_G038.0-51.5-2	22:08:45.353	−17:59:27.90	10.4 ± 2.4	$2.3^{+0.9}_{-0.9}$	$9.5^{+12.3}_{-6.5} \times 10^{12}$	Y
PLCK_HZ_G067.2-63.8-0	23:24:24.799	−10:43:46.08	22.7 ± 3.5	$3.1^{+1.2}_{-1.1}$	$2.0^{+2.3}_{-1.3} \times 10^{13}$	N
PLCK_HZ_G067.2-63.8-1	23:24:12.043	−10:46:14.10	11.1 ± 1.8	$2.6^{+1.0}_{-0.9}$	$1.2^{+1.4}_{-0.8} \times 10^{13}$	Y
PLCK_HZ_G067.2-63.8-2	23:24:23.718	−10:50:18.08	12.6 ± 2.1	$3.0^{+1.3}_{-1.0}$	$1.6^{+2.1}_{-1.0} \times 10^{13}$	N
PLCK_HZ_G067.2-63.8-3	23:24:01.728	−10:45:26.09	13.1 ± 2.2	$4.9^{+1.8}_{-1.5}$	$1.6^{+1.4}_{-0.9} \times 10^{13}$	Y
PLCK_HZ_G067.2-63.8-4	23:24:00.643	−10:45:06.09	11.9 ± 2.2	$2.7^{+1.3}_{-1.0}$	$1.3^{+2.0}_{-0.9} \times 10^{13}$	Y
PLCK_HZ_G067.2-63.8-5	23:24:16.658	−10:48:30.10	7.8 ± 1.7	$3.6^{+1.5}_{-1.1}$	$8.9^{+9.4}_{-5.1} \times 10^{12}$	Y
PLCK_HZ_G067.2-63.8-6	23:24:06.614	−10:47:14.10	7.1 ± 1.5	$2.3^{+0.9}_{-0.8}$	$8.1^{+9.9}_{-5.5} \times 10^{12}$	Y
PLCK_HZ_G067.2-63.8-7	23:23:56.023	−10:51:30.08	10.7 ± 2.4	$1.6^{+0.8}_{-0.7}$	$1.3^{+2.1}_{-1.0} \times 10^{13}$	N
PLCK_HZ_G067.2-63.8-8	23:24:01.453	−10:52:06.09	8.9 ± 2.1	$6.3^{+2.3}_{-2.1}$	$1.1^{+0.9}_{-0.6} \times 10^{13}$	Y
PLCK_HZ_G067.2-63.8-9	23:23:59.014	−10:45:34.08	8.6 ± 2.1	$3.5^{+1.4}_{-1.1}$	$8.7^{+8.7}_{-5.1} \times 10^{12}$	Y
PLCK_HZ_G067.2-63.8-10	23:24:27.248	−10:51:10.07	11.8 ± 2.8	$4.1^{+1.6}_{-1.3}$	$1.3^{+1.2}_{-0.7} \times 10^{13}$	N
PLCK_HZ_G067.2-63.8-11	23:24:12.314	−10:48:06.10	5.9 ± 1.5	> 5.4	$7.9^{+8.2}_{-3.9} \times 10^{12}$	Y
PLCK_HZ_G103.1-73.6-0	0:28:48.011	−11:35:52.39	9.0 ± 2.2	> 4.0	$1.1^{+1.0}_{-0.6} \times 10^{13}$	Y
PLCK_HZ_G106.8-83.3-0	0:43:25.677	−20:36:20.29	22.8 ± 1.7	$3.6^{+1.3}_{-1.3}$	$2.5^{+2.7}_{-1.6} \times 10^{13}$	Y
PLCK_HZ_G106.8-83.3-1	0:43:17.415	−20:36:00.30	10.2 ± 1.4	$2.2^{+0.9}_{-0.8}$	$1.5^{+1.9}_{-1.0} \times 10^{13}$	Y

Gal ID	RA J2000	Dec J2000	S_{850} (mJy)	$z_{\rm phot}$	Far-IR Luminosity ($L_\odot$)	In Planck Beam
PLCK_HZ_G106.8-83.3-2	0:43:14.281	−20:36:12.30	10.1 ± 1.4	$2.4^{+1.1}_{-0.9}$	$9.5^{+13.6}_{-6.4} \times 10^{12}$	Y
PLCK_HZ_G106.8-83.3-3	0:43:21.689	−20:36:40.30	9.1 ± 1.5	$5.2^{+2.3}_{-1.7}$	$1.1^{+0.9}_{-0.6} \times 10^{13}$	Y
PLCK_HZ_G106.8-83.3-4	0:43:02.320	−20:34:04.26	12.4 ± 2.1	$2.6^{+1.0}_{-0.9}$	$1.5^{+1.7}_{-1.0} \times 10^{13}$	Y
PLCK_HZ_G106.8-83.3-5	0:43:32.230	−20:36:48.26	12.0 ± 2.1	$2.7^{+1.1}_{-0.8}$	$1.5^{+1.7}_{-0.9} \times 10^{13}$	Y
PLCK_HZ_G106.8-83.3-6	0:43:41.064	−20:37:20.20	19.1 ± 3.9	> 7.0	$3.2^{+9.9}_{-1.5} \times 10^{13}$	N
PLCK_HZ_G106.8-83.3-7	0:43:04.598	−20:34:24.27	9.4 ± 2.0	$3.3^{+1.2}_{-1.1}$	$1.1^{+1.1}_{-0.7} \times 10^{13}$	Y
PLCK_HZ_G106.8-83.3-8	0:43:04.882	−20:34:52.27	8.7 ± 1.9	$4.7^{+2.1}_{-1.6}$	$1.0^{+0.8}_{-0.5} \times 10^{13}$	Y
PLCK_HZ_G106.8-83.3-9	0:43:32.807	−20:40:44.26	13.9 ± 3.1	$3.9^{+1.6}_{-1.2}$	$1.3^{+1.2}_{-0.7} \times 10^{13}$	Y
PLCK_HZ_G106.8-83.3-10	0:43:12.001	−20:37:36.29	7.0 ± 1.6	$3.6^{+1.5}_{-1.2}$	$7.6^{+8.3}_{-4.4} \times 10^{12}$	Y
PLCK_HZ_G106.8-83.3-11	0:43:29.099	−20:38:44.28	8.1 ± 2.0	$4.9^{+2.0}_{-1.6}$	$9.7^{+8.5}_{-5.2} \times 10^{12}$	Y
PLCK_HZ_G106.8-83.3-12	0:43:17.700	−20:36:48.30	5.9 ± 1.4	$2.3^{+1.0}_{-0.8}$	$7.9^{+10.9}_{-5.1} \times 10^{12}$	Y
PLCK_HZ_G119.4-76.6-0	0:48:10.840	−13:45:56.30	24.5 ± 2.2	$3.1^{+1.1}_{-1.1}$	$2.9^{+3.1}_{-1.9} \times 10^{13}$	Y
PLCK_HZ_G119.4-76.6-1	0:47:52.723	−13:41:56.28	10.7 ± 1.9	$2.6^{+1.0}_{-1.1}$	$1.9^{+2.1}_{-1.4} \times 10^{13}$	Y
PLCK_HZ_G119.4-76.6-2	0:48:10.016	−13:44:28.30	10.8 ± 2.4	$3.7^{+1.5}_{-1.2}$	$1.2^{+1.3}_{-0.7} \times 10^{13}$	Y
PLCK_HZ_G119.4-76.6-3	0:47:59.311	−13:40:32.30	7.4 ± 1.7	> 5.5	$1.1^{+1.6}_{-0.5} \times 10^{13}$	Y
PLCK_HZ_G119.4-76.6-4	0:48:02.604	−13:40:12.30	7.0 ± 1.7	> 2.7	$8.6^{+11.3}_{-5.2} \times 10^{12}$	Y
PLCK_HZ_G119.4-76.6-5	0:47:53.273	−13:41:12.28	7.6 ± 1.8	> 5.5	$1.1^{+1.2}_{-0.5} \times 10^{13}$	Y
PLCK_HZ_G119.4-76.6-6	0:48:08.093	−13:37:24.30	9.2 ± 2.2	> 5.6	$1.2^{+1.1}_{-0.6} \times 10^{13}$	N
PLCK_HZ_G119.4-76.6-7	0:47:45.864	−13:39:36.26	10.0 ± 2.5	$2.3^{+0.9}_{-0.8}$	$9.6^{+12.1}_{-6.4} \times 10^{12}$	N
PLCK_HZ_G119.4-76.6-8	0:48:13.584	−13:43:12.29	8.1 ± 2.0	> 6.9	$1.1^{+1.2}_{-0.5} \times 10^{13}$	Y
PLCK_HZ_G132.6-81.1-0	0:57:48.895	−18:19:23.50	13.3 ± 2.1	$3.3^{+1.4}_{-1.2}$	$1.5^{+1.8}_{-1.0} \times 10^{13}$	Y
PLCK_HZ_G132.6-81.1-1	0:57:52.265	−18:19:03.49	8.6 ± 2.1	> 4.8	$1.1^{+1.0}_{-0.6} \times 10^{13}$	Y
PLCK_HZ_G171.1-78.7-0	1:27:01.926	−19:19:41.60	14.6 ± 2.1	$3.1^{+1.1}_{-1.1}$	$1.6^{+1.7}_{-1.0} \times 10^{13}$	Y
PLCK_HZ_G171.1-78.7-1	1:26:50.339	−19:20:13.56	15.4 ± 3.6	$5.4^{+2.4}_{-1.7}$	$1.7^{+1.5}_{-0.9} \times 10^{13}$	Y
PLCK_HZ_G171.1-78.7-2	1:27:08.708	−19:18:57.60	9.0 ± 2.1	$4.9^{+2.4}_{-1.7}$	$1.1^{+1.0}_{-0.6} \times 10^{13}$	Y
PLCK_HZ_G171.1-78.7-3	1:27:08.708	−19:19:01.60	8.7 ± 2.1	$4.0^{+2.0}_{-1.3}$	$1.1^{+1.0}_{-0.6} \times 10^{13}$	Y
PLCK_HZ_G173.9+57.0-0	10:28:38.124	43:25:37.69	8.5 ± 1.9	$3.7^{+1.6}_{-1.2}$	$9.5^{+9.9}_{-5.6} \times 10^{12}$	Y
PLCK_HZ_G173.9+57.0-1	10:28:48.771	43:24:53.70	8.7 ± 2.0	$2.4^{+1.0}_{-0.9}$	$1.1^{+1.5}_{-0.8} \times 10^{13}$	Y
PLCK_HZ_G176.6+59.0-0	10:36:56.556	41:27:22.40	15.8 ± 2.6	$3.3^{+1.2}_{-1.2}$	$1.9^{+1.9}_{-1.2} \times 10^{13}$	Y
PLCK_HZ_G176.6+59.0-1	10:37:05.451	41:27:30.38	12.5 ± 3.0	$2.1^{+1.0}_{-0.8}$	$1.4^{+2.2}_{-1.0} \times 10^{13}$	Y
PLCK_HZ_G214.1+48.3-0	9:52:34.268	19:08:18.69	15.7 ± 3.1	$6.4^{+2.2}_{-2.0}$	$1.8^{+1.4}_{-0.9} \times 10^{13}$	Y
PLCK_HZ_G214.1+48.3-1	9:52:39.349	19:08:30.67	14.9 ± 3.2	> 6.9	$2.2^{+5.1}_{-1.0} \times 10^{13}$	Y
PLCK_HZ_G214.1+48.3-2	9:52:09.714	19:06:26.66	15.2 ± 3.6	$5.6^{+2.1}_{-1.6}$	$1.7^{+1.3}_{-0.8} \times 10^{13}$	N
Planck18p194-0	8:30:46.455	19:36:47.19	19.6 ± 1.9	$3.3^{+1.4}_{-1.1}$	$2.2^{+2.7}_{-1.4} \times 10^{13}$	Y
Planck18p194-1	8:30:54.382	19:37:31.20	14.9 ± 1.7	$3.3^{+1.4}_{-1.2}$	$1.8^{+2.2}_{-1.1} \times 10^{13}$	Y
Planck18p194-2	8:30:51.551	19:37:55.20	10.7 ± 1.6	$5.3^{+2.1}_{-1.7}$	$1.3^{+1.1}_{-0.7} \times 10^{13}$	Y
Planck18p194-3	8:30:41.073	19:39:43.18	13.7 ± 2.5	$4.9^{+1.7}_{-1.5}$	$1.6^{+1.5}_{-0.9} \times 10^{13}$	Y
Planck18p194-4	8:31:04.287	19:34:23.18	13.7 ± 3.1	$3.4^{+1.3}_{-1.1}$	$1.5^{+1.5}_{-0.9} \times 10^{13}$	N
Planck18p194-5	8:30:40.228	19:36:15.17	8.5 ± 2.0	> 6.7	$1.3^{+2.3}_{-0.6} \times 10^{13}$	Y
Planck18p194-6	8:30:51.268	19:37:31.20	6.8 ± 1.7	$3.2^{+1.2}_{-1.0}$	$8.9^{+9.7}_{-5.4} \times 10^{12}$	Y
Planck18p194-7	8:30:48.719	19:37:55.20	6.5 ± 1.6	$4.0^{+1.5}_{-1.2}$	$8.1^{+7.8}_{-4.6} \times 10^{12}$	Y
Planck18p735-0	1:58:48.085	−7:52:43.50	8.5 ± 2.0	$2.8^{+1.2}_{-1.0}$	$1.3^{+1.7}_{-0.9} \times 10^{13}$	Y
Planck24p194-0	8:40:40.588	22:12:37.60	8.3 ± 1.6	$2.8^{+1.1}_{-0.9}$	$1.2^{+1.4}_{-0.8} \times 10^{13}$	Y